Ph.D. Thesis

Molecular Dynamics Study of Oil–Water Interfacial Equilibrium in Petroleum Engineering

Makoto Kunieda

Abstract

Interfacial phenomena are ubiquitous in a number of natural and technological processes, and concern areas where chemistry, physics, and engineering intersect. Unlike the bulk material, the interface is non-centrosymmetric. The interfacial phenomena such as surface/interfacial tension, wetting, spreading, mutual diffusion and etc. are governed by interactions between molecules at the interface of their phases, acting usually over a few molecular distances. These length scales are being probed with experimental techniques, such as atomic force microscopy and surface forces measurement, or theoretical tools, such as molecular simulations, to obtain new insights into interface phenomena. Molecular simulations are powerful techniques by which we can obtain thermodynamic properties of the system of given composition at desired temperature and pressure, and it also enables us to observe microscopic phenomena by direct visualization.

In this dissertation, Molecular Dynamics (MD, one of molecular simulations) simulations have been performed to investigate the oil–water interfacial equilibrium, related to the primary oil production and the enhanced oil recovery (EOR) techniques in the oil industries. The results are followings:

(1) The interfacial equilibrium of a light-oil–water interface system was investigated by using MD method. In advance, the accuracies of each hydrocarbon model were checked by comparing to the experimental values on the thermodynamic properties, such as the bulk density and IFTs at an ambient condition. The light-oil model was modeled as a mixture of eight kinds of hydrocarbons, including n-alkanes, cycloalkanes and aromatics. The results showed the inhomogeneity of the molecular distributions, such as strong accumulation of aromatic molecules at the light-oil–water interface, which were caused by the specific interaction between aromatic and water, called as weak hydrogen bonding. This phenomenon affects a large area of the oil–water interface properties.

(2) The interfacial equilibrium of a decane–water–vapor three phase system was investigated by using MD method. The inhomogeneity of the molecular distribution, especially at the vicinity of three phase contact line, and the interfacial tensions of each interface were obtained. In addition, the convenient equation to calculate the line tension of three phases system from local pressure distribution was derived and applied to the decane–water–vapor three phase system. With this method, the line tension of the decane–water–vapor three phase system was calculated

successfully. And the size dependence of the contact angle inside of the droplet was estimated from nano to macro scales by using the three calculated interfacial tensions and the line tension with the general form of Neumann triangle relationship.

(3) The interfacial equilibrium of a multicomponent-oil–water–vapor three phase system was investigated by using MD method. The multicomponent-oil was modeled as a mixture of heptane, decane and toluene. The line tension, the interfacial tensions and the molecular distributions in the multicomponent-oil–water–vapor three phase system were obtained and discussed. The effects by impurity of the droplet, such as lower interfacial tension and higher line tension, molecular coverage on water surface by toluene molecules, were shown. The line tension value has changed from negative to positive value by adding heptane and toluene molecules into decane droplet. This causes opposite trend in size dependence of the contact angle of droplet.

Contents

List of Figures

List of Tables

Chapter 1

Introduction

1.1 Enhanced Oil Recovery

Currently, the biggest issue in our society is how to meet the increasing global energy demand. It is having become difficult to find new big oil fields, the oil price has risen. Some new energy resources have been suggested and investigated as an alternative energy to replace existing ones. However they are still in the research phase. Under this circumstance, one of the promising solutions to the problem is to increase the oil production from existing oil fields, which is called Enhanced Oil Recovery (EOR) techniques (Lake, 1989; Thomas, 2008). The EOR techniques are increasingly important for the energy security, as the reserves are limited. There are many EOR techniques, including gas injection and chemical injection, among others (Lake, 1989; Pedersen and Christensen, 2006; Thomas, 2008). These techniques try to change physical or chemical properties of fluids in the petroleum reservoirs. The target of EOR varies considerably for the different types of hydrocarbons (Thomas, 2008). Fig.1.1 shows the fluid saturations and the target of EOR for typical light and heavy oil reservoirs and tar sands. For light oil reservoirs, EOR is usually applicable after secondary recovery operations, and the EOR target is $\sim 45\%$ OOIP (original oil in place). Heavy oils and tar sands respond poorly to primary and secondary recovery methods, and the bulk of the production from such reservoirs come from EOR methods.

1.1.1 Interfacial phenomena in petroleum engineering

The interfaces between immiscible liquids are ubiquitous and play an important role in many natural and technological processes (Assael et al., 1996; Batzle and Wang, 1992; Benjamin, 1997; Bonn et al., 2009; Chandler, 2007; Chiquet et al., 2007; Di Leo and Maranon, 2004; Hore

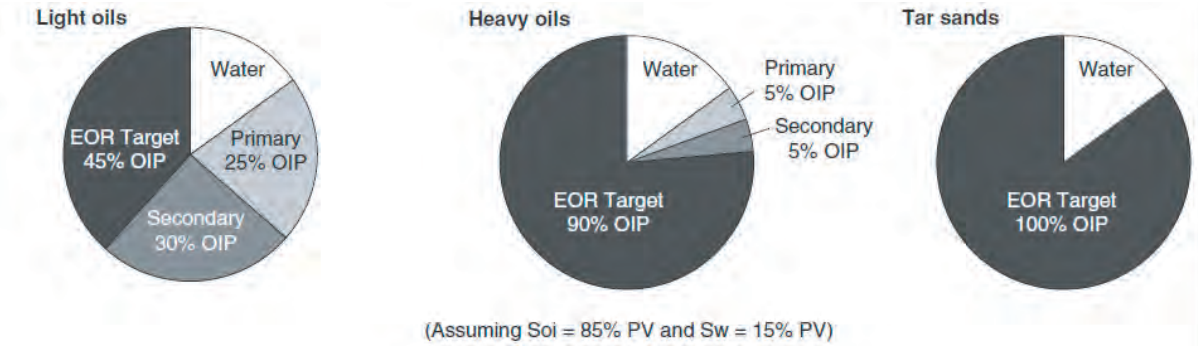

Figure 1.1: EOR target for different hydrocarbons (Thomas, 2008).

et al., 2008; Jungwirth et al., 2006). Unlike the bulk materials, the interface system is a non-centrosymmetric environment about which we know very little.

Mobilization of residual oil is influenced by two major factors: Capillary Number (N_c) and Mobility Ratio (M) (Thomas, 2008). Capillary Number is defined as $N_c = v\mu/\gamma$, where v is the Darcy velocity (m/s), μ is the displacing fluid viscosity (Pa·s) and γ is the interfacial tension (N/m). The most effective and practical way of increasing the Capillary Number is by reducing γ. Mobility ratio is defined as $M = \lambda_{ing}/\lambda_{ed}$, where λ_{ing} is the mobility of the displacing fluid (e.g. water), and λ_{ed} is the mobility of the displaced fluid (oil). ($\lambda = k/\mu$, where k is the effective permeability (m^2), and μ is the viscosity (Pa·s) of the fluid concerned). Mobility ratio influences the microscopic and macroscopic displacement efficiencies.

So the one of the main approaches to the EOR techniques is to decrease the interfacial tension or the viscosity of the crude oil through molecular additives that are adsorbed at the oil–water interface or migrate into the crude oil through the interface (Lake, 1989; Thomas, 2008; Zhang et al., 2010). It is important, therefore, for the phenomena pertaining to the crude oil and underground fluid (usually aqueous) interface to be understood.

1.1.2 Environmental concerns

Besides of the high energy demands in the petroleum technology fields, human security engineering has been growing in importance since the BP oil spill disaster. On April 20, 2010, the BP oil spill occurred in the Gulf of Mexico. The spilled oil spread immediately on the ocean surface in the Gulf of Mexico, and led to secondary disasters to humans and nature lives. The oil-water-vapor three phase interaction is key factor to this phenomena. Therefore, deep understandings

of these properties can prevent the secondary disasters efficiently.

1.1.3 Previous researches

In the past, much experimental work has been carried out to understand the properties of water next to hydrophobic surfaces (Du et al., 1994; Scatena et al., 2001), including the orientation of water and its hydrogen bonding. However, there has been little exploration of the structural properties of oil next to the interface. Experimental measurements for liquid–liquid interfaces are still challenging (De Serio et al., 2006; Du et al., 1994; Lambert et al., 2009; Mitrinovic et al., 2000; Nomoto and Onishi, 2007; Scatena et al., 2001) because of the relatively small sizes typically only a few molecular diameters widesand the buried nature of the interface.

Although computational approaches such as Molecular Dynamics (MD) and Monte Carlo (MC) simulations can provide insights into the structural properties of oil–water interfacial systems, most studies have been limited to the stable interfacial structure of a pure hydrocarbon–water system (Bresme et al., 2008; Chau and Hardwick, 1998; Kereszturi and Jedlovszky, 2005; Linse, 1987; Nicolas and de Souza, 2004; Patel and Brooks, 2006; van Buuren et al., 1993) or that with surfactant (Ikeda et al., 1992; Jang et al., 2004). However, crude oil is a highly complex material that consists mainly of hydrocarbons but can hardly be described as a single hydrocarbon phase (Pedersen and Christensen, 2006; Riazi and AlSahhaf, 1996). In particular, it is widely accepted that the percentage contents of paraffinic (alkane), naphthenic (cycloalkane), and aromatic components in reservoir fluids (often referred to as the PNA distribution) are essential properties when describing crude oil (Pedersen and Christensen, 2006). Recent experimental studies have reported that trace impurities can significantly modify the interfacial tension, by up to 10-20 mN/m, over a period of a few hours (Mitrinovic et al., 2000). Theoretical investigations have also shown that even mixtures containing only n-alkanes exhibit exotic phenomena compared with a single-component system (Xia and Landman, 1993).

1.2 Overview of this research

The purposes of this dissertation are to investigate the interfacial equilibrium of various liquids, such as hydrocarbons, light oil, water and their vapor, in nano scale and evaluate macroscopic properties by using MD methods.

In Chapter 2, the methodology of MD methods are described.

In Chapter 3, the oil–water interface system is investigated by using MD methods. First, the accuracies of hydrocarbon models are verified by comparing their thermodynamic properties to the experimental values at ambient conditions. Then, the light-oil model is modeled as a mixture of their hydrocarbons in order to investigate the interfacial equilibrium of the light-oil–water interface system. The results are discussed on the inhomogeneity of the molecular distributions and the specific interaction between aromatic and water, called as weak hydrogen bonding.

In Chapter 4, the decane–water–vapor three phase system is investigated by using MD methods. At first, a convenient way to calculate the line tension of a three liquid phase system is derived as a function of the local pressure distributions. With this method, the line tension of our decane–water–vapor three phase system is calculated from our MD simulation results. Then MD simulation is carried out with an apparent 2 dimensional system. And also, the inhomogeneity of the molecular distribution and the interfacial tensions of each interface are discussed.

In Chapter 5, the three phase system is investigated similar to Chapter 4, but the mixture of heptane, decane and toluene for an oil phase is used instead of just decane. The technical methodologies are almost same with those used in Chapter 4. The line tension, the interfacial tensions and the molecular distributions of the oil, water and vapor three phase system are obtained and discussed. Then the results are compared to those of pure decane case (Chapter 4). The effects caused by impurity of the droplet, such as lower interfacial tension and higher line tension, thin film of toluene molecules on water surface, are discussed.

Finally, the conclusion of this dissertation is described in Chapter 6.

Chapter 2

Methodology of Molecular Dynamics

2.1 Introduction

Computational Chemistry is a name to indicate the use of computational techniques in chemistry, ranging from quantum mechanics of molecules to dynamics of large complex molecular aggregates. Molecular simulation is main approach in computational chemistry, and can be defined as a kind of particle simulation where the individual position of every atom in the system is explicitly accounted for (Frenkel and Smit, 2002; Kadau et al., 2004). Once proper potential function and parameters for atoms composing molecules are given, it allows us to obtain thermodynamic properties of the system consisting of molecules at given pressure and temperature conditions. Macroscopic properties are always ensemble averages over a representative statistical ensemble of molecular systems. Molecular Dynamics (MD) simulation is one of the many techniques that belong to the realm of computational chemistry and molecular modeling.

In this dissertation, MD simulations are employed to investigate the interfacial equilibrium of various liquids including oil, water and their vapor phases. Fundamental algorithm of MD methods are described in first several sections in this chapter. And then, thermodynamic ensembles used in this dissertation are described. The details of algorithms and further techniques of MD methods can be found in Allen and Tildesley (1989); Frenkel and Smit (2002); Hess et al. (2008); Van Der Spoel et al. (2005).

2.2 Newton's equations of motion

MD simulations solve Newton's equations of motion for a system of N interacting atoms, which are given by:

$$m_i \frac{\partial^2 \boldsymbol{r}_i}{\partial t^2} = \boldsymbol{F}_i \tag{2.1}$$

where m_i and $\boldsymbol{r}_i$ are the mass and position vector of atom i, and $\boldsymbol{F}_i$ is the force acted on atom i. The forces are given as the negative derivatives of a potential function $U(\boldsymbol{r}_1, \boldsymbol{r}_2, \ldots, \boldsymbol{r}_N)$:

$$\boldsymbol{F}_i = -\frac{\partial U}{\partial \boldsymbol{r}_i} \tag{2.2}$$

Eq.(2.2) for all atoms in the system are solved simultaneously in small time steps, Δt. The system is followed for some time, taking care that the temperature and pressure remain at the required values, and the coordinates are written to an output file at regular intervals. The coordinates as a function of time represent a trajectory of the system. By averaging over an equilibrium trajectory, many macroscopic properties can be extracted from the output file. Thermodynamic properties $\langle X \rangle$ are obtained by the time averages of them as follows:

$$\langle X \rangle = \frac{1}{t} \int_0^t X(t)\, dt \tag{2.3}$$

2.3 Update configuration

In this dissertation, MD simulations use the algorithm so-called *leap-frog* to integrate the equation of motion (Eq.(2.1)). The leap-frog algorithm uses positions $\boldsymbol{r}$ at time t and velocities $\boldsymbol{v}$ at time $t - \frac{\Delta t}{2}$, and it updates positions and velocities using the force $\boldsymbol{F}(t)$ (Eq.(2.2)) determined by the positions at time t:

$$\boldsymbol{v}\left(t + \frac{\Delta t}{2}\right) = \boldsymbol{v}\left(t - \frac{\Delta t}{2}\right) + \frac{\boldsymbol{F}(t)}{m}\Delta t \tag{2.4}$$

$$\boldsymbol{r}(t + \Delta t) = \boldsymbol{r}(t) + \boldsymbol{v}\left(t + \frac{\Delta t}{2}\right)\Delta t \tag{2.5}$$

$$\boldsymbol{r}(t - \Delta t) = \boldsymbol{r}(t) + \boldsymbol{v}\left(t - \frac{\Delta t}{2}\right)\Delta t \tag{2.6}$$

Substituting Eq.(2.4) and Eq.(2.5) into Eq.(2.6) gives:

$$\boldsymbol{r}(t + \Delta t) = 2\boldsymbol{r}(t) - \boldsymbol{r}(t - \Delta t) + \frac{\boldsymbol{F}(t)}{m}\Delta t^2 + O\left(\Delta t^4\right) \tag{2.7}$$

The equations of motion (Eq.(2.1)) are modified for temperature coupling and pressure coupling, both of which are discussed in following sections.

2.4 Interaction function and force field

The potential function, U_{pot}, in Eq.(2.2) can be subdivided into non-bonded and bonded interactions:

$$U_{pot} = U_{non-bond} + U_{bond} \tag{2.8}$$

where $U_{non-bond}$ is the non-bonded interaction energy, which arises from the interaction between distinct atoms, and U_{bond} is the bonded interaction energy, which comes from the interaction between the atoms connected by bond, angle and dihedral in the same molecule.

2.4.1 Non-bonded interactions

The non-bonded interaction energy, $U_{non-bonded}$, in Eq.(2.8) can be subdivided into Lennard-Jones or Buckingham, and Coulomb or modified Coulomb potentials. These non-bonded interactions are computed on the basis of a neighbor list (a list of non-bonded atoms within a certain radius), in which exclusions are already removed. In this dissertation, the Lennard-Jones and Coulomb potentials are introduced:

$$U_{non-bond} = U_{LJ} + U_c \tag{2.9}$$

where U_{LJ} and U_c are the Lennard-Jones and Coulomb potentials, respectively.

Lennard-Jones interaction

Lennard-Jones potential U_{LJ} between atom types i and j are given by:

$$U_{LJ}\left(r_{ij}\right) = 4\epsilon_{ij}\left[\left(\frac{\sigma_{ij}}{r_{ij}}\right)^{12} - \left(\frac{\sigma_{ij}}{r_{ij}}\right)^{6}\right] \tag{2.10}$$

where ϵ_{ij} and σ_{ij} are Lennard-Jones potential parameters, and r_{ij} is the distance between atom i and j. Usually, the Lennard-Jones potential parameters between same atom types, ϵ_{ii} and σ_{ii} are given by empirical or semi-empirical ways and reported as a force field, such as CHARMM (Davis et al., 2008; Klauda et al., 2005; MacKerell Jr et al., 1998), CLAYFF (Cygan et al., 2004) and so on. All Lennard-Jones potential parameters between same atom types, which are used in this dissertation, are listed in Table.A.1. For example, U_{LJ} and the force by LJ potential, F_{LJ} (negative derivative of U_{LJ}, see Eq.(2.2)) between CTL3 and CTL3 are illustrated in Fig.2.1. Note that CTL3 is a name for specifying the atom type (see Table.A.1).

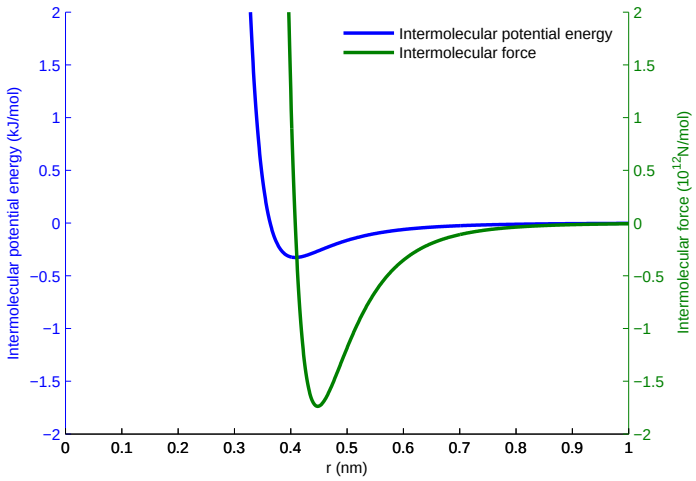

Figure 2.1: Example of U_{LJ} and F_{LJ} between CTL3 and CTL3 atom types.

The Lennard-Jones potential parameters between different atom types, ϵ_{ij} and σ_{ij}, can be obtained by Lorentz-Berthelot combining rules:

$$\sigma_{ij} = \frac{\sigma_{ii} + \sigma_{jj}}{2} \tag{2.11}$$

$$\epsilon_{ij} = \sqrt{\epsilon_{ii}\epsilon_{jj}} \tag{2.12}$$

Fig.2.2 shows the comparison of three kinds of U_{LJ} and F_{LJ} between CTL3 and HAL3.

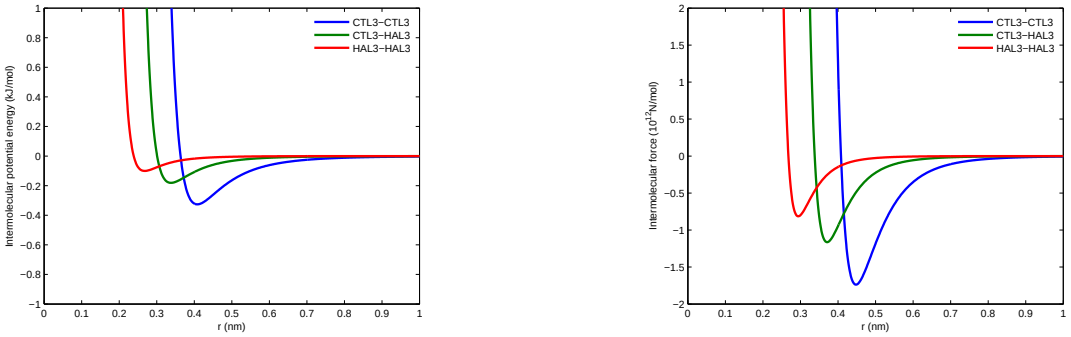

(a) U_{LJ} (b) F_{LJ}

Figure 2.2: Comparison of U_{LJ} and F_{LJ} between CTL3-CTL3, CTL3-HAL3 and HAL3-HAL3.

Coulomb interaction

The Coulomb interaction U_c between two charged atoms is given by:

$$U_c(r_{ij}) = f\frac{q_i q_j}{\epsilon_r r_{ij}} \tag{2.13}$$

where $f = \frac{1}{4\pi\epsilon_0}$, q_i and q_j are the charge on atom i and j, respectively, ϵ_r is relative dielectric constant, which is given in advance. Fig.2.3 shows the example of the Coulomb interaction, which is between CTL3 and CTL3.

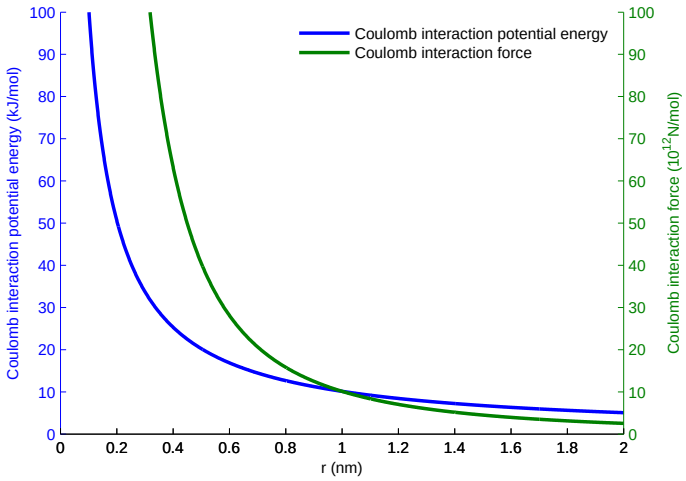

Figure 2.3: Example of U_c and F_c between CTL3 and CTL3 atom types.

2.4.2 Bonded interactions

Bonded interactions are based on a fixed list of atoms. They are not exclusively pair interactions, but include 3- and 4-body interactions as well. There are bond stretching (2-body), bond angle (3-body), and dihedral angle (4-body) interactions.

$$U_{bond} = U_b + U_a + U_d \tag{2.14}$$

where U_b, U_a and U_d are the interaction energies from the bond stretching, bond angle and dihedral angle, respectively.

Bond stretching (2-body)

The bond stretching between two covalently bonded atoms i and j is represented by a harmonic potential:

$$U_b\left(r_{ij}\right) = \frac{1}{2}k_{ij}^{b}\left(r_{ij} - b_{ij}\right)^2 \tag{2.15}$$

where r_{ij} is the distance between atom i and j. The parameters in Eq.(2.15), k_{ij}^{b} and b_{ij}, used in this dissertation are listed in Table.A.2.

Harmonic angle potential (3-body)

The bond angle vibration between a triplet of atoms i, j and k is also represented by a harmonic potential on the angle θ_{ijk}:

$$U_a\left(\theta_{ijk}\right) = \frac{1}{2}k_{ijk}^{\theta}\left(\theta_{ijk} - \theta_{ijk}^{0}\right)^2 \tag{2.16}$$

where θ_{ijk} is the angle between two vectors, $\boldsymbol{r_{ji}}$ and $\boldsymbol{r_{jk}}$. The parameters in Eq.(2.16), k_{ijk}^{θ} and θ_{ijk}^{0}, used in this dissertation are listed in Table.A.2.

Urey-Bradley potential (3-body)

The Urey-Bradley angle vibration between a triple of atoms i, j and k is represented by a harmonic potential on the angle θ_{ijk} and a harmonic correction term on the distance between the atoms i and k. It is used mainly in the CHARMM force field. The Urey-Bradley potential energy is given by:

$$U_a\left(\theta_{ijk}\right) = \frac{1}{2}k_{ijk}^{\theta}\left(\theta_{ijk} - \theta_{ijk}^{0}\right)^2 + \frac{1}{2}k_{ijk}^{UB}\left(r_{ik} - r_{ik}^{0}\right)^2 \tag{2.17}$$

The parameters in Eq.(2.17), k_{ijk}^{θ}, θ_{ijk}^{0}, k_{ijk}^{UB} and r_{ik}^{0}, used in this dissertation are listed in Table.A.3.

Proper dihedrals (4-body)

Proper dihedral angles are defined according to the IUPAC/IUB convention, where ϕ is the angle between the ijk and the jkl planes, with zero corresponding to the cis-configuration (i and l on the same side).

$$U_d\left(\phi_{ijkl}\right) = k_{\phi}\left(1 + \cos\left(n\phi - \phi_s\right)\right) \tag{2.18}$$

The parameters in Eq.(2.18), k_{ϕ}, n and ϕ_s, used in this dissertation are listed in Table.A.4.

2.5 Periodic boundary conditions

The classical way to minimize edge effects in a finite system is to apply periodic boundary conditions (PDC). The atoms of the system to be simulated are put into a space-filling box, which is surrounded by translated copies of itself. Thus, there are no boundaries of the system; the artifact caused by unwanted boundaries in an isolated cluster is now replaced by the artifact of PBC. MD uses PBC, combined with the minimum image convention: only one - the nearest - image of each particle is considered for short-range non-bonded interaction terms. For long-range electrostatic interactions, this is not always accurate enough, and MD therefore also incorporates lattice sum methods like Ewald Sum, PME (Essmann et al., 1995).

2.6 Compute forces

Potential energy

When forces are computed, the potential energy of each interaction term is computed as well. The total potential energy is summed for various contributions, such as Lennard-Jones, Coulomb, and bonded interaction terms (Eq.(2.8)).

Kinetic energy and temperature

The total kinetic energy of the N particle system:

$$E_{kin} = \frac{1}{2}\sum_{i=1}^{N} m_i v_i^2 \tag{2.19}$$

From this the absolute temperature T can be computed using:

$$\frac{1}{2} N_{df} kT = E_{kin} \tag{2.20}$$

where k is Boltzmann's constant and N_{df} is the number of degrees of freedom which can computed from:

$$N_{df} = 3N - N_c - N_{com} \tag{2.21}$$

where N_c is the number of constraints imposed on the system. When performing MD, additional degrees of freedom $N_{com} = 3$ must be removed, because the three center of mass velocities are

constants of the motion, which are usually set to zero. The kinetic energy can also be written as a tensor, which is necessary for pressure calculation.

$$\boldsymbol{E}_{kin} = \frac{1}{2}\sum_{i}^{N} m_i \boldsymbol{v}_i \otimes \boldsymbol{v}_i \tag{2.22}$$

Pressure and virial

The pressure tensor $\boldsymbol{p}$ is calculated from the difference between kinetic energy E_{kin} and the virial term $\boldsymbol{\Xi}$.

$$\boldsymbol{p} = \frac{2}{V}\left(\boldsymbol{E}_{kin} - \boldsymbol{\Xi}\right) \tag{2.23}$$

where V is the volume of the computational box. The scalar pressure P, which can be used for pressure coupling in the case of isotropic systems, is computed as:

$$P = \text{trace}\left(\boldsymbol{p}\right)/3 \tag{2.24}$$

The virial term $\boldsymbol{\Xi}$ is defined as:

$$\boldsymbol{\Xi} = -\frac{1}{2}\sum_{i<j} \boldsymbol{r}_{ij} \otimes \boldsymbol{F}_{ij} \tag{2.25}$$

2.6.1 Temperature coupling

In this dissertation, in order to control the temperature at desired value, both Berendsen (Berendsen et al., 1984) and Nose-Hoover scheme (Nose, 1984) are used.

Berendsen temperature coupling

The Berendsen algorithm mimics weak coupling with first-order kinetics to an external heat bath with given temperature T_0. The deviation of the system temperature from T_0 is slowly corrected according to:

$$\frac{dT}{dt} = \frac{T_0 - T}{\tau} \tag{2.26}$$

This means that a temperature deviation decays exponentially with a time constant τ. The Berendsen thermostat causes the fluctuations of the kinetic energy, which moans that one does not generate a proper canonical ensemble. This dose not matter when simulating larger systems, where most properties are not affected significantly, except for the distribution of the kinetic

energy itself. The heat flow into or out of the system is realized by scaling the velocities of each particle every step with a time-dependent factor λ, which is given by:

$$\lambda = \left[1 + \frac{\Delta t}{\tau_T}\left\{\frac{T_0}{T\left(t - \frac{\Delta t}{2}\right)} - 1\right\}\right]^{\frac{1}{2}} \tag{2.27}$$

The parameter τ_T is calculated by the following relation ship:

$$\tau = \frac{2C_V\tau_T}{N_{df}k} \tag{2.28}$$

where C_V is the total heat capacity of the system, k is the Boltzmann constant, and N_{df} is the total number of degrees of freedom.

Nose-Hoover temperature coupling

The Berendsen thermostat is useful to relax a system to the target temperature. However, once the system has reached equilibrium, it is more important to built correct canonical ensemble. Nose-Hoover thermostat makes it possible to simulate proper canonical ensemble, by introducing a thermal reservoir and a friction term to the system Hamiltonian in the equations of motion. In this algorithm, the equations of motion (Eq.(2.2)) are replaced by:

$$\frac{d^2\boldsymbol{r}_i}{dt^2} = \frac{\boldsymbol{F}_i}{m_i} - \xi\frac{d\boldsymbol{r}_i}{dt} \tag{2.29}$$

where the equations of motion for the heat bath parameter ξ are expressed with target temperature T_0 and instantaneous temperature T:

$$\frac{d\xi}{dt} = \frac{1}{Q}\left(T - T_0\right) \tag{2.30}$$

The parameter Q is obtained by:

$$Q = \frac{\tau_T^2 T_0}{4\pi^2} \tag{2.31}$$

In practice, Berendsen thermostat should be used in the system far away from equilibrium, and after the equilibrium, Nose-Hoover coupling gives more accurate thermodynamic ensemble.

2.6.2 Pressure coupling

Same as the temperature coupling, pressure coupling can be implemented by Berendsen (Berendsen et al., 1984) or Parrinello-Rahman (Parrinello and Rahman, 1982) method.

Berendsen pressure coupling

The Berendsen pressure coupling rescales the coordinates and box vectors every step with a matrix $\boldsymbol{\mu}$, which has the effect of a first-order kinetic relaxation of the pressure to a target pressure $\boldsymbol{P}_0$:

$$\frac{d\boldsymbol{P}}{dt} = \frac{\boldsymbol{P}_0 - \boldsymbol{P}}{\tau_p} \tag{2.32}$$

The scaling matrix $\boldsymbol{\mu}$ is given by:

$$\mu_{ij} = \delta_{ij} - \frac{\Delta t}{3\tau_p}\beta_{ij}\left(P_{0ij} - P_{ij}\left(t\right)\right) \tag{2.33}$$

where β is the isothermal compressibility of the system.

Parrinello-Rahman pressure coupling

It might be a theoretical problem that neither the Berendsen pressure coupling nor the temperature coupling gives exact ensemble. Similar to the Nose-Hoover thermostat, the Parrinello-Rahman pressure coupling is used to run simulations at constant pressure after the system reaches equilibrium. With the Parrinello-Rahman barostat, the box vectors given by the matrix $\boldsymbol{b}$ obey the matrix equation of motion:

$$\frac{d^2\boldsymbol{b}}{dt^2} = V\boldsymbol{W}^{-1}\boldsymbol{b'}^{-1}\left(\boldsymbol{P} - \boldsymbol{P}_{ref}\right) \tag{2.34}$$

where V is the volume of the box, and $\boldsymbol{W}$ is a matrix parameter by which we can determines the strength of the coupling. The matrices $\boldsymbol{P}$ and $\boldsymbol{P}_{ref}$ are the current and target pressures, respectively. The mass parameter matrix $\boldsymbol{W}$ is given by:

$$\left(\boldsymbol{W}^{-1}\right)_{ij} = \frac{4\pi^2\beta_{ij}}{3\tau_p^2 L} \tag{2.35}$$

where β is the approximate isothermal compressibility, τ_p is the pressure time constant and L is the largest box matrix element.

2.7 Thermodynamic ensembles

It is known that the pressure is fixed for a gas sample when the volume and the temperature of the system are maintained, obeying the equation of state in which pressure is a function of volume and temperature. This means that average gas volume over a long enough period of time

follows an equation of state, but instantaneous volume does not. In the microscopic systems dealt with in molecular simulations, instantaneous volume of the system always fluctuates with small time period. Therefore it is necessary to collect multiple snapshots of the microscopic systems for a long enough time to get meaningful average of the thermodynamic properties. In statistical thermodynamics, the collection of snapshots which makes it possible to derive average properties is referred to as statistical ensemble (Feller et al., 1995; Hoover, 1985; Kataoka, 1987; Nose, 1984; Nose and Klein, 1983; Parrinello and Rahman, 1982; Poling et al., 2001; Prausnitz et al., 1998; Zhang et al., 1995).

2.7.1 Canonical ensemble

When computing the thermodynamic properties of a system at fixed volume and temperature, a statistical ensemble called the canonical ensemble (NVT ensemble) is used. The number of molecules N and the volume V kept for all system states belonging to the ensemble, but they differ in total energy E which is fluctuating variable in this ensemble. This fixed temperature does not mean that every system state is at temperature T, but that the energies of the system states have a specific distribution. Each state j of the canonical ensemble occurs with a probability proportional to $\exp\left(\frac{-Ej}{kT}\right)$ where k is the Boltzmann constant and E_j is the total energy of the system in the state j. This is generally expressed as the Boltzmann factor β in statistical mechanics:

$$\beta = \frac{1}{kT} \tag{2.36}$$

The probability that the state j occurs in the canonical ensemble is given by:

$$P_j = \frac{\exp\left(-\beta E_j\right)}{Q_{NVT}} \tag{2.37}$$

Q_{NVT} in this expression is partition function, which is imply the summation of the Boltzmann factors for all possible distinct state in the ensemble:

$$Q_{NVT} = \frac{1}{N!}\sum_{r_i}\sum_{p_i}\exp\left(-\beta E\left(r_i, p_i\right)\right) \tag{2.38}$$

To make it consistent with quantum mechanics, the finite summation is transformed in a continuous integral:

$$Q_{NVT} = \frac{1}{h^{3N}N!}\int_{r_i}\int_{p_i}\exp\left(-\beta E\left(r_i, p_i\right)\right) dr_i dp_i \tag{2.39}$$

where h is the Plank constant and the factor h^{3N} is the volume of an individual quantum state. Assuming that we have a finite collection of system states belonging to the statistical ensemble, where each state occurs in proportion to the Boltzmann factor, average properties can be obtained by simply averaging over the n states belonging to the ensemble. Such averages, commonly expressed $\langle X \rangle$ is given by:

$$\langle X \rangle = \frac{1}{n} \sum_{i=1}^{n} X_i \tag{2.40}$$

Other statistical ensembles can be defined in the same way as the canonical ensemble, depending on which intensive variable are fixed and which associated extensive variable fluctuates.

2.7.2 NPT ensemble

When simulating a system at imposed pressure and temperature, the isothermal-isobaric ensemble, also called NPT ensemble, where volume and energy are fluctuating variables, is used. The probability of occurance of the system states belonging to the ensemble is proportional to:

$$\exp\left(-\beta E_j - \beta P V_j\right) \tag{2.41}$$

2.7.3 NPnAT ensemble

NPnAT ensemble is one type of NPT ensemble. It is useful to simulate the system with interfaces (Allen and Tildesley, 1989; Feller et al., 1995; Israelachvili, 2011; Zhang et al., 1995). Fig.2.4 is a schematic of an interfacial system with two immiscible liquids. The difference between NPT and NPnAT ensembles is just on how to control the pressure. In NPT ensemble, the pressure is controlled isotropically. That is, all box lengths are updated as keeping them at same ratio during MD simulation. On the other hand, in NPnAT ensemble, the pressure on only one direction is controlled, and the box length on this direction are changed. The area which is tangential to the controlled pressure are fixed during MD simulation. This is convenient when the interfaces are set on the plane of the fixed area. In this case, the bulk pressure in each phase can be controlled to the target value.

2.8 Energy Minimization

When a initial system is prepared, that has the configuration where forces between molecules are extremely high. Therefore, an energy minimization should be done before the MD simulation.

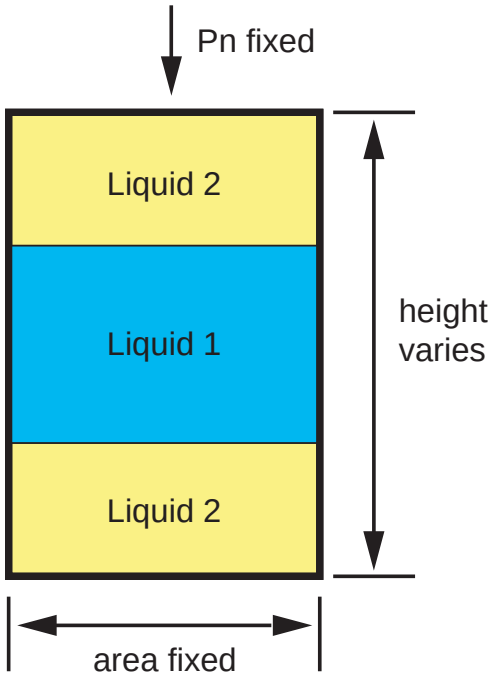

Figure 2.4: Schematic of a liquid–liquid system as simulated by NP_nAT ensemble, modified from Zhang et al. (1995). The interfacial areas are fixed. The pressure normal to the interfaces is kept at a target value by varying height of the system.

In this dissertation, the steepest descent method is used for an energy minimization process. In this method, first, the forces and potential energy are calculated. New positions are calculated by:

$$\boldsymbol{r}_{n+1} = \boldsymbol{r}_n + \frac{\boldsymbol{F}_n}{\max\left(|\boldsymbol{F}_n|\right)} h_n \tag{2.42}$$

where h_n is the maximum displacement and $\boldsymbol{F}_n$ is the force, derived from the negative gradient of the potential U. $\max\left(|\boldsymbol{F}_n|\right)$ means the largest of the absolute values of the force components. The new positions are accepted or rejected according to following algorithm:

If $U_{n+1} < U_n$, the new positions are accepted and $h_{n+1} = 1.2h_n$.

If $U_{n+1} \geq U_n$, the new positions are rejected and $h_{n+1} = 0.2h_n$.

The algorithm stops when the maximum of the absolute values of the force component is smaller than a specified value ϵ.

Chapter 3

Molecular Dynamics of Multicomponent-Oil–Water Interface System

3.1 Introduction

As mentioned in Chapter 1, experimental measurements for liquid–liquid interface are still challenging (De Serio et al., 2006; Du et al., 1994; Lambert et al., 2009; Mitrinovic et al., 2000; Nomoto and Onishi, 2007; Scatena et al., 2001) because of the relatively small sizestypically only a few molecular diameters widesand the buried nature of the interface. In the past, much experimental work has been carried out to understand the properties of water next to hydrophobic surfaces (Du et al., 1994; Scatena et al., 2001), including the orientation of water and its hydrogen bonding. However, there has been little exploration of the structural properties of oil next to the interface. Although computational approaches such as Molecular Dynamics (MD) and Monte Carlo simulations can provide insights into the structural properties of oil–water interfacial systems, most studies have been limited to the stable interfacial structure of a pure hydrocarbon-water system (Biscay et al., 2009; Bresme et al., 2008; Kereszturi and Jedlovszky, 2005; Linse, 1987; Nicolas and de Souza, 2004; Patel and Brooks, 2006; van Buuren et al., 1993) or that with surfactant (Jang et al., 2004). However, crude oil is a highly complex material (Lake, 1989; Pedersen and Christensen, 2006) that consists mainly of hydrocarbons but can hardly be described as a single hydrocarbon phase. In particular, it is widely accepted that the percentage contents of paraffinic (alkane), naphthenic (cycloalkane), and aromatic components in reservoir

fluids (often referred to as the PNA distribution) are essential properties when describing crude oil (Pedersen and Christensen, 2006). Recent experimental studies have reported that trace impurities can significantly modify the interfacial tension, by up to 10-20 mN/m, over a period of a few hours (Mitrinovic et al., 2000). Theoretical investigations have also shown that even mixtures containing only n-alkanes exhibit exotic phenomena compared with a single-component system (Xia and Landman, 1993).

Here, we present a more realistic light-oil model. The purpose of this work was to study the molecular organization and the interfacial properties of a complex oil–water interface system and to compare these results with those of pure hydrocarbon–water interface systems. Three types of system were used for the interfacial simulations: a light-oil model–water interface system, pure hydrocarbon–water interface systems, and a hep-tol (1:1 mixture of heptane and toluene, by volume)–water interface system. In previous studies, a small number of hydrocarbons were typically employed to investigate the oil–water interfaces, which resulted in low statistical accuracy regarding the structural properties (e.g., insufficient resolution on the density profile), thereby obscuring the structural features (Kereszturi and Jedlovszky, 2005; Linse, 1987; van Buuren et al., 1993). To overcome this difficulty, large-scale MD simulations were engaged in this work. A typical interface system contained approximately 1000 hydrocarbon molecules and 7,000-8,000 H_2O molecules, giving a total of about 50,000 atoms.

3.2 Computational Methods

The light-oil model we used in this study was modeled as a mixture of eight hydrocarbons: hexane, heptane, octane, nonane, cyclohexane, cycloheptane, benzene, and toluene. The chemical formulas and structures are shown in Table.3.1. All alkanes are modeled as linear ones, called normal-alkanes, usually described as with a prefix of n-. The number of each molecule in unit cell and the mole fraction of each molecule in initial oil phase are shown in Table.3.2. The composition has high relevance to light crude oil in Japanese oil fields and is typical for modeling gasoline. MD simulations were performed using the GROMACS package (Hess et al., 2008). The water molecules were modeled by SPC/E (single point charge/extended) (Alejandre et al., 1995; Berendsen et al., 1987), as it can reproduce the surface tension of water and orthobaric densities as well as other structural properties of liquid water (Alejandre et al., 1995). A revised version of the CHARMM27 force field (Davis et al., 2008; Klauda et al., 2005; MacKerell Jr

et al., 1998) was used to model the hydrocarbons, except for benzene, where different charges were used (see below for an explanation).

Table 3.1: Chemical formulas and structures of hydrocarbons and water molecules for the light-oil–water interface system.

Component	formula	Structure
n-hexane	C_6H_{14}	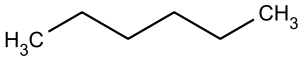
n-heptane	C_7H_{16}	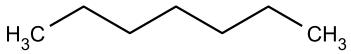
n-octane	C_8H_{18}	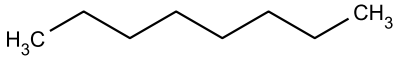
n-nonane	C_9H_{20}	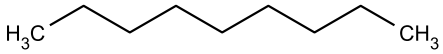
cyclohexane	C_6H_{12}	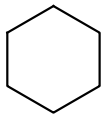
cycloheptane	C_7H_{14}	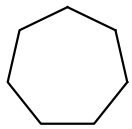
benzene	C_6H_6	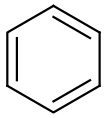
toluene	C_7H_8	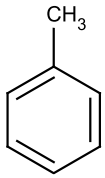
water	H_2O	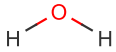

Fig.3.1 shows the schematic flow how to make the oil–water interface system. First, the light-oil box was calculated from isobaric-isothermal ensemble (NPT) simulation. Then the water box was calculated from the isobaric-isothermal-isointerface area ensemble (NPnAT) simulation (See Chapter 2). Finally, the interface system was made by combining each other and performed in the NPnAT simulation. Same procedures were used for calculating the pure hydrocarbon–water interface systems.

In all calculations after equilibration process, the temperature was controlled by the Nose-

Table 3.2: Compositions in the light-oil model–water interface system

Phase	Component	No. in the simulation box	Mole fraction
Light-oil	n-hexane	144	0.133
	n-heptane	132	0.122
	n-octane	156	0.144
	n-nonane	180	0.167
	cyclohexane	96	0.089
	cycloheptane	156	0.144
	benzene	60	0.056
	toluene	156	0.144
Water	water	8,449	

Hoover thermostat (Nose, 1984), and the pressure was controlled by the Parrinello-Rahman method (Parrinello and Rahman, 1982). The particle mesh Ewald summation (Essmann et al., 1995) was used for the electrostatic interactions, and a cutoff of 1.4 nm was used for the van der Waals interactions. A 1.0 fs time step was used and the coordinates output every 1.0 ps.

3.3 Results and Discussion

3.3.1 Densities and interfacial tensions for pure hydrocarbon case.

The accuracy of each hydrocarbon model were confirmed by comparing their thermodynamic properties with experimental ones. The equilibrium densities of the pure hydrocarbons from NPT simulation 298 K and 0.1 MPa are shown in Table.3.2. The densities of n-alkanes and aromtaics were in excellent agreement with experimental values (Lemmon et al., 2005). The densities of cycloalkane were slightly lower than experimental values, but the differences are only less than 3%. More importantly, the hierarchy of the densities of the n-alkanes, cycloalkanes, and aromatics was well-reproduced.

Then the interface equilibrium of the pure hydrocarbon and water were investigated by using MD methods from NPnAT ensemble. Fig.3.2 shows the density profiles at the vicinity of their interfaces for all system. The density profiles of both hydrocarbon and water in all systems change gradually from their own phase to the another phase, and make clear interfaces. The interactions between the hydrocarbons and water molecules reproduce their immiscibility

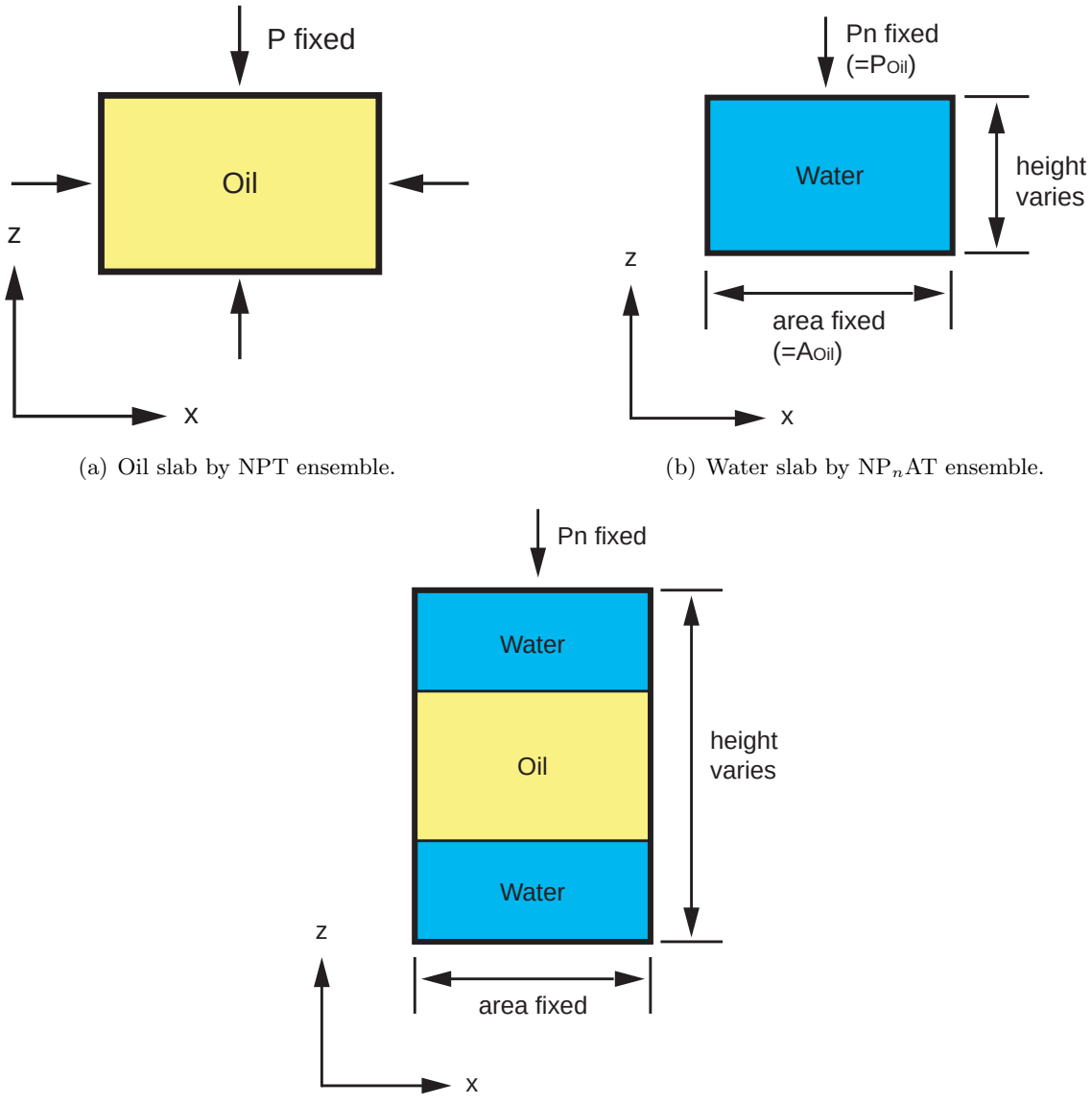

(a) Oil slab by NPT ensemble.

(b) Water slab by NP$_n$AT ensemble.

(c) Oil-water system by NP$_n$AT ensemble.

Figure 3.1: Schematic flow how to make oil–water interface system.

Table 3.3: Densities of pure hydrocarbons and interfacial tensions of the hydrocarbon–water interface systems at 298 K and 0.1 MPa

System	Density (kg/m^3)		Interfacial tension with SPC/E water (mN/m)	
	MD	Experiment[a]	MD	Experiment
n-hexane	654.27	654.92	50.73	50.5[b], 51.4[c], 49.7[d]
n-heptane	679.64	679.72	51.96	51.9[c], 50.2[d]
n-octane	699.12	698.39	52.72	50.7[b], 52.5[c], 50.2[d]
n-nonane	715.70	714.21	52.77	50.9[b], 52.4[c]
cyclohexane	754.02	774.03	49.53	49.6[b], 50.0[d]
cycloheptane	791.37	811.00	53.48	
benzene	874.74	873.83	34.42	34.4[b], 35.8[e], 33.7[f], 34.7[d]
toluene	867.45	862.38	37.69	36.0[e], 36.4[f], 36.1[d]

[a] Lemmon et al. (2005). [b] Rehfeld (1967). [c] Goebel and Lunkenheimer (1997).
[d] Donahue and Bartell (1952). [e] Yeung et al. (1998). [f] Moran et al. (1999).

correctly. All bulk densities of water phase (left side in each panel of Fig.3.2) were around 1,000 kg/m^3 and in good agreement with the experimental value. And also, the bulk densities of hydrocarbon phase (right side in each panel of Fig.3.2) were almost same with those obtained from pure NPT calculations (Table.3.3).

The interfacial tension can be calculated from the MD results (Chapela et al., 1977; Harris, 1992; Kirkwood and Buff, 1949; Lopez-Lemus et al., 2008; Senapati and Berkowitz, 2001). The instantaneous interfacial tension, $\gamma(t)$, is defined as:

$$\gamma(t) = \int \left[p_{nn}(n,t) - p_{tt}(n,t)\right] dn \tag{3.1}$$

where n is the axis normal to the interface, and hence p_{nn} and p_{tt} are normal and tangential component, respectively, of the pressure tensor $\boldsymbol{p}$ (Eq.(2.23)). The integral in Eq.(3.1) should be carried out from the bulk position of one phase to that of another phase. The interfacial tension, γ, can be calculated by averaging $\gamma(t)$ over the simulation time:

$$\gamma = \langle \gamma(t) \rangle \tag{3.2}$$

In our case, since the z axis is perpendicular to the interfaces, Eq.(3.1) becomes

$$\gamma(t) = \int \left[p_{zz}(z,t) - \frac{p_{xx}(z,t) + p_{yy}(z,t)}{2}\right] dz \tag{3.3}$$

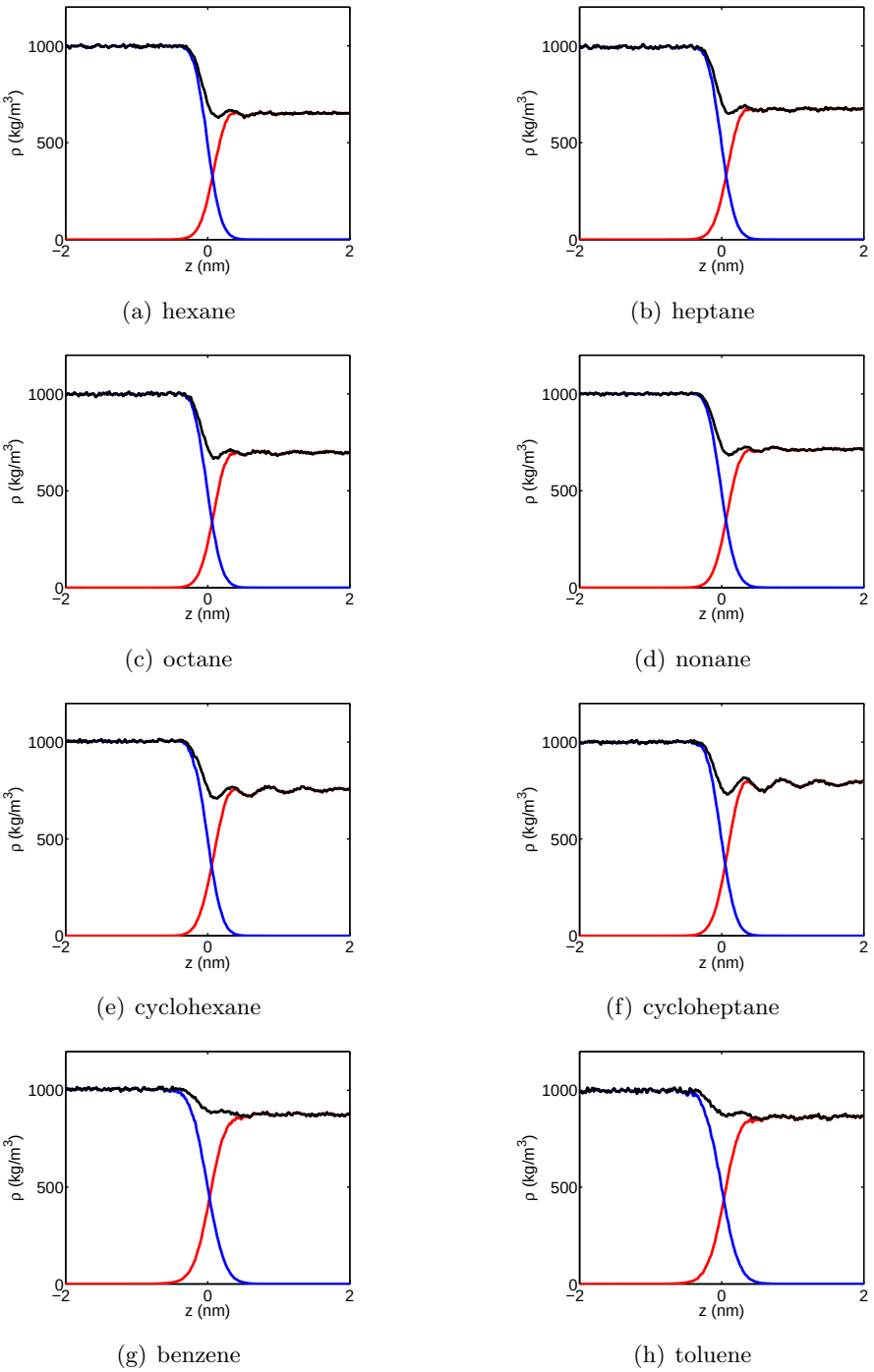

(a) hexane (b) heptane

(c) octane (d) nonane

(e) cyclohexane (f) cycloheptane

(g) benzene (h) toluene

Figure 3.2: Density profiles of hydrocarbon–water interface systems (black; total, red; hydrocarbon, blue; water). Shown only at the vicinity of each interface. Left side of each panel corresponds to water phase and right side corresponds to each hydrocarbon phase.

In our MD simulations, the instantaneous pressure, P_i $(i = x, y, z)$, for each direction can be described as:

$$\begin{aligned} P_i(t) &= \frac{1}{V} \iiint_V p_{ii}(x, y, z, t)\, dxdydz \\ &= \frac{1}{L_z} \int p_{ii}(z, t)\, dz \end{aligned} \tag{3.4}$$

where L_z is the box length in the z direction. So, Eq.(3.3) can be rewritten as:

$$\gamma(t) = L_z \left(P_z(t) - \frac{P_x(t) + P_y(t)}{2} \right) \tag{3.5}$$

Finally, Eq.(3.2) becomes:

$$\gamma = \left\langle L_z \left(P_z(t) - \frac{P_x(t) + P_y(t)}{2} \right) \right\rangle \tag{3.6}$$

Since our system has two interfaces, Eq.(3.2) should be divided by 2.

$$\gamma = \frac{1}{2} \left\langle L_z \left(P_z(t) - \frac{P_x(t) + P_y(t)}{2} \right) \right\rangle \tag{3.7}$$

Fig.3.3 shows the rolling averages of the instantaneous interfacial tensions for the pure hydrocarbon–water interface system from the beginning to arbitrarily time. As shown in Fig.3.3, all interfacial tensions show good convergence. The interfacial tensions averaged over 3ns of simulation are presented in Table.3.3, and are also in good agreement with experimental data (Donahue and Bartell, 1952; Goebel and Lunkenheimer, 1997; Moran et al., 1999; Rehfeld, 1967; Yeung et al., 1998). The interfacial tensions of n-alkanes and cycloalkanes with the SPC/E water are around 50 mN/m, whereas those of aromatics with SPC/E water are around 35 mN/m, 15 mN/m lower than those of n-alkanes and cycloalkanes. Therefore, each hydrocarbon model reasonably served as a component in the light–oil model.

3.3.2 Light-oil model and water interface: self-accumulation of the aromatics.

The interface between the light-oil model and water were investigated. As mentions above, the light-oil model was modeled as a mixture of above eight kinds of hydrocarbons. A typical snapshot of the light-oil model is shown in Fig.3.4. Since all hydrocarbons are miscible each other, the light-oil model becomes one phase. And as shown, all hydrocarbons distribute homogeneity in the light-oil phase.

Then the light-oil model was combined with water slab, which was prepared independently. A typical snapshot of a unit cell for the MD simulation of the interface system under 298 K and

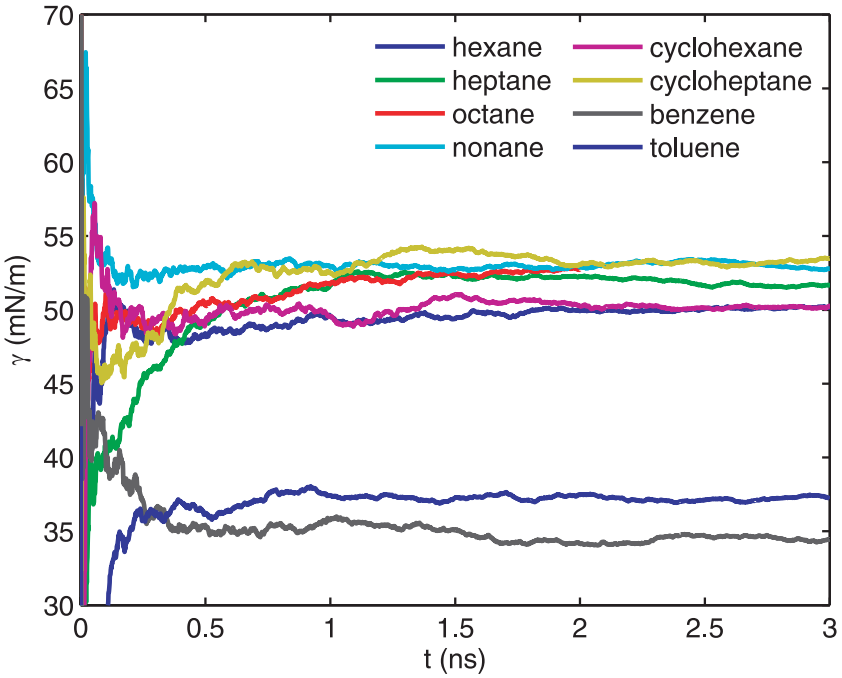

Figure 3.3: Rolling averages of instantaneous interfacial tensions for pure hydrocarbon–SPC/E water interface systems.

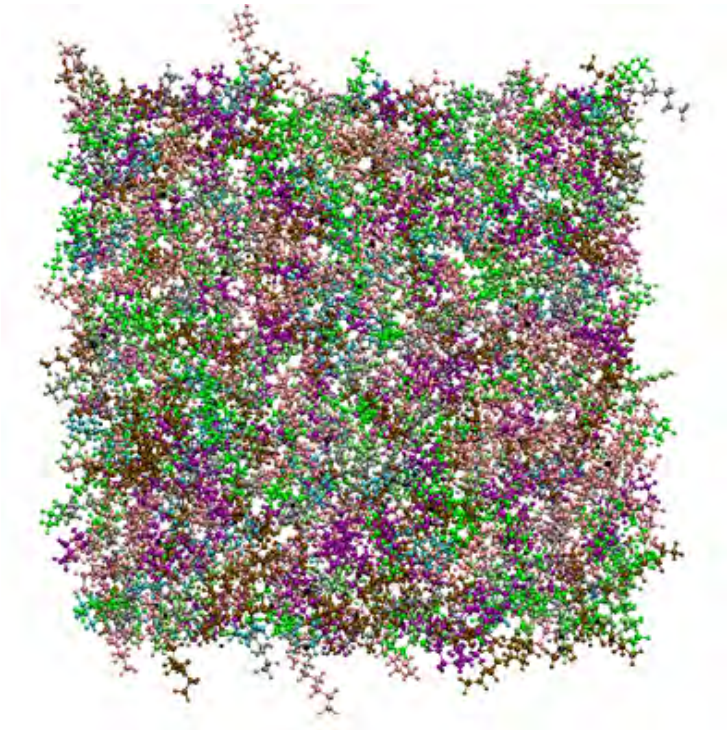

(a) Snapshot of the light-oil model.

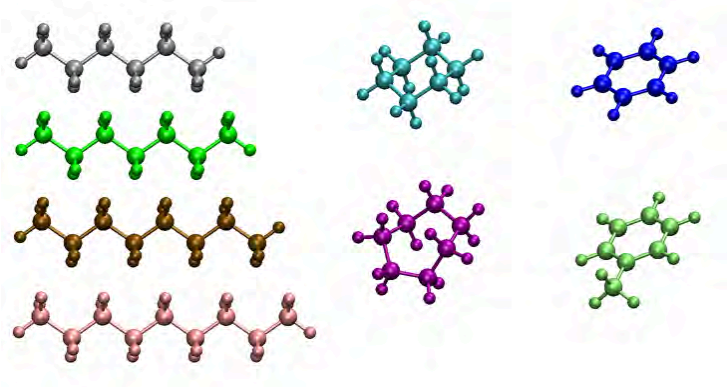

(b) Color Specification for Fig.3.4(a).

Figure 3.4: Snapshots for the light-oil model.

0.1 MPa is shown in Fig.3.5. Note that Fig.3.5 uses different colors for specifying molecule from in Fig.3.4. The density profiles across the light-oil model–water interface system after NPnAT equilibration at 298 K and 0.1 MPa, and at 400 K and 30 MPa are illustrated in Fig.3.6. The accumulations of aromatics (benzene and toluene) at the interface of water and the light-oil model were observed at all the thermal conditions we studied. The interface system can be divided into three regions: the water region, the interface region (that is, the aromatics-rich region), and the bulk oil region. Fig.3.7 shows the relative density profiles of each component at the vicinity of the light-oil and water interface. At 298 K and 0.1 MPa, the maximum densities of aromatics (both benzene and toluene) in the interface region are 3.5-4.0 times higher than their densities in the bulk oil region. This value approaches 1.8 at a typical reservoir condition of 400 K and 30 MPa.

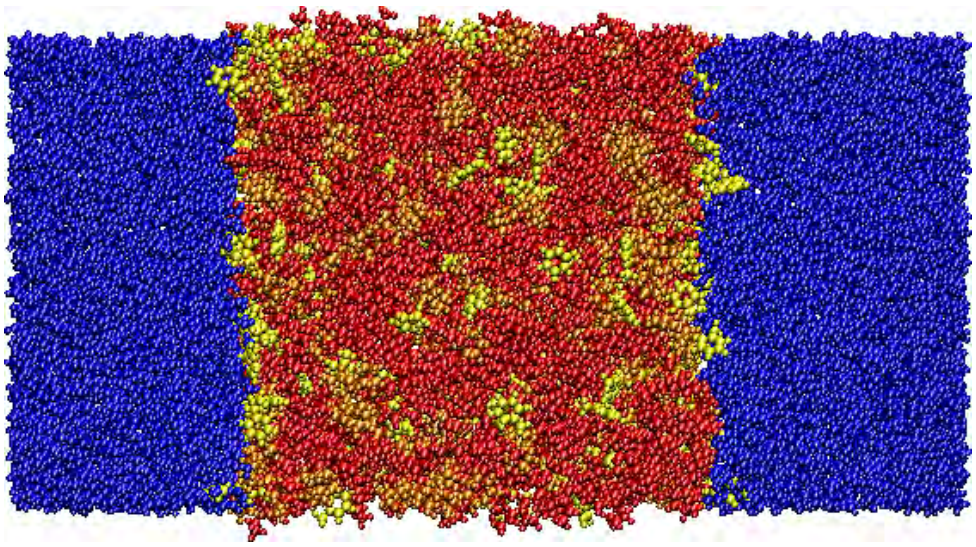

Figure 3.5: Snapshot of the light-oil model–water interface system at 298 K and 0.1 MPa after 5.0 ns of NPnAT simulation (red, n-alkanes; orange, cycloalkanes; green, aromatics; blue, water).

The calculated interfacial tension of the light-oil–water interface system at 298 K and 0.1 MPa is 47.49 mN/m or 5 mN/m lower than that of a typical n-alkane–water interface system. It is noteworthy that such an aromatic concentration is not observed at pure hydrocarbon–water interfaces, including benzene–water and toluene–water (Fig.3.2). In summary, the aromatics (though not amphiphilic) are surface-active at the oil–water interface but are inactive at the pure aromatics–water interface. We hypothesize that the accumulation is driven by the inherent interfacial tension difference between aromatics–water and the other potential hydrocarbons–water

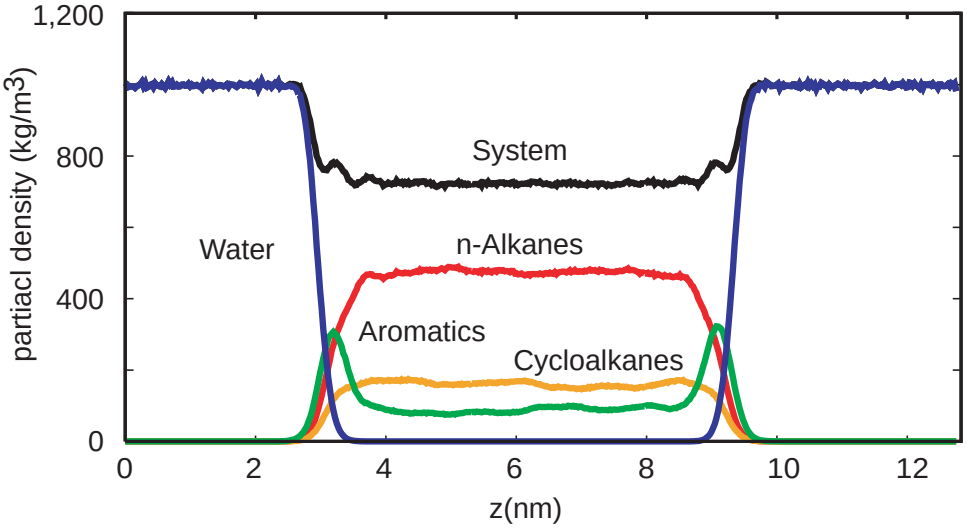

(a) 298 K and 0.1 MPa.

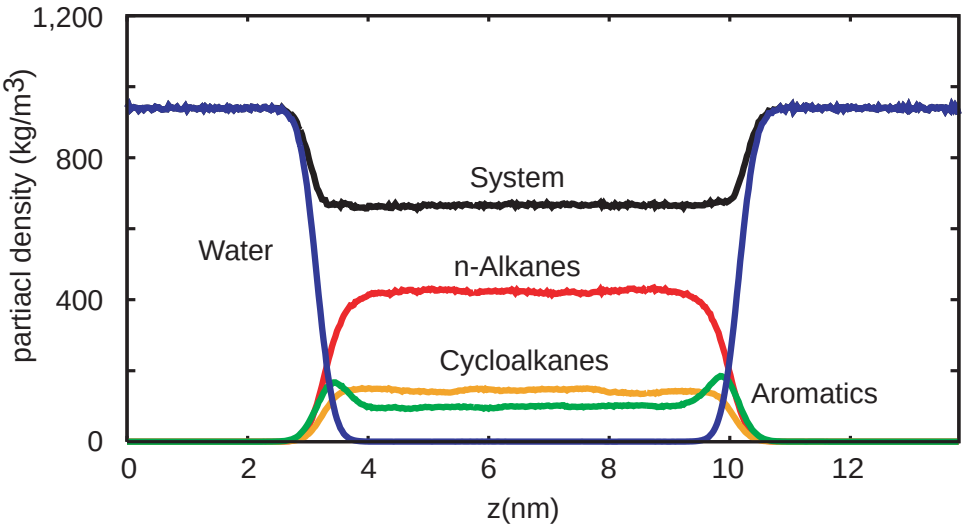

(b) 400 K and 30 MPa.

Figure 3.6: Partial density profiles along the z-axis averaged over 3.0–5.0 ns.

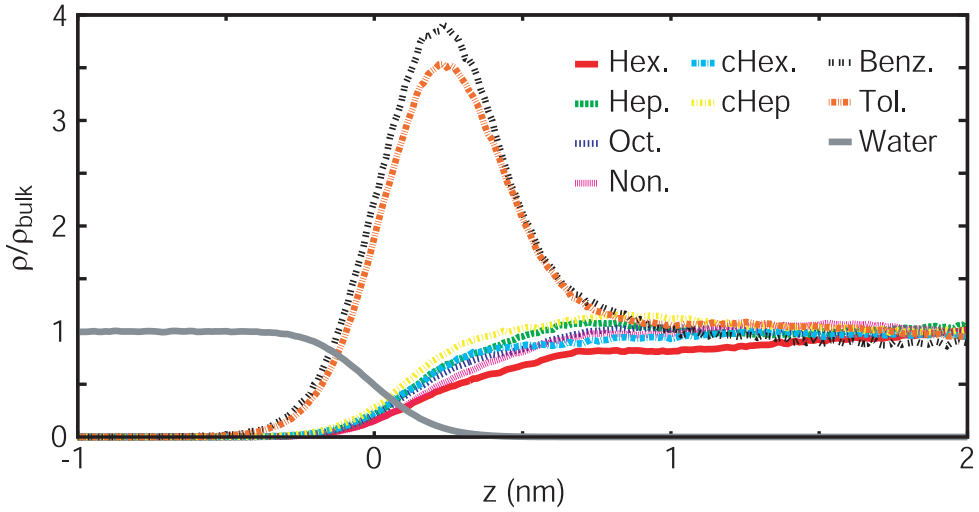

(a) 298 K and 0.1 MPa.

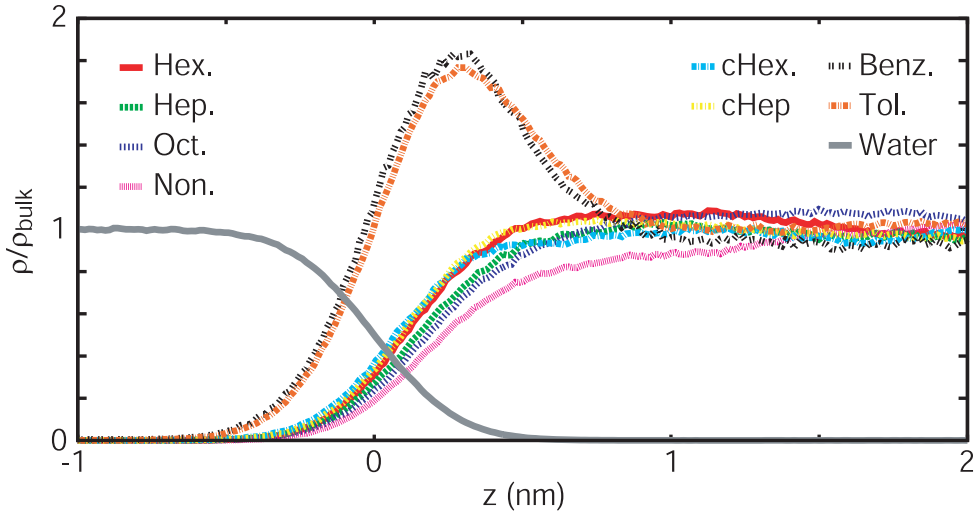

(b) 400 K and 30 MPa.

Figure 3.7: Relative partial density profiles of each component near the interface.

interface combinations. When aromatic molecules accumulate at the interface, the configuration entropy, S, decreases, similar to the case for the adsorption of surfactants and alkanols (Takiue et al., 1998), and the Gibbs free energy increases within the interface system. On the other hand, the interfacial tensions of the aromatics are 10-15 mN/m lower than those of n-alkanes and cycloalkanes (Table.3.3) so the accumulation of aromatics causes a decrease in interfacial tension, γ, therefore decreasing the potential energy of the total system. Consequently, the Gibbs free energy reaches a minimum value with the accumulation of aromatics at equilibrium (Guggenheim, 1945).

3.3.3 Hep-Tol-Water interface: interfacial tension difference is the driving force of the accumulation.

To corroborate our hypothesis, a hep-tol–water system was prepared in an ad hoc manner. The composition of the hep-tol–water interface system is shown in Table.3.4. The numbers of heptane and toluene molecules in the hep-tol phase were set as their mixture became a 1:1 ratio by volume. Fig.3.8 shows the density profiles for the hep-tol–water system after NPnAT equilibration. As anticipated, the accumulation of toluene at the hep-tol–water interfaces was observed. Similar to the light-oil–water interface system, the density profiles can be divided into three regions: the water region, the interface region (i.e., the toluene-rich region), and the bulk hep-tol region. The density of the bulk hep-tol region (4 nm $<$ z $<$ 8 nm) was 760 kg/m^3, which is slightly lower than that of the pure hep-tol system (773.19 kg/m^3). This occurs simply because the amount of toluene in the bulk hep-tol region is reduced due to the accumulation of toluene at the interface so that the hep-tol region is no longer a 1:1 mixture, by volume, of heptane and toluene. The maximum concentration of toluene at the interface region is nearly 1.6 times larger than that in the bulk hep-tol region. Note that the amount of accumulation of toluene may differ when the ratio of the interface area over the bulk hep-tol volume is varied. From the density profiles, the surface excess of toluene was estimated to be 3.68 (0.11 $\times$ 10^{-6} mol/m^2 by taking the average for 3.0-5.0 ns, which is in fairly good accordance with the one calculated by Gibbs adsorption equation 2.93 $\times$ 10^{-6} mol/m^2. The calculated interfacial tensions for the hep-tol–water system is 42.27 mN/m, lower than the algebraically averaged value (44.82 mN/m) for the heptane–water (51.96 mN/m) and the toluene–water (37.69 mN/m) systems. The lowered interfacial tension should thus result from the accumulation of toluene at the hep-tol–water interface. Interestingly, the measured value is reported to be around 40 mN/m (Goebel and Lunkenheimer, 1997; Yeung et al., 1998), which is somewhat lower than our calculated value.

This disparity is not a failure of the force field we used but rather may be direct proof that the interfacial tension of the hep-tol–water interface is a function of the ratio between the volume and the interface area of the heptane–toluene phase. Recall that the ratio between the volume and interface area in our MD calculation (6.4 nm) is extremely small compared with that of the experiment (167,000 nm, Yeung et al. (1998)). To confirm this, we performed two additional simulations, one at a lower volume-area ratio of 3.3 nm and the other at a higher ratio of 9.5 nm. The interfacial tensions were increased to 43.64 or reduced to 42.08 mN/m, respectively. In other words, the interfacial tension of this system is not an intrinsic property of the interface but shows clear evidence of surfactant-like behavior (of toluene) (Yeung et al., 1998). In summary, the results of the hep-tol–water interface system support our hypothesis that the accumulation is due to the mixing effects of the aromatics and the other hydrocarbons, namely, the interfacial tension difference is the driving force of accumulation of aromatics.

Table 3.4: Composition of the Hep-Tol–water interface system.

System	Component	No. in the simulation box
Hep-Tol	n-heptane	500
	toluene	694
Water	Water	8,449

3.3.4 Weak hydrogen bonding between aromatics and water.

In the following, we show that the reason the aromatics–water interface has a lower interfacial tension is that there is attractive weak hydrogen bonding between aromatic molecules and water molecules (Allesch et al., 2008; Graziano and Lee, 2001; Raschke and Levitt, 2005; Schravendijk and van der Vegt, 2005; Suzuki et al., 1992). For this analyses, the radial distribution functions (RDF, or pair correlation function) were used. The RDF $g_{AB}(r)$ between particles of type A and B is defined in the following way:

$$\begin{aligned} g_{AB}(r) &= \frac{\langle \rho_B(r) \rangle}{\langle \rho_B \rangle_{local}} \\ &= \frac{1}{\langle \rho_B \rangle_{local}} \frac{1}{N_A} \sum_{i \in A}^{N_A} \sum_{i \in B}^{N_B} \frac{\delta(r_{ij} - r)}{4\pi r^2} \end{aligned} \tag{3.8}$$

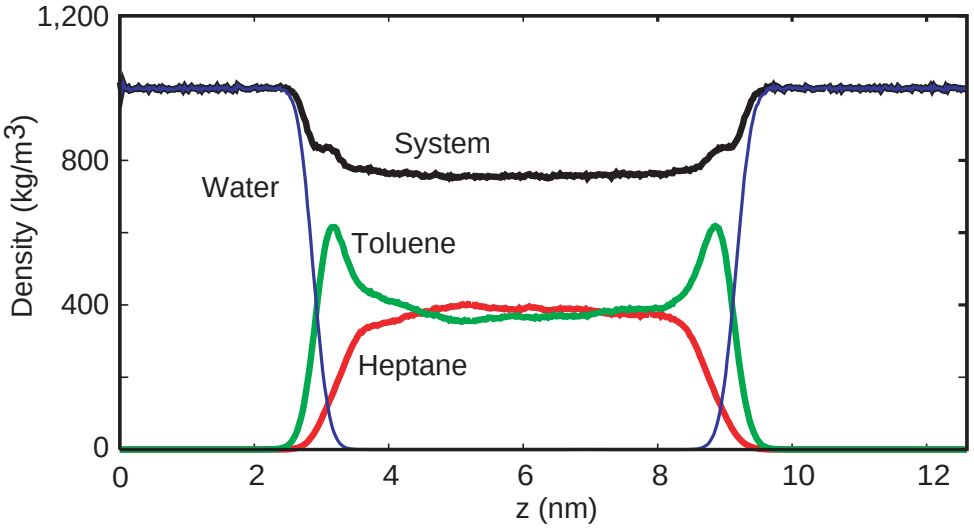

Figure 3.8: Partial density profiles for hep-tol–water interface system along the z-axis averaged over 3.0–5.0 ns.

where $\langle \rho_B(r) \rangle$ is the particle density of atom B at a distance r around atom A, and $\langle \rho_B \rangle$ is the particle density of atom B averaged over all spheres around atom A. Eq.(3.8) can be separated into axial and equatorial parts as follows.

$$\begin{aligned} g_{AB}^{axial}(r) &= \frac{\langle \rho_B^{axial}(r) \rangle}{\langle \rho_B \rangle_{local}} \\ &= \frac{1}{\langle \rho_B \rangle_{local}} \frac{1}{N_A} \sum_{i \in A}^{N_A} \sum_{i \in B}^{N_B} \frac{\delta^{axial}(r_{ij} - r)}{4\pi r^2 (1 - \cos\phi)} \end{aligned} \tag{3.9}$$

and

$$\begin{aligned} g_{AB}^{equatorial}(r) &= \frac{\langle \rho_B^{equatorial}(r) \rangle}{\langle \rho_B \rangle_{local}} \\ &= \frac{1}{\langle \rho_B \rangle_{local}} \frac{1}{N_A} \sum_{i \in A}^{N_A} \sum_{i \in B}^{N_B} \frac{\delta^{equatorial}(r_{ij} - r)}{4\pi r^2 \cos\phi} \end{aligned} \tag{3.10}$$

where

$$\delta^{axial}(r_{ij} - r) = \begin{cases} 1 & \text{if } 0 \le \theta \le \phi, \text{ or } \pi - \phi \le \theta \le \pi, \\ 0 & \text{elsewhere} \end{cases} \tag{3.11}$$

and

$$\delta^{equatorial}(r_{ij} - r) = \begin{cases} 1 & \text{if } \phi \le \theta \le \pi - \phi, \\ 0 & \text{elsewhere} \end{cases} \tag{3.12}$$

where $\langle \rho_B^{axial}(r) \rangle$ and $\langle \rho_B^{equatorial}(r) \rangle$ are the particle density of atom B at a distance r around atom A in axial and equatorial region, respectively, θ is the angle between a base axis and vector AB, and ϕ is the dividing angle between axial and equatorial region.

Fig.3.9 shows normal (total), axial and equatorial RDFs between the center of hexane, cyclohexane, benzene, and the hydrogen or oxygen atoms in water molecules in each hydrocarbon–water interface system. In sharp contrast to the hexane–water and the cyclohexane–water interface systems (which have only one peak at around $r = 0.5$ nm, b, c, e and f in Fig.3.9), the total RDF, g_{total}, in the benzene–water interface system has two peaks (h and i in Fig.3.9). To explain why these two peaks appear, the total RDFs in the cyclohexane–water and benzene–water interface system were divided into two regions: the axial and equatorial regions, $g_{axial}(r)$ and $g_{equatorial}(r)$ (as shown in d and g in Fig.3.9), respectively. The RDFs are defined by $g_{total} = g_{axial}(r)(1 - \cos\phi) + g_{equatorial}(r)\cos\phi$, where ϕ is the dividing angle between the axial and equatorial regions. In the present case, ϕ was set to 20 °. The first peaks of each g_{total} in the benzene-water interface system are mainly contributed by $g_{axial}(r)$ (h and i in Fig.3.9). In particular, the $g_{benzene-H}$ and $g_{benzene-O}$ show maximum values at z = 0.23 and 0.33 nm, respectively. The difference is exactly 0.1 nm, a value close to the OH bond length in the water molecule. We therefore, confirm the picture of weak hydrogen bonding, i.e., the nearest water molecule in the axial region tends to point its proton toward the benzene ring.

To investigate and compare the details of this local structure, one additional MD calculation of the solution system (one benzene molecule and 2,176 water molecules) was performed at 298 K and 0.1 MPa. For further discussion, the angle dependent RDF was defined as follows.

$$\begin{aligned} g_{AB}(r,\theta) &= \frac{\langle \rho_B(r,\theta) \rangle}{\langle \rho_B \rangle_{local,\theta}} \\ &= \frac{1}{\langle \rho_B \rangle_{local,\theta}} \frac{1}{N_A} \sum_{i \in A}^{N_A} \sum_{i \in B}^{N_B} \frac{\delta(r_{ij} - r)\,\delta(\theta_{ij} - \theta)}{2\pi r^2 \sin\theta} \end{aligned} \tag{3.13}$$

where $\langle \rho_B(r,\theta) \rangle$ is the particle density of atom B at a distance r and angle θ around atom A.

$$\cos\theta_{ij} = \frac{\boldsymbol{r}_{ij} \cdot \boldsymbol{e}}{\|r_{ij}\| \|e\|} \tag{3.14}$$

Fig.3.10 shows the angle dependent RDFs for this artificial solution and the benzene–water interface system. In both systems, $g_{benzene-H}$ and $g_{benzene-O}$ show maximum values at z = 0.21 and 0.31 nm, respectively, at an angle of less than 20 °. The nearest water molecule to benzene locates well in the normal direction to the benzene ring, and its hydrogen is oriented

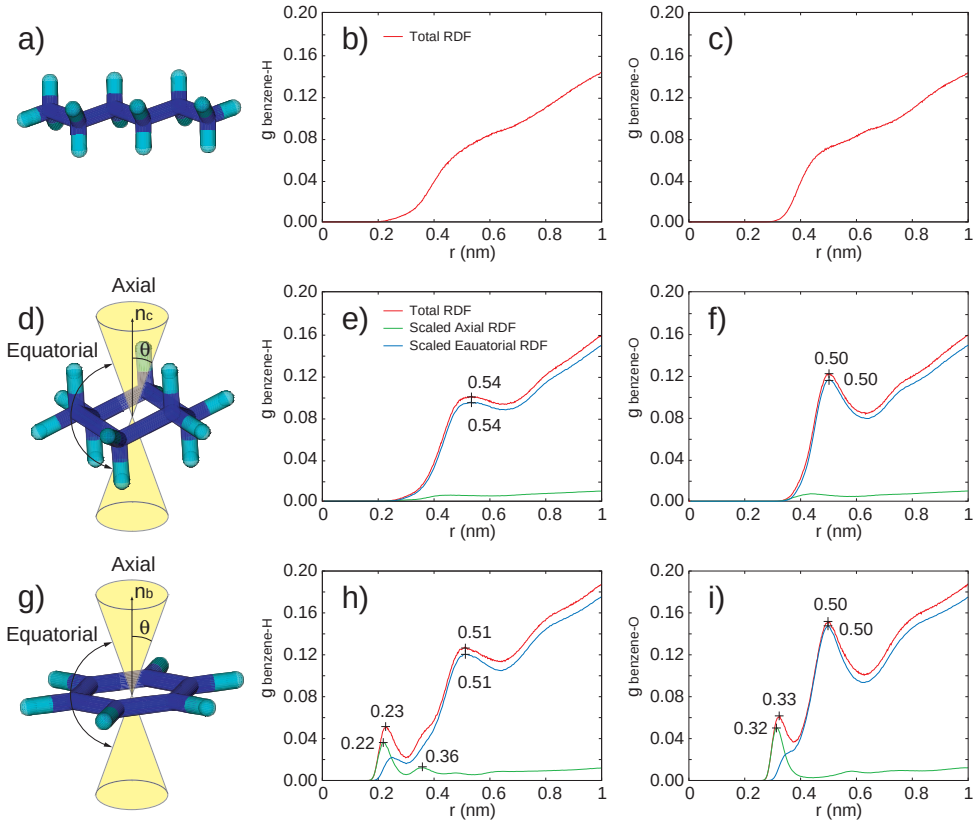

Figure 3.9: Total (red), axial (green), and equatorial (blue) radial distribution functions between the center of hexane (b and c), cyclohexane (e and f), benzene (h and i), and hydrogen (middle panels) or oxygen (right panels) in water molecules in each hydrocarbon–water interfacial system.

toward the center of benzene. This situation provides a strong basis for the dividing angle (20 °) used for Fig.3.9. In other words, the benzene molecules near the interface display " weak hydrogen bonding " between the aromatic rings and the proton of the water molecules in the interface system. Although we have shown here only the analysis of the pure benzene-water interface, a similar finding holds for the toluene-water interface. The attractive nature of this weak hydrogen bonding is the reason aromatics have a lower interfacial tension with water than the other hydrocarbons.

3.3.5 Charge dependence of benzene model: A further evidence of weak hydrogen bonding.

To further confirm the presence of weak hydrogen bonding, the charge dependence in a benzene molecule was investigated. Although the default charge value for hydrogen atoms in a benzene molecule in the CHARMM27 force field is 0.115, values of 0.120, 0.125, and 0.130 were also investigated (the values for carbon atoms were the negative of each hydrogen charge value, Fig.3.11) at 298 K and 0.1 MPa.

Fig.3.12 show the interfacial tensions and the bulk densities at different charge set. The interfacial tensions showed lower values when the model had a higher charge set. Interestingly, the model with a proper charge of -0.130, which provides the experimental interfacial tension, reproduced the density of the pure benzene phase. Therefore, a charge set of 0.130 was used for the benzene model in the light-oil model as well as the pure benzene-water interface, as shown in all figures in this research. Aromatic molecules interact with each other through so-called π-π stacking in which the π systems form two parallel rings overlapping in a face-to-face orientation (Baker and Grant, 2007; Bonnaud et al., 2007; Chelli et al., 2000; Fioroni and Vogt, 2004; Raiteri et al., 2005). They also interact in an edge-to-face orientation where the slight positive charges of substitutes on the ring atoms of one molecule are attracted to the slight negative charge of the aromatic system on another molecule. The configuration with a higher edge-to-face orientation is typically higher (as manifested by high-pressure polymorphs of benzene (Raiteri et al., 2005)) and can explain the observed behavior that the bulk densities show higher values with higher absolute value of electric charges. Although Lorentz-Berthelot rules were used throughout our study, we also tested different Lennard-Jones potential parameters, as van Buuren et al. had done for the decane–water interface (van Buuren et al., 1993). It is concluded that the interfacial tension is mainly dominated by a Coulomb interaction via weak hydrogen bonding, which differs

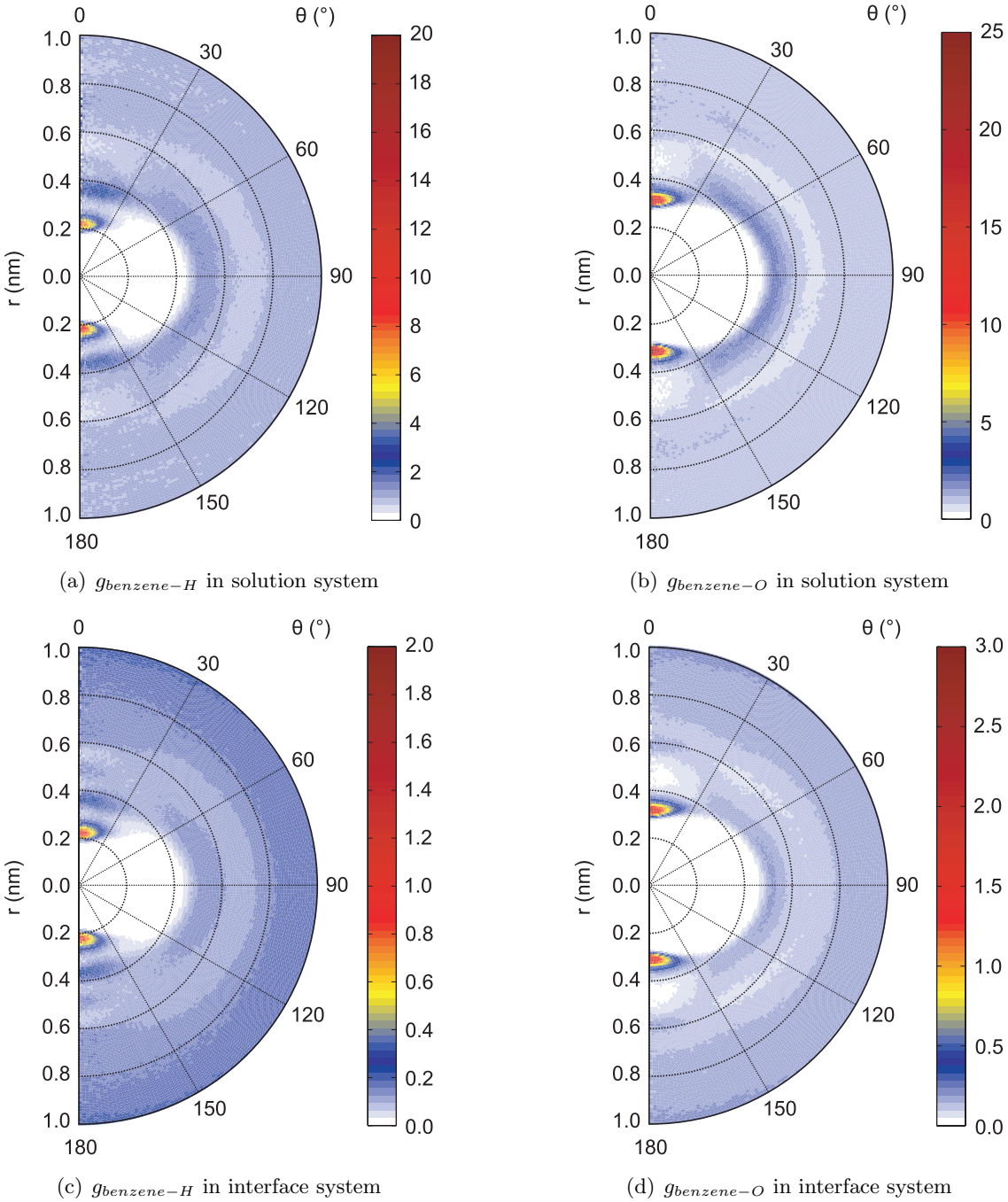

(a) $g_{benzene-H}$ in solution system

(b) $g_{benzene-O}$ in solution system

(c) $g_{benzene-H}$ in interface system

(d) $g_{benzene-O}$ in interface system

Figure 3.10: Angle dependent RDFs from the center of benzene and the hydrogen or oxygen atoms in water molecules. The base direction was set normal to the benzene ring plane

from previous findings based on the analysis of the hydration Gibbs free energy (Graziano and Lee, 2001).

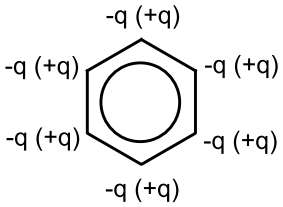

Figure 3.11: Structure of a benzene molecule.

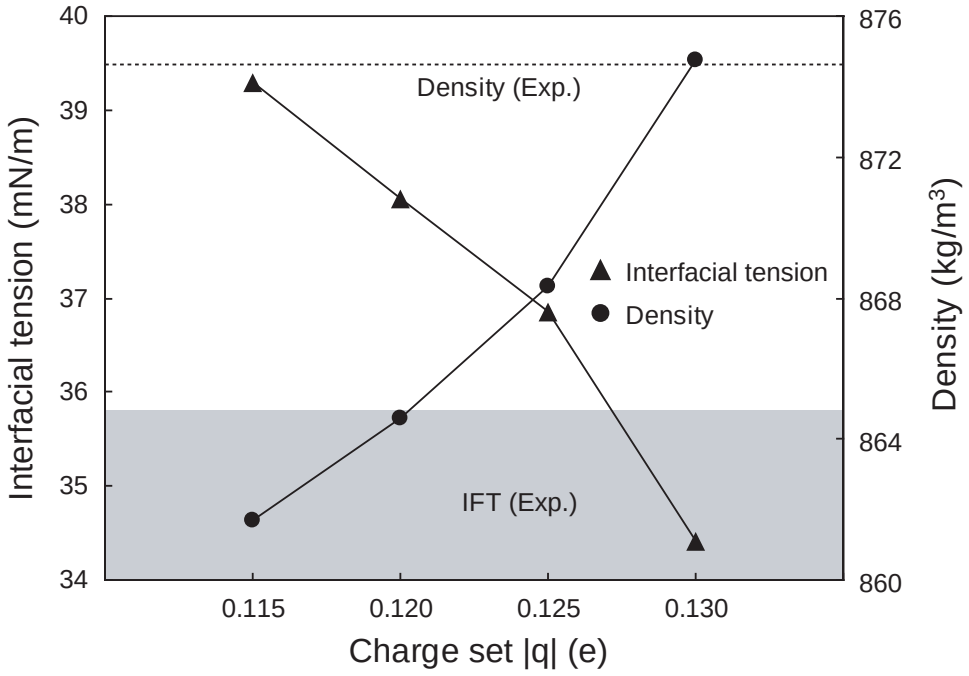

Figure 3.12: Charge dependences of densities of benzene and interfacial tensions of benzene–water.

3.4 Conclusions

Finally, it is remarkable that the accumulation of aromatics is fundamentally different from the layering of alkanols at the oil–water interface and those observed in case of surfactants

(Jang et al., 2004; Takiue et al., 1998), which are well-known amphiphilic behaviors. Such accumulation (or the weak hydrogen bonding) might be detected by vibrational sum frequency spectroscopy (Du et al., 1994; Scatena et al., 2001), novel near-field or fourth-order coherent Raman spectroscopy (De Serio et al., 2006; Nomoto and Onishi, 2007), or spatially resolved NMR spectroscopy (Lambert et al., 2009). In particular, the NMR signals of protons in the plane of an aromatic ring are shifted substantially from those on nonaromatic hydrocarbons. This is an important method to detect the accumulation of aromatics at the oil–water interface. Although the amount of the aromatics accumulation decreases under high-temperature and high-pressure conditions, the phenomenon would generally occur under reservoir conditions. These aromatics-rich layer formations may be a critical factor in determining the interfacial behaviors in EOR technology. It might be straightforward to generalize our findings to the notion that interfacial tension difference is a driving force for the probable accumulation of materials at other mixture interfaces, which are ubiquitous and important to many natural and technological processes.

Chapter 4

Molecular Dynamics of Decane–Water–Vapor Three Phase System

4.1 Introduction

Since wetting and spreading phenomena are ubiquitous in natural and technological processes, and concern areas where chemistry, physics, and engineering intersect, a lot of experimental, theoretical and computational researches have been done. (Bertrand et al., 2009; Blake, 2006; Bonn et al., 2009; Bonn and Ross, 2001; Cruz-Chu et al., 2006; De Coninck and Blake, 2008; De Ruijter et al., 1999; Degennes, 1985; Diaz et al., 2010; Dickson et al., 2006; Dussan, 1979; Harkins and Feldman, 1922; Hong et al., 2009; Huh and Scriven, 1971; Qian et al., 2004, 2006; Rusanov, 2005; Seveno et al., 2009; Shaw and Shaw, 1980). Wettability of oil–water–rock is a key factor in the flow of fluids through the pore spaces in a reservoir, and hence, plays a primary role in oil recovery (Amott, 1959; Cheng et al., 1990; Dixit et al., 2000; Donaldson and Alam, 2008; Hirasaki, 1992; Jadhunandan and Morrow, 1995; Lake, 1989; Morrow, 1990). Moreover, laboratory studies have shown that the wetting behavior of oil on water in the presence of gas, also strongly impacts oil recovery by gas injection (Kalaydjian et al., 1993; Kantzas et al., 1988; Maeda and Okatsu, 2008; Vizika et al., 1998). According to Maeda and Okatsu (2008), the recovery of residual oil by gas flooding was highly influenced by the spreading coefficient of the system. The system with highly positive spreading coefficient gives high recovery ratio of residual oil, because the residual oil can flow as a thin film on water surface (Fig.4.1). On the

other hand, the efficiency of the gas flooding decreases significantly in the system with negative spreading coefficient. Ellipsometric studies of the wetting behavior and its transition have been reported for alkanes on water and on aqueous solutions (Bertrand et al., 2001, 2000; Dussaud and VignesAdler, 1997; Pfohl and Riegler, 1999; Rafaï et al., 2004; Ragil et al., 1996; Ross et al., 2001; Shahidzadeh et al., 1998). The state of spreading of a liquid on another liquid can be estimated from the Neumann triangle of forces for the three tensions to obtain the spreading coefficient, S (Harkins and Feldman, 1922; Shaw and Shaw, 1980). In the case of spreading of oil on water, the three tensions are the surface tensions (SFTs) of water and oil against a gas phase and the interfacial tension (IFT) of oil against water. The spreading coefficients, S, for oil-on-water can be calculated from (Harkins and Feldman, 1922; Shaw and Shaw, 1980):

$$S = \gamma_{wv} - (\gamma_{ov} + \gamma_{wo}) \tag{4.1}$$

where $\gamma_{\alpha\beta}$ is the surface or interfacial tensions between phases α and β, the subscript w, o and v correspond water, oil and vapor, respectively. Since the spreading coefficient describes the force balance at a three phase contact line, if the spreading coefficient is positive, oil will spread on water. On the other hand, oil with a negative spreading coefficient cannot spread and forms a liquid lens (Fig.4.2). Change from non-spreading to spreading occurs at the boundary according to whether the coefficient is positive or negative (Bertrand et al., 2001; Bonn et al., 2009; Bonn and Ross, 2001). Wetting phenomena are governed by interfacial interactions as well as the interactions at the contact line of the three phases, acting usually over a few molecular distances.

In this chapter, the pure decane–water–vapor three phase system was investigated by using MD methods. Decane is a material which has a negative spreading coefficient with water and vapor, so it should form a lens-shape on water surface. The inhomogeneity of molecular distributions at the vicinity of three phase contact line was discussed. Moreover, the line tension value was obtained from local pressure tensor distribution by a convenient way, which was proposed here, and discussed. Note that the system was expanded to more complex one and the effects due to the impurity of oil droplet were discussed in Chapter 5.

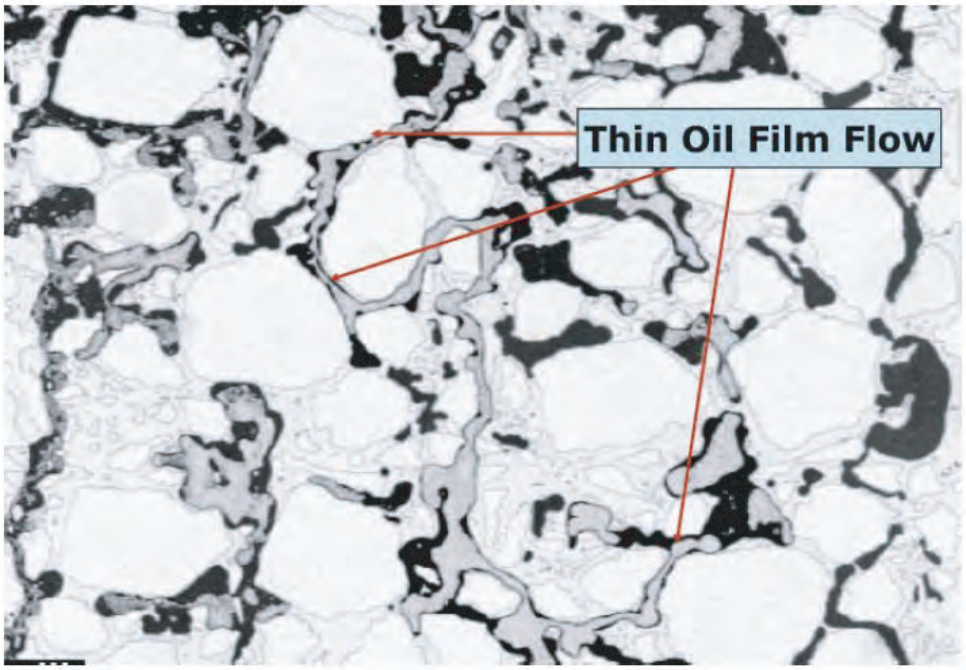

Figure 4.1: Thin oil film flow between gas and water with high spreading coefficient.(Maeda and Okatsu, 2008). Black:Oil, Clean white:Grain, Dark white:Water, Gray:Nitrogen gas.

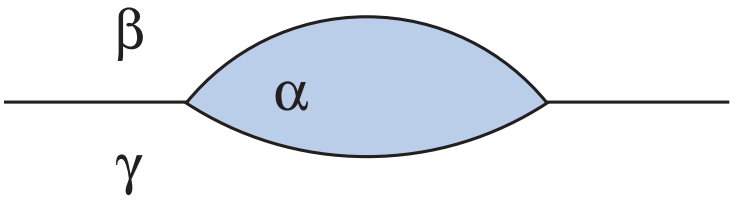

Figure 4.2: Coexistence of three fluid phases.

4.2 Theoretical Backgrounds

4.2.1 Coexistence of three fluid phases

The system which has a negative spreading coefficient includes a lens-shape droplet (Fig.4.2). The Neumann triangle relation is employed here to determine the shape of the three-phase contact zone. From a thermodynamic point of view, the Neumann triangle relation in a mechanical equilibrium condition for a three phase contact line which is formed by three intersecting interfaces of a multi-surface thermodynamic system. For a three phase system including line tension in 3-dimension, a general form of Neumann triangle relation is given by:

$$\boldsymbol{\gamma_{\alpha\beta}} + \boldsymbol{\gamma_{\beta\gamma}} + \boldsymbol{\gamma_{\gamma\alpha}} + \tau\boldsymbol{\kappa} = 0 \tag{4.2}$$

where τ is the line tension, $\boldsymbol{\kappa}$ is the curvature vector of the three phase contact line, $\boldsymbol{\gamma_{ij}}$ indicates the interfacial tension vector between i and j phases. The value of $\boldsymbol{\gamma_{ij}}$ is the interfacial tension between i and j two bulk phases and the direction of $\boldsymbol{\gamma_{ij}}$ is along the tangent of the interface. Since the three phase contact line is assumed as a straight line in our research (discussed in following section), $\boldsymbol{\kappa}$ should be equal to zero. Therefore, Eq.(4.2) can be simplified as:

$$\boldsymbol{\gamma_{\alpha\beta}} + \boldsymbol{\gamma_{\beta\gamma}} + \boldsymbol{\gamma_{\gamma\alpha}} = 0 \tag{4.3}$$

This is a classical expression of Neumann triangle. From Eq.(4.3), the interfacial tension vectors form a closed triangle. Fig.4.3 illustrates such a triangle of interfacial tensions which results in mechanical equilibrium at the three phase contact line, where θ_α, θ_β and θ_γ indicate the angles formed between two adjacent interfacial tension vectors, respectively. This expression can be deduced straightforwardly by minimizing the Helmholtz free energy under the condition of constant volume. For small drops the line tension term becomes important and it cannot be neglected. Thus, for instance, it plays an important role in foam films and it is essential for classical theory of heterogeneous nucleation. However, nothing is known about line tension except for some estimations of the order of its magnitude.

4.2.2 Equations of line tension

Thermodynamically speaking, τdl is the reversible work necessary to extend isothermally the contact line by dl, keeping constant the volumes of the bulk phases and the areas of the dividing

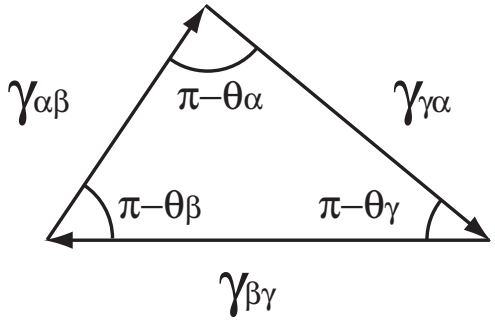

Figure 4.3: Neumann triangle.

surfaces (Drelich, 1996; Qu and Li, 1999; Rusanov, 2005; Tarazona and Navascues, 1981; Toshev et al., 1988).

$$\tau = \left(\frac{\partial F}{\partial L}\right)_{T,V,A_{ij},N} \tag{4.4}$$

where A_{ij} are the respective interfacial areas and N is the number of fluid molecules.

In 2-dimensional system, there are some theoretical approaches to calculate the line tension (Amirfazli and Neumann, 2004; Indekeu, 1994; Kerins and Boiteux, 1983; Rusanov, 2005; Solomentsev and White, 1999; Tarazona and Navascues, 1981; Widom and Widom, 1991). Widom and Widom (1991) has used the density of excess free energy, Ψ, associated with the inhomogeneities in the system; i.e., with the three two-phase interfaces and with the three phase contact line. Near the planar interfaces and far from the three phase contact line, Ψ varies only perpendicularly to the interfaces and vanishes rapidly with increasing distance from them. If $z_{\alpha\beta}$ is a coordinate perpendicular to the $\alpha\beta$ interface, infinitely far from the three phase contact line, the interfacial tension $\gamma_{\alpha\beta}$ of that interface is given by:

$$\gamma_{\alpha\beta} = \int_{-\infty}^{\infty} \Psi dz_{\alpha\beta} \tag{4.5}$$

And similarly for the other interfacial tensions, $\gamma_{\beta\gamma}$ and $\gamma_{\gamma\alpha}$. Near the three phase contact line, the free energy density Ψ varies in the two directions perpendicular to that line. Integrating Ψ through the interior, B, of a circle of radius r centered at the three phase contact line, we obtain the line tension τ as the nest-to-leading term in the asymptotic expansion ($R \to \infty$):

$$\int_B \Psi db = r\left(\gamma_{\alpha\beta} + \gamma_{\beta\gamma} + \gamma_{\gamma\alpha}\right) + \tau + O\left(1/r\right) \tag{4.6}$$

where db is an element of area in the plane. Then Kerins and Boiteux (1983) have supposed that Ψ is of the form:

$$\Psi = F(\rho_1, \rho_2, \dots) + \frac{1}{2}\sum_{i,j} m_{ij} \nabla \boldsymbol{\rho_i} \cdot \nabla \boldsymbol{\rho_j} \tag{4.7}$$

where the ρ_i are the density or composition variables in the system, the function $F(\rho_1, \rho_2, \dots)$ vanishes when the ρ_i have their bulk phase values and is positive for all other values of the ρ_i, the m_{ij} are constant parameters, and ∇ is the two dimensional gradient operator in any plane perpendicular to the three phase contact line. Then the equilibrium $\boldsymbol{\rho_i}$ satisfy the Euler-Lagrange equations:

$$\frac{\partial F}{\partial \rho_i} = \frac{1}{2}\sum_{j} (m_i + m_j) \nabla^2 \rho_j \tag{4.8}$$

And then Kerins and Boiteux (1983) have derived a formula for the line tension given by:

$$\tau = \int_B (\Psi - 2F)\, db \tag{4.9}$$

Widom and Widom (1991) have proposed a model free-energy functional for F in Eq.(4.9) by modeling ρ_i near the three phase contact line. They have modeled ρ_i with a simple function. Therefore there is no reason that the actual density distribution ρ_i satisfy such a simple function near the three phase contact line.

Tarazona and Navascues (1981) have derived two types of expression of the line tension from Eq.(4.4) as a function of local pressure distributions and interfacial tensions:

$$\tau = \iint_B [p_B - p_{yy}]\, dxdz - r\,(\gamma_{\alpha\beta} + \gamma_{\beta\gamma} + \gamma_{\gamma\alpha}) \tag{4.10}$$

and

$$\tau = \iint_B \left[\frac{p_{xx} + p_{zz}}{2} - p_{yy}\right] dxdz - \frac{r}{2}\,(\gamma_{\alpha\beta} + \gamma_{\beta\gamma} + \gamma_{\gamma\alpha}) \tag{4.11}$$

where B is an infinite large region, which includes the three phase contact line, r is the radius of B, p_B is the bulk pressure and p_{ij} is an element of the pressure tensor $\boldsymbol{p}$. Here the axes are set as the straight three phase contact line locates on y direction. Tarazona and Navascues (1981) have derived Eq.(4.10) and Eq.(4.11) for the analyses of their solid–liquid–liquid three phase system, but they also can be applied to a liquid–liquid–liquid three phase system. Eq.(4.10)

and Eq.(4.11) are equivalent, because in this region B, the following equation is satisfied under hydrostatic conditions:

$$\iint_B (p_B - p_{xx})\, dxdz + \iint_B (p_B - p_{zz})\, dxdz = r\left(\gamma_{\alpha\beta} + \gamma_{\beta\gamma} + \gamma_{\gamma\alpha}\right) \tag{4.12}$$

The proof of Eq.(4.12) is given in the following section. Moreover, using Eq.(4.12), we can get another expression of equation of the line tension from either Eq.(4.10) or Eq.(4.11) as:

$$\tau = \iint_B \left[p_{xx} + p_{zz} - p_{yy} - p_B\right] dxdz \tag{4.13}$$

Eq.(4.13) is convenient expression since Eq.(4.13) do not need to consider the shapes of three interfaces as Kerins and Boiteux (1983) have mentioned for Eq.(4.9), which was also derived with similar procedures for Eq.(4.13).

4.2.3 Relationship between local pressures and interfacial tensions

In this section, at first, the Neumann triangle relation (Eq.(4.3)) is derived from the hydrostatic equilibrium condition. And then, by using similar ways when the Neumann triangle condition is derived, the relationship between the local pressure tensor and the interfacial tensions at the three phase contact zone (Eq.(4.12)) is derived. Similar ways have been used by Tarazona and Navascues (1981) for their solid–liquid–liquid three phase system. Here their techniques are modified for our liquid–liquid–liquid three phase system.

Neumann triangle from hydrostatic equilibrium

Under the hydrostatic equilibrium condition, the pressure tensors satisfies the equations of equilibrium.

$$\begin{aligned}
0 &= \frac{\partial p_{xx}}{\partial x} + \frac{\partial p_{yx}}{\partial y} + \frac{\partial p_{zx}}{\partial z} \\
0 &= \frac{\partial p_{xy}}{\partial x} + \frac{\partial p_{yy}}{\partial y} + \frac{\partial p_{zy}}{\partial z} \\
0 &= \frac{\partial p_{xz}}{\partial x} + \frac{\partial p_{yz}}{\partial y} + \frac{\partial p_{zz}}{\partial z}
\end{aligned} \tag{4.14}$$

Since our system is 2-dimension, Eq.(4.14) reduce to

$$0 = \frac{\partial p_{xx}}{\partial x} + \frac{\partial p_{zx}}{\partial z} \tag{4.15}$$

$$0 = \frac{\partial p_{xz}}{\partial x} + \frac{\partial p_{zz}}{\partial z} \tag{4.16}$$

Accordingly, the integrals of Eq.(4.15) and Eq.(4.16) over any simply-connected region B are 0.

$$0 = \iint_B \left[\frac{\partial p_{xx}}{\partial x} + \frac{\partial p_{zx}}{\partial z} \right] dxdz \tag{4.17}$$

$$0 = \iint_B \left[\frac{\partial p_{xz}}{\partial x} + \frac{\partial p_{zz}}{\partial z} \right] dxdz \tag{4.18}$$

By Stokes' theorem, these integrals over the region B can be converted to line integrals along the boundary ∂B of B.

$$0 = \oint_{\partial B} [p_{xx}dz - p_{zx}dx] \tag{4.19}$$

$$0 = \oint_{\partial B} [p_{xz}dz - p_{zz}dx] \tag{4.20}$$

Here we calculate these integrals in the circle region B (Fig.4.4). In polar coordinates,

$$x = r\cos\theta \tag{4.21}$$

$$z = r\sin\theta \tag{4.22}$$

$$dx = -r\sin\theta d\theta \tag{4.23}$$

$$dz = r\cos\theta d\theta \tag{4.24}$$

Therefore, Eq.(4.19) and Eq.(4.20) become

$$0 = r\int_{-\pi}^{\pi} [p_{xx}\cos\theta + p_{zx}\sin\theta]\, d\theta \tag{4.25}$$

$$0 = r\int_{-\pi}^{\pi} [p_{xz}\cos\theta + p_{zz}\sin\theta]\, d\theta \tag{4.26}$$

Then we used the rotation matrix $\boldsymbol{A}$ to rotate the coordinate.

$$\boldsymbol{p'} = \boldsymbol{ApA^{-1}}$$
$$\text{where } \boldsymbol{A} = \begin{pmatrix} \cos\theta & \sin\theta \\ -\sin\theta & \cos\theta \end{pmatrix} \tag{4.27}$$

By Eq.(4.27), Eq.(4.25) and Eq.(4.26) become

$$0 = r\int_{-\pi}^{\pi} [p_{x'x'}\cos\theta - p_{z'x'}\sin\theta]\, d\theta \tag{4.28}$$

$$0 = r\int_{-\pi}^{\pi} [p_{x'x'}\sin\theta + p_{x'z'}\cos\theta]\, d\theta \tag{4.29}$$

$\boldsymbol{p}$ and $\boldsymbol{p'}$ are the pressure tensors referred to xz and $x'z'$ systems, respectively, and $\boldsymbol{A}$ is the matrix corresponding to a rotation about the y axis through angle θ. Because of the symmetry

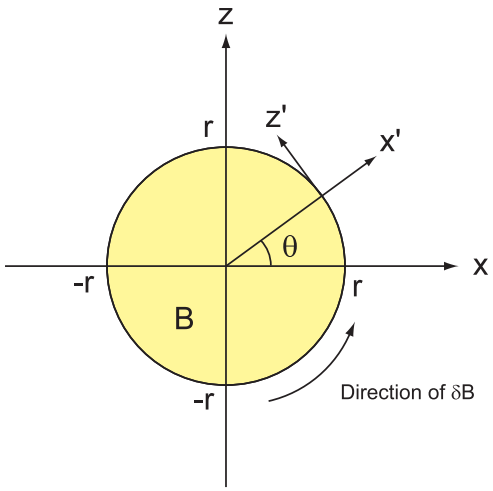

Figure 4.4: Diagram showing the circle region over which the integral Eq.(4.19) and Eq.(4.20) are carried out.

and the fluid character of our system, it is clear that $p'_{xz} \equiv 0$ and $p'_{zx} \equiv 0$ far from the three phase contact line, so Eq.(4.28) and Eq.(4.29) become

$$0 = r \int_{-\pi}^{\pi} p_{x'x'} \cos\theta d\theta \tag{4.30}$$

$$0 = r \int_{-\pi}^{\pi} p_{x'x'} \sin\theta d\theta \tag{4.31}$$

Eq.(4.30) can be written as:

$$\begin{aligned} 0 &= r \int_{-\pi}^{\pi} \left[p_B - p_{x'x'} \cos\theta\right] d\theta - r \int_{-\pi}^{\pi} p_B d\theta \\ &= r \int_{-\pi}^{\pi} \left[p_B - p_{x'x'} \cos\theta\right] d\theta \\ &= \gamma_{\alpha\beta} e_{\alpha\beta,x} + \gamma_{\beta\gamma} e_{\beta\gamma,x} + \gamma_{\gamma\alpha} e_{\gamma\alpha,x} \end{aligned} \tag{4.32}$$

and also Eq.(4.31) can be written as:

$$\begin{aligned} 0 &= r \int_{-\pi}^{\pi} \left[p_B - p_{x'x'} \sin\theta\right] d\theta - r \int_{-\pi}^{\pi} p_B d\theta \\ &= r \int_{-\pi}^{\pi} \left[p_B - p_{x'x'} \sin\theta\right] d\theta \\ &= \gamma_{\alpha\beta} e_{\alpha\beta,z} + \gamma_{\beta\gamma} e_{\beta\gamma,z} + \gamma_{\gamma\alpha} e_{\gamma\alpha,z} \end{aligned} \tag{4.33}$$

where $e_{ij,k}$ is an element of unit vector tangent to the interface between phase i and j on k axis. Eq.(4.32) and Eq.(4.33) indicate the Neumann triangle relation (Eq.(4.3)) as the balance of forces at the three phase contact line.

Relationship between local pressures 1.

Here we integrated over half-circle region C (Fig.4.5) for Eq.(4.19).

$$0 = \int_{\partial C_1} [p_{xx}dz - p_{zx}dx] + \int_{\partial C_2} p_{xx}dz \tag{4.34}$$

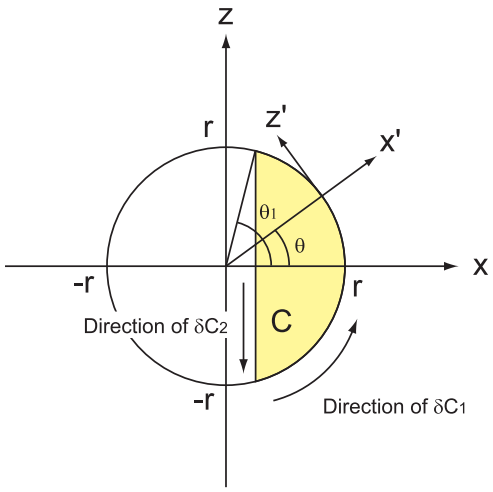

Figure 4.5: Diagram showing the circle region over which the integral Eq.(4.34) is carried out.

With Eq.(4.27) in polar coordinates, Eq.(4.34) becomes

$$0 = r\int_{-\theta_1}^{\theta_1} [p_{x'x'}\cos\theta - p_{z'x'}\sin\theta]\, d\theta - \int_{-\sin\theta_1}^{\sin\theta_1} p_{xx}dz \tag{4.35}$$

At far from the three phase contact line, Eq.(4.35) becomes

$$0 = r\int_{-\theta_1}^{\theta_1} p_{x'x'}\cos\theta d\theta - \int_{-\sin\theta_1}^{\sin\theta_1} p_{xx}dz \tag{4.36}$$

And then, Eq.(4.36) is integrated over $-r$ to r in x direction:

$$\begin{aligned} 0 &= \int_{-r}^{r}\left[r\int_{-\theta_1}^{\theta_1} p_{x'x'}\cos\theta d\theta - \int_{-\sin\theta_1}^{\sin\theta_1} p_{xx}dz\right] dx \\ &= r^2\int_0^{\pi}\left[\sin\theta_1\int_{-\theta_1}^{\theta_1} p_{x'x'}\cos\theta d\theta\right] d\theta_1 - \iint_B p_{xx}dxdz \end{aligned} \tag{4.37}$$

Here the first term of Eq.(4.37) is written as I_1, and can be expanded as:

$$\begin{aligned} \frac{I_1}{r^2} &= \left[-\cos\theta_1\int_{-\theta_1}^{\theta_1} p_{x'x'}\cos\theta d\theta\right]_0^{\pi} + \int_0^{\pi}\cos\theta_1\frac{d}{d\theta_1}\left(\int_{-\theta_1}^{\theta_1} p_{x'x'}\cos\theta d\theta\right) d\theta_1 \\ &= \int_{-\pi}^{\pi} p_{x'x'}\cos\theta d\theta + \int_0^{\pi}\cos\theta_1\frac{d}{d\theta_1}\left(\int_{-\theta_1}^{\theta_1} p_{x'x'}\cos\theta d\theta\right) d\theta_1 \end{aligned} \tag{4.38}$$

From Eq.(4.30), the first term of Eq.(4.38) is zero, and then Eq.(4.38) becomes

$$\begin{aligned}\frac{I_1}{r^2} &= \int_0^{\pi} \cos\theta_1 \left[p_{x'x'}\left(r,\theta_1\right)\cos\theta_1 \frac{d\theta_1}{d\theta_1} - p_{x'x'}\left(r,-\theta_1\right)\cos\left(-\theta_1\right)\frac{d\left(-\theta_1\right)}{d\theta_1}\right] d\theta_1 \\ &= \int_0^{\pi} \cos\theta_1 \left[p_{x'x'}\left(r,\theta_1\right)\cos\theta_1 + p_{x'x'}\left(r,-\theta_1\right)\cos\left(-\theta_1\right)\right] d\theta_1 \\ &= \int_0^{\pi} p_{x'x'}\left(r,\theta_1\right)\cos^2\theta_1 d\theta_1 + \int_{-\pi}^{0} p_{x'x'}\left(r,\theta_1\right)\cos^2\theta_1 d\theta_1 \\ &= \int_{-\pi}^{\pi} p_{x'x'}\cos^2\theta_1 d\theta_1 \end{aligned} \tag{4.39}$$

Finally, from Eq.(4.37) and Eq.(4.39), one finds

$$0 = r^2 \int_{-\pi}^{\pi} p_{x'x'}\cos^2\theta d\theta - \iint_B p_{xx} dx dz \tag{4.40}$$

Relationship between local pressures 2.

Here we integrated over half-circle region D (Fig.4.6) for Eq.(4.20).

$$0 = \int_{\partial D_1} \left[p_{xz} dz - p_{zz} dx\right] + \int_{\partial D_2} p_{zz} dx \tag{4.41}$$

With Eq.(4.27) in polar coordinates, Eq.(4.41) becomes

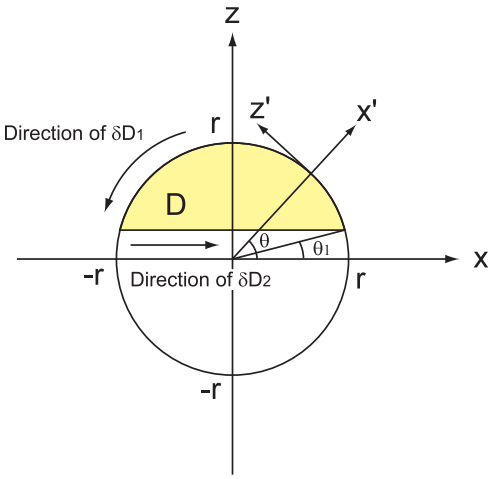

Figure 4.6: Diagram showing the circle region over which the integral Eq.(4.41) is carried out.

$$0 = r \int_{\theta_1}^{\pi-\theta_1} \left[p_{x'x'}\sin\theta + p_{z'x'}\cos\theta\right] d\theta + \int_{\cos(\pi-\theta_1)}^{\cos(\theta_1)} p_{zz} dx \tag{4.42}$$

At far from the three phase contact line, Eq.(4.42) becomes

$$0 = r\int_{\theta_1}^{\pi-\theta_1} p_{x'x'}\sin\theta d\theta + \int_{\cos(\pi-\theta_1)}^{\cos\theta_1} p_{zz}dx \tag{4.43}$$

And then, Eq.(4.43) is integrated over $-r$ to r in z direction.

$$\begin{aligned} 0 &= \int_{-r}^{r}\left[r\int_{\theta_1}^{\pi-\theta_1} p_{x'x'}\sin\theta d\theta + \int_{\cos(\pi-\theta_1)}^{\cos\theta_1} p_{zz}dx\right]dz \\ &= r^2\int_{-\frac{\pi}{2}}^{\frac{\pi}{2}}\left[\cos\theta_1\int_{\theta_1}^{\pi-\theta_1} p_{x'x'}\sin\theta d\theta\right]d\theta_1 + \iint_B p_{zz}dxdz \end{aligned} \tag{4.44}$$

Here the first term of Eq.(4.44) is written as I_2, and can be expanded as:

$$\begin{aligned} \frac{I_2}{r^2} &= \left[\sin\theta_1\int_{\theta_1}^{\pi-\theta_1} p_{x'x'}\sin\theta d\theta\right]_{-\frac{\pi}{2}}^{\frac{\pi}{2}} - \int_{-\frac{\pi}{2}}^{\frac{\pi}{2}}\sin\theta_1\frac{d}{d\theta_1}\left(\int_{\theta_1}^{\pi-\theta_1} p_{x'x'}\sin\theta d\theta\right)d\theta_1 \\ &= -\int_{-\frac{\pi}{2}}^{\frac{3\pi}{2}} p_{x'x'}\cos\theta d\theta - \int_{-\frac{\pi}{2}}^{\frac{\pi}{2}}\sin\theta_1\frac{d}{d\theta_1}\left(\int_{\theta_1}^{\pi-\theta_1} p_{x'x'}\sin\theta d\theta\right)d\theta_1 \end{aligned} \tag{4.45}$$

From Eq.(4.31), the first term of Eq.(4.45) is zero, and then Eq.(4.45) becomes

$$\begin{aligned} \frac{I_2}{r^2} &= -\int_{-\frac{\pi}{2}}^{\frac{\pi}{2}}\sin\theta_1\left[p_{x'x'}\left(r,\pi-\theta_1\right)\sin\left(\pi-\theta_1\right)\frac{d\left(\pi-\theta_1\right)}{d\theta_1} - p_{x'x'}\left(r,\theta_1\right)\sin\left(\theta_1\right)\frac{d\theta_1}{d\theta_1}\right]d\theta_1 \\ &= -\int_{-\frac{\pi}{2}}^{\frac{\pi}{2}}\sin\theta_1\left[-p_{x'x'}\left(r,\pi-\theta_1\right)\sin\left(\pi-\theta_1\right) - p_{x'x'}\left(r,\theta_1\right)\sin\left(\theta_1\right)\right]d\theta_1 \\ &= \int_{\frac{\pi}{2}}^{\frac{3\pi}{2}} p_{x'x'}\left(r,\theta_1\right)\sin^2\theta_1 d\theta_1 + \int_{-\frac{\pi}{2}}^{\frac{\pi}{2}} p_{x'x'}\left(r,\theta_1\right)\sin^2\theta_1 d\theta_1 \\ &= \int_{-\pi}^{\pi} p_{x'x'}\sin^2\theta_1 d\theta_1 \end{aligned} \tag{4.46}$$

Finally, from Eq.(4.44) and Eq.(4.46), one finds

$$0 = r^2\int_{-\pi}^{\pi} p_{x'x'}\sin^2\theta d\theta - \iint_B p_{xx}dxdz \tag{4.47}$$

Relationship between local pressures and interfacial tensions

From Eq.(4.40) and Eq.(4.47), one fines,

$$\begin{aligned} \iint_B p_{xx}dxdz + \iint_B p_{zz}dxdz &= r^2\int_{-\pi}^{\pi} p_{x'x'}d\theta \\ &= r\oint_{\partial B} p_{x'x'}dl \end{aligned} \tag{4.48}$$

The left side of Eq.(4.48) can be written as:

$$\begin{aligned}\iint_B p_{xx}dxdz + \iint_B p_{zz}dxdz &= \iint_B (p_B - p_{xx})\,dxdz + \iint_B (p_B - p_{zz})\,dxdz - 2\int_B p_B dxdz \\ &= \iint_B (p_B - p_{xx})\,dxdz + \iint_B (p_B - p_{zz})\,dxdz - 2p_B\pi r^2\end{aligned} \tag{4.49}$$

Also, the right side of Eq.(4.48) can be written as:

$$\begin{aligned}r\oint_{\partial B} p_{x'x'}dl &= r\oint_{\partial B} (p_B - p_{x'x'})\,dl - r\oint_{\partial B} p_B dl \\ &= r\left(\gamma_{\alpha\beta} + \gamma_{\beta\gamma} + \gamma_{\gamma\alpha}\right) - 2p_B\pi r^2\end{aligned} \tag{4.50}$$

From Eq.(4.49) and Eq.(4.50), one finds Eq.(4.12),

$$\iint_B (p_B - p_{xx})\,dxdz + \iint_B (p_B - p_{zz})\,dxdz = r\left(\gamma_{\alpha\beta} + \gamma_{\beta\gamma} + \gamma_{\gamma\alpha}\right) \tag{4.51}$$

4.3 Computational Methods

4.3.1 Materials

The droplet used in this study consisted of decane ($C_{10}H_{22}$) with 1000 molecules. Decane phase has a negative spreading coefficient in decane–water–vapor three phase system in experiments, so it forms a lens-shape droplet on water surface. The chemical formulas and structures of decane and water are shown in Table.4.1. The water molecules were modeled by the SPC/E model (Alejandre et al., 1995; Berendsen et al., 1987). A revised version of the CHARMM 27 force field (Davis et al., 2008; Klauda et al., 2005; MacKerell Jr et al., 1998) was used to model the decane molecules. All parameters for these models are listed in Appendix A.

Table 4.1: Chemical formulas and structures of molecules used in decane–water–vapor three phase system.

Component	Formula	Structure
n-decane	$C_{10}H_{22}$	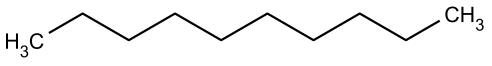
water	H_2O	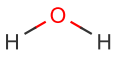

4.3.2 Preparation of 2D decane–water–vapor three phase system

The decane–water–vapor three phase system was made as an apparent 2 dimensional (2D) system (e.g. left top in Fig.4.7). The advantages of such a system comparing to fully 3 dimensional (3D) one (e.g. right top in Fig.4.7) are follows:

1. Computational time can be saved since the small length in the depth direction can be taken.

2. Equations of line tension in a previous section can be used directly, since they have been derived for 2D system.

3. Effect caused by droplet size to contact angle can be ignored, since the curvature radius is infinity on the straight three phase contact line.

Weijs et al. (2011) have performed MD simulations of 2D and 3D droplet systems (Fig.4.7) and investigated the contact angles at different size of droplets (Fig.4.8). As mentioned above, the contact angles in 2D system does not show a size dependence, whereas those in 3D system show it. And note that, more importantly, they have obtained the negative line tension by fitting the contact angles as a function of droplet size.

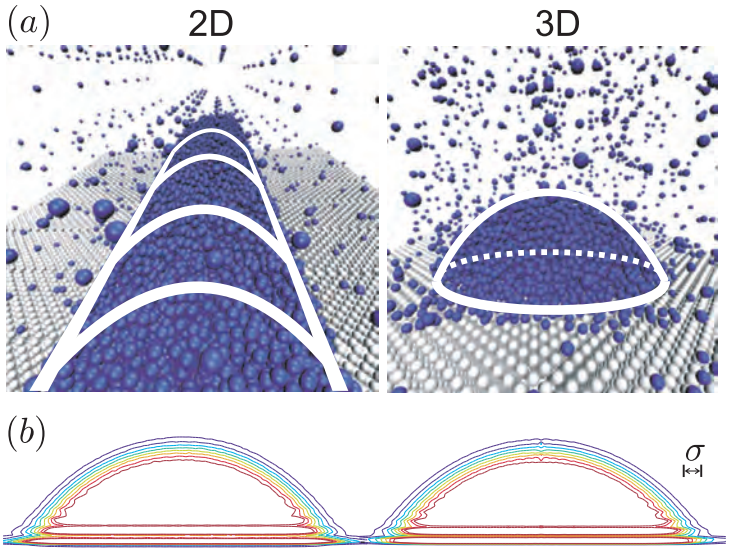

Figure 4.7: Snapshots and isodensity contours from molecular dynamics simulations of a 2D and a 3D (Weijs et al., 2011).

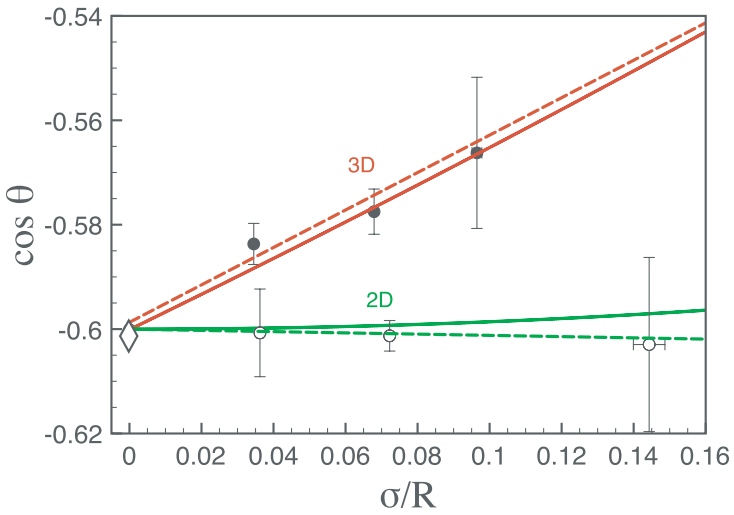

Figure 4.8: $cos\theta$ vs σR^{-1} for cylindrical (open symbols) and spherical (filled symbols) drops for $cos\theta_Y = -0.60$ (Weijs et al., 2011). The dashed lines are linear fits through the data points, and the solid lines are the solutions obtained using density functional theory (DFT). The top two lines represent the 3D data, whereas the bottom two lines represent the 2D data. The diamond at $1/R = 0$ indicates Young's law, calculated independently by determining the surface tensions of the three interfaces.

Fig.4.9 shows how we prepared our oil–water–vapor three phase system. First, the droplet model was calculated from NVT simulation to form a cylindrical shape (Fig.4.9(a)). Then the thin water layer was calculated from NPnAT simulation (Fig.4.9(b)). The cylindrical droplet was put next to the thin water layer to give continuity in the y direction (Fig.4.9(c)), and hence, a 2D profile in the x and z plane. Finally, the oil–water–vapor three phase system was equilibrated with NVT ensemble.

4.3.3 Details of Molecular Dynamics

The MD simulation was performed using the GROMACS package (Hess et al., 2008; Van Der Spoel et al., 2005). In all NVT and NPnAT calculations, the temperature was controlled by the Nose-Hoover thermostat (Nose, 1984) to 298 K. In NPnAT calculations, the pressure was controlled by the Parrinello-Rahman method (Parrinello and Rahman, 1982) to 0.1 MPa. The particle mesh Ewald summation (Essmann et al., 1995) was used for the electrostatic interactions, and a cutoff of 1.4 nm was used for calculation of the van der Waals interactions. A 1.0 fs time step was used and output coordinates were obtained every 1.0 ps. Calculations run for 10.0 ns, and showed sufficiently close approach to equilibrium states. Snapshots of molecular distributions were prepared by Visual Molecular Dynamics (VMD) software (Humphrey et al., 1996). After that, the local pressure distributions were calculated using an adapted version of GROMACS that allows the computation of local pressure distributions (Ollila et al., 2009), by re-calculating the output trajectories with 0.1 grid size.

4.4 Results and Discussion

4.4.1 Shape of decane droplet on water

Snapshots of a unit cell for MD calculations at the beginning and after 5.0 ns of simulation are shown in Fig.4.10 as 2D and 3D images. And the series of 2D images during MD equilibration are shown in Fig.4.11. The unit cell has 20 nm $\times$ 6.88916 nm $\times$ 18 nm in x, y and z direction, respectively. At the beginning, the minimum distance between the decane droplet and water surfaces was set to less than 0.5 nm (Fig.4.10(a)). Once the simulation started, the decane droplet approached the water surface and contact at around 10 ps (Fig.4.11). Note that there are not any external forces, such as gravity, in our all MD calculations. So these approaching and contacting phenomena were caused by attractive interactions, such as van der Waals forces,

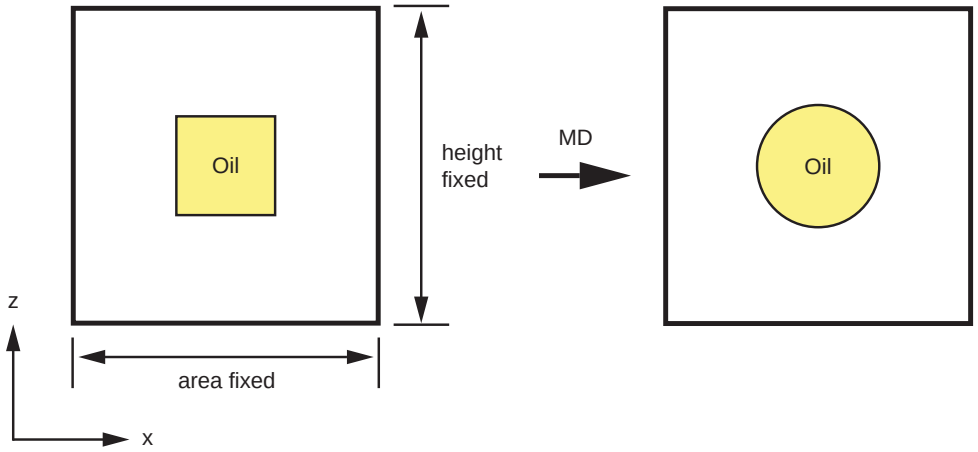

(a) Preparation of cylindrical oil droplet by NVT ensemble.

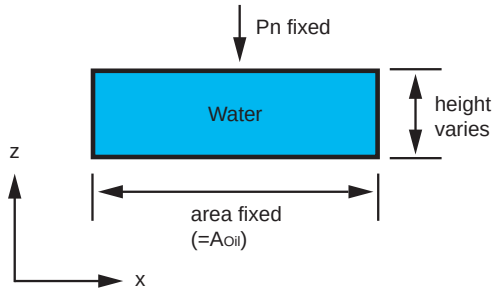

(b) Preparation of water layer by NP_nAT ensemble.

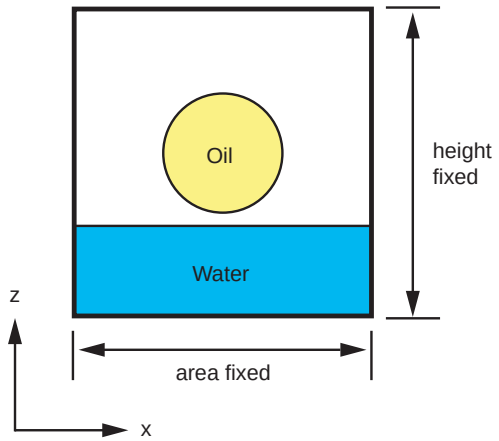

(c) Oil–water–vapor three phase system by NVT ensemble.

Figure 4.9: Schematic flow how to make and simulate an oil–water–vapor three phase system.

between their molecules. Then the decane droplet started to spread on the water surface. Finally, the decane formed a lens-shape droplet on water surface at around 1.0 ns of simulation time. After that, the decane droplet kept its shape apart from the effect of thermal fluctuations (Fig.4.11). During MD simulation, the decane–water–vapor three phase system has been continuous in y direction. Very small amount of decane and water molecule evaporated from their each bulk phase (t =1, 10ns in Fig.4.11). The decane molecules were observed below the water layer (t =2, 6, 10ns in Fig.4.11). This was that the evaporated decane molecules came through periodic boundary condition in z direction and adsorbed onto the water surface during MD simulation.

The density distributions were calculated from the trajectories over 2.0–10.0ns and are shown in the left panels in Fig.4.12. It seems that the edges of the density distributions are unclear, especially in case of decane droplet. As shown in Fig.4.11, the decane droplet has floated on the water surface during MD simulation, similar to a real situation. To confirm how the decane droplet float on water surface, the locations of center of mass (COM) of the decane droplet for each 0.2 ns length from 2.0 ns to 10.0 ns were calculated and are shown in Fig.4.14. From Fig.4.14, the decane droplet has moved randomly, especially in x-direction, from x $\sim$ 8.8 nm to $\sim$ 10.6 nm. This is the reason why these density distributions (left panels in Fig.4.12) got unclear. In order to avoid that effect, the density distributions were obtained by following way:

1. The temporally-segmented density distributions of each component were calculated on 0.1 nm $\times$ 0.1 nm grid size over the trajectory of 0.2 ns length. In this stage, totally 40 density distributions were obtained.

2. Each temporally-segmented density distribution was shifted as the x-position of COM of the decane droplet located at the center of the unit cell (x =10 nm).

3. The shifted temporally-segmented density distributions were averaged over 2.0–10.0ns.

The schematic flow of these procedures are shown in Fig.4.13.

The right panels in Fig.4.12 show those which are based on these shifting procedures. Obviously, the edges of each density distributions in Fig.4.12(b), Fig.4.12(d) and Fig.4.12(f) becomes clearer than original ones (Fig.4.12(a), Fig.4.12(c) and Fig.4.12(e), respectively). Moreover, these density distributions are very symmetrical around x = 10nm. So the density distributions were averaged both sides of the symmetrical line. Fig.4.15, Fig.4.16 and Fig.4.17 show the half

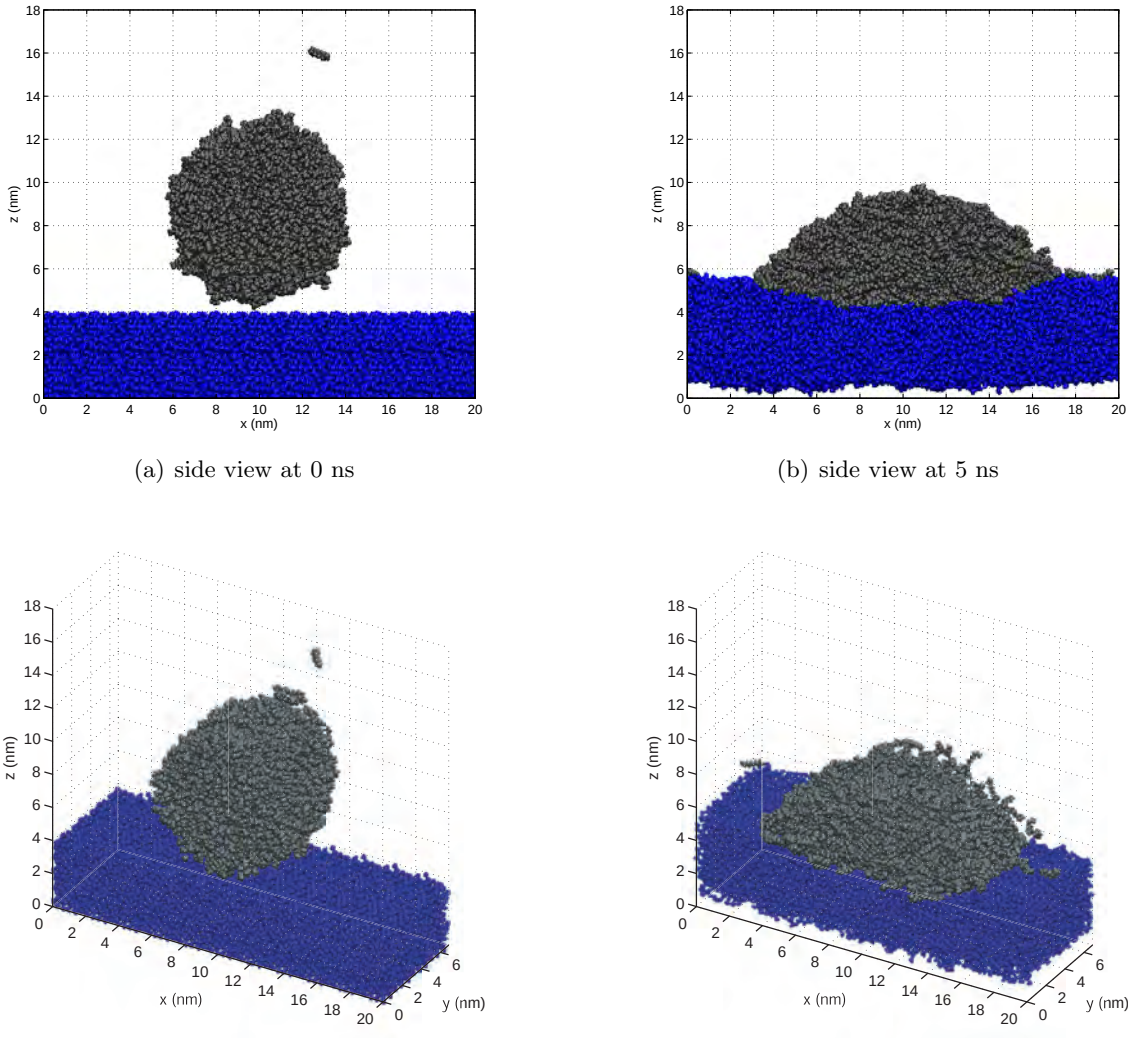

(a) side view at 0 ns

(b) side view at 5 ns

(c) 3D view at 0 ns

(d) 3D view at 5 ns

Figure 4.10: Snapshots of decane–water–vapor three phase system (gray, decane; blue, water).

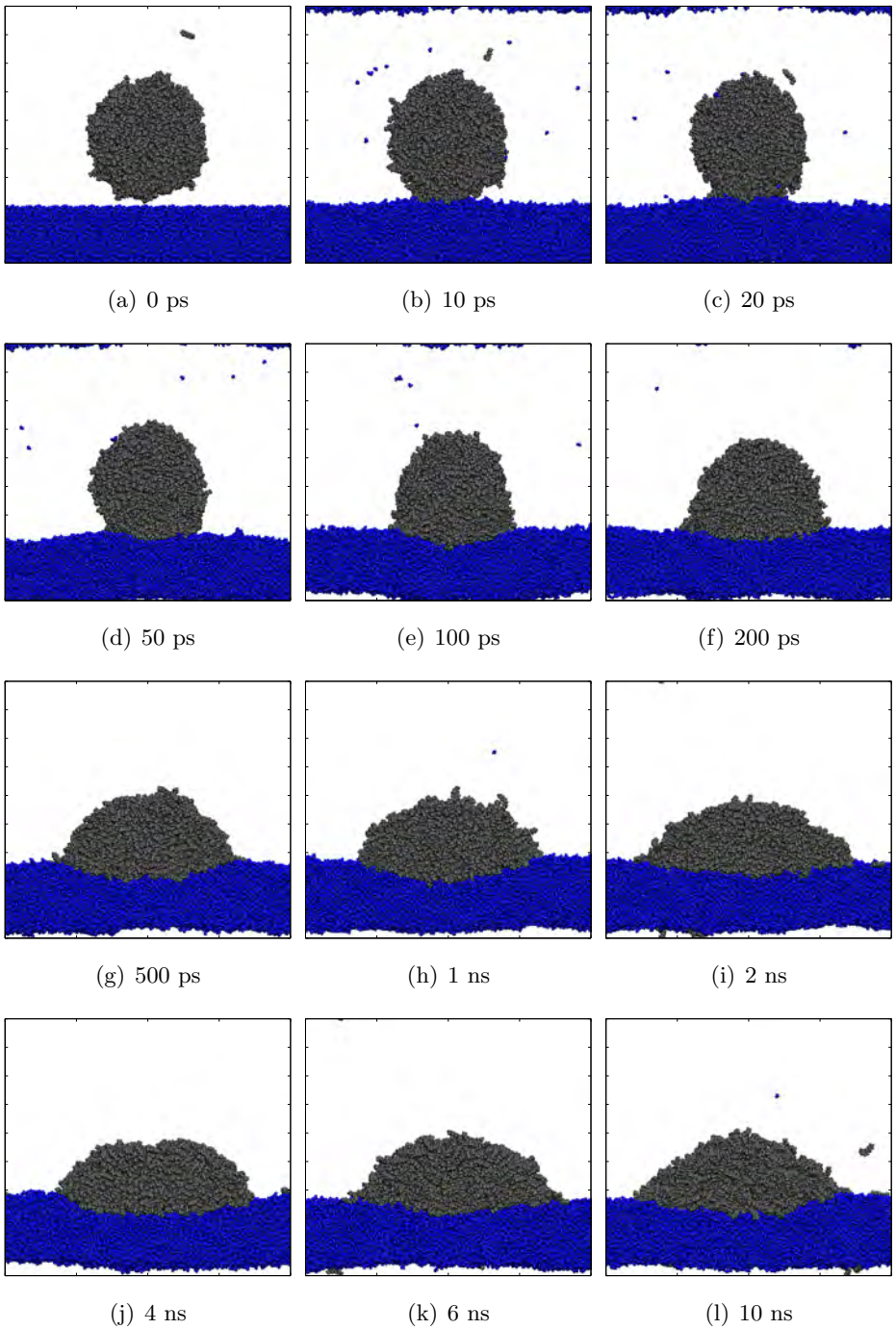

(a) 0 ps (b) 10 ps (c) 20 ps

(d) 50 ps (e) 100 ps (f) 200 ps

(g) 500 ps (h) 1 ns (i) 2 ns

(j) 4 ns (k) 6 ns (l) 10 ns

Figure 4.11: Series of snapshots of decane–water–vapor three phase system (gray, decane; blue, water). The size of each panel corresponds to Fig.4.10(a).

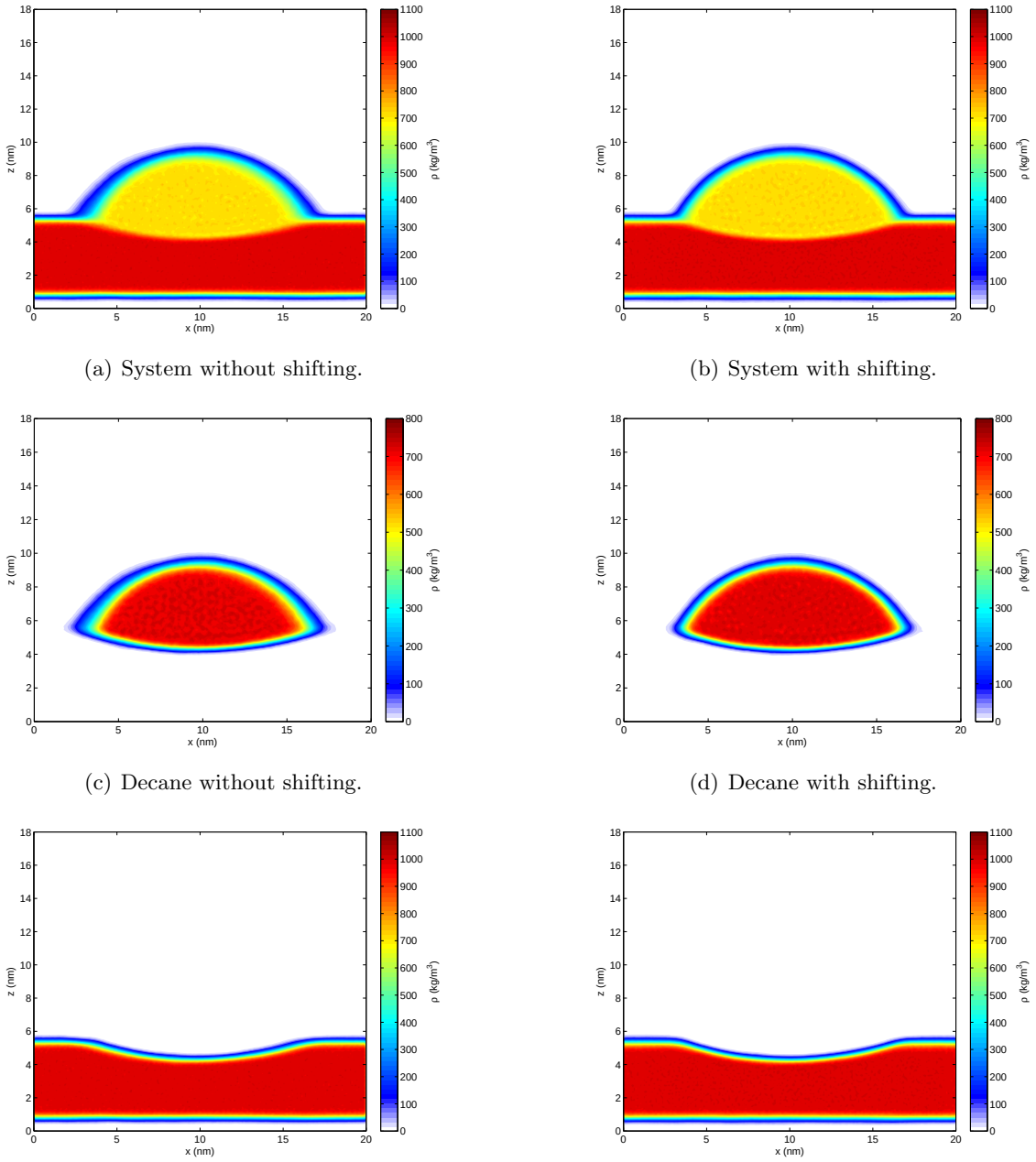

(a) System without shifting.

(b) System with shifting.

(c) Decane without shifting.

(d) Decane with shifting.

(e) Water without shifting.

(f) Water with shifting.

Figure 4.12: Density distributions without (left panels) and with (right panels) shifting techniques for decane–water–vapor three phase system.

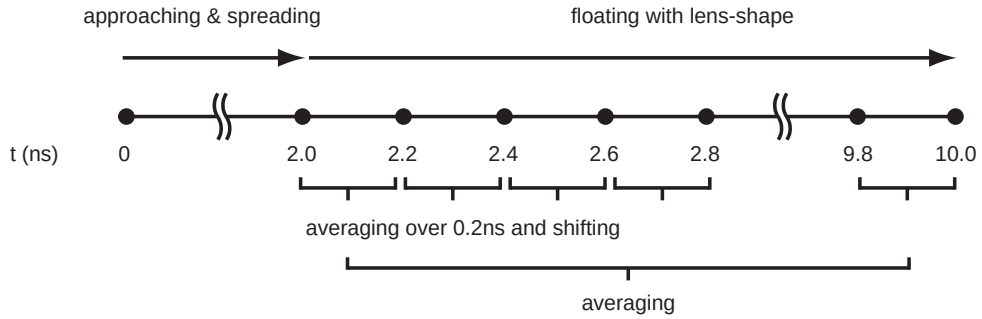

Figure 4.13: Schematic flow for averaging the density and the local pressure distributions.

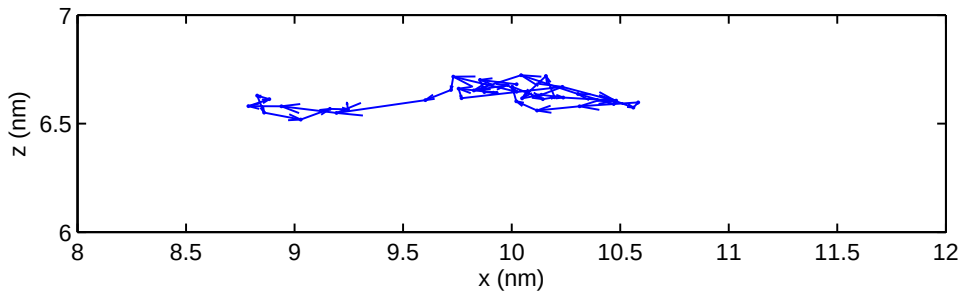

Figure 4.14: Positions of center of mass of decane droplet during 2.0–10.0ns of MD simulation. Each center of mass was calculated from the set of 0.2ns trajectories. Each arrow shows the migration of the center of mass from one time-segment to the next.

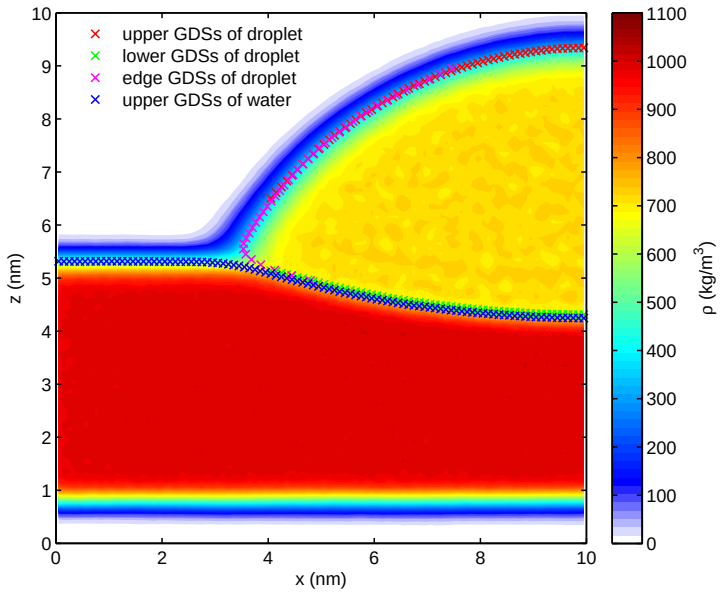

Figure 4.15: Density distribution of system for decane–water–vapor three phase system with the Gibbs dividing surfaces.

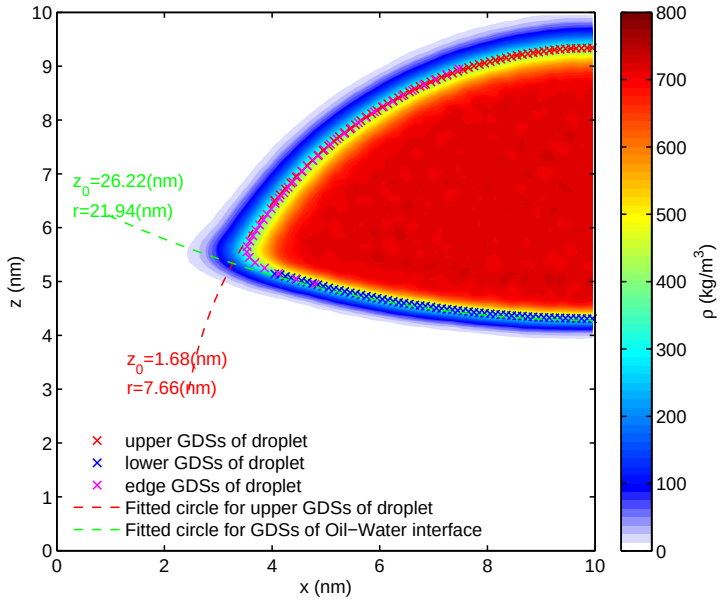

Figure 4.16: Density distribution of decane droplet for decane–water–vapor three phase system with the Gibbs dividing surfaces and the fitted curves.

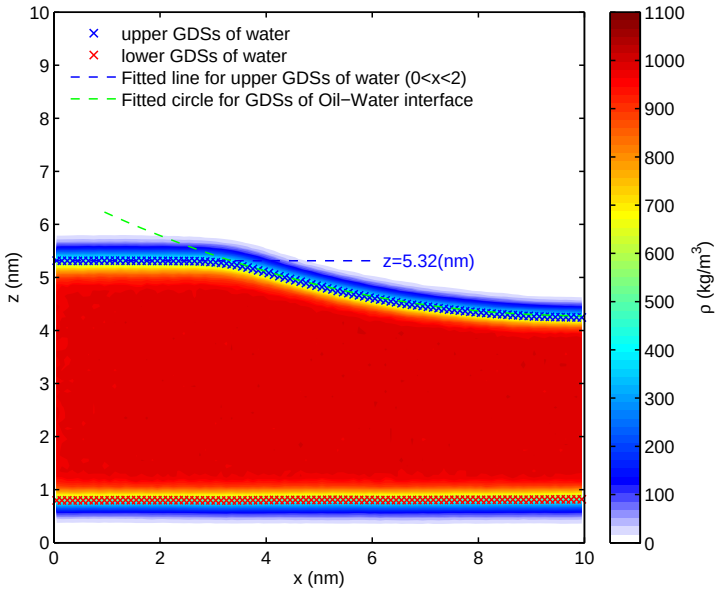

Figure 4.17: Density distribution of water layer for decane–water–vapor three phase system with the Gibbs dividing surfaces and the fitted curves.

density distributions of the decane–water–vapor three phase system. In the following sections, these density distributions were used for further discussions.

The decane droplet clearly shows a lens-shape, which has two different circular surfaces (Fig.4.16). The water layer also shows two surfaces at upper and lower sides (Fig.4.17). The lower side of the water layer is parallel to $xy-$plane, which corresponds to the water–vapor interface. The upper side of the water layer can be separated into two different interfaces: flat surface at the left of the three phase contact line, and circular surface at the right of the three phase contact line. The former surface corresponds to the water–vapor interface, same with the lower surface of the water layer. And the latter surface corresponds to the decane–water interface. It seems that the three phase contact line is located at around x =3nm and z =5.2nm (Fig.4.15).

4.4.2 Gibbs dividing surfaces of decane droplet on water

In order to investigate the detail shape of the decane–water–vapor three phase system, the Gibbs dividing surface (GDS) was used. To calculate the locations of GDS, at first, the density profiles of decane $\rho_{decane}(z)$ and water $\rho_{water}(z)$ along z axis were obtained from Fig.4.16 and Fig.4.17,

respectively. Fig.4.18 shows examples of $\rho_{decane}(z)$ and $\rho_{water}(z)$ at some positions of x. We can see two water–vapor interfaces in the density profiles at x =0, 2 nm. And also we can see three interfaces (water–vapor, oil–water and oil–vapor) in the density profiles at x =6, 8 and 10 nm clearly. On the other hand, at x =4nm, the bulk density of decane did not appear on the $\rho_{decane}(z)$ since it is close to the three phase contact line. Then $\rho_{decane}(z)$ except for those at the vicinity of the three phase contact line and $\rho_{water}(z)$ were fitted by following equation (Benjamin, 1997; Senapati and Berkowitz, 2001):

$$\rho(z) = \frac{\rho_1 + \rho_2}{2} + \frac{\rho_1 - \rho_2}{2}\mathrm{erf}\left(\frac{z - z_{GDS}}{\sqrt{2}w}\right) \tag{4.52}$$

where ρ_1 and ρ_2 are bulk densities at phase 1 and 2, respectively, z_{GDS} is position of GDS, and w is a parameter related with the interfacial thickness, and erf is an error function given by:

$$\mathrm{erf}(x) = \frac{2}{\sqrt{\pi}}\int_0^x e^{-t^2}dt \tag{4.53}$$

The least square methods were used in the fitting procedures. Fig.4.18 also include the fitted lines (Eq.(4.52)). The upper side of each decane surface was fitted using the density profiles over $z > 5.5$nm, and the lower side was fitted using those over $z < 5.5$nm. In addition, the density profiles of the decane droplet were fitted only at $x > 4$nm as mentioned above. At the vicinity of the three phase contact line, the density profiles along x direction were used to fit with Eq.(4.52) (but z changes to x). The GDSs of decane droplet are also shown in Fig.4.16 with its density distribution. For each density profile of water layer, the upper side was fitted using the density profiles of water over $z > 3$nm, and the lower side was fitted using those over $z < 3$nm. The GDSs of water layer are also shown in Fig.4.17 with its density distribution.

Then these GDSs were used to obtain the shape of three interfaces and the location of the three phase contact line in decane–water–vapor three phase system. As mentioned above, in case of the system with a negative spreading coefficient, a liquid droplet on another liquid should form a lens-shape from a macroscopic viewpoint. That is, each two surface of the decane droplet can be fitted with a sphere (a circle in our 2D case). In microscopic viewpoint, the two surfaces can change from the fitted spheres only near its three phase contact line. This may appear within a few molecular lengths from the three phase contact line since this is caused by molecular interactions near that location. The size of this region is discussed in following sections. Therefore the locations of all GDSs far from the three phase contact line of both surfaces of the decane droplet can be fitted by circle shapes as:

$$r^2 = (x - x_0)^2 + (z_{GDS}(x) - z_0)^2 \tag{4.54}$$

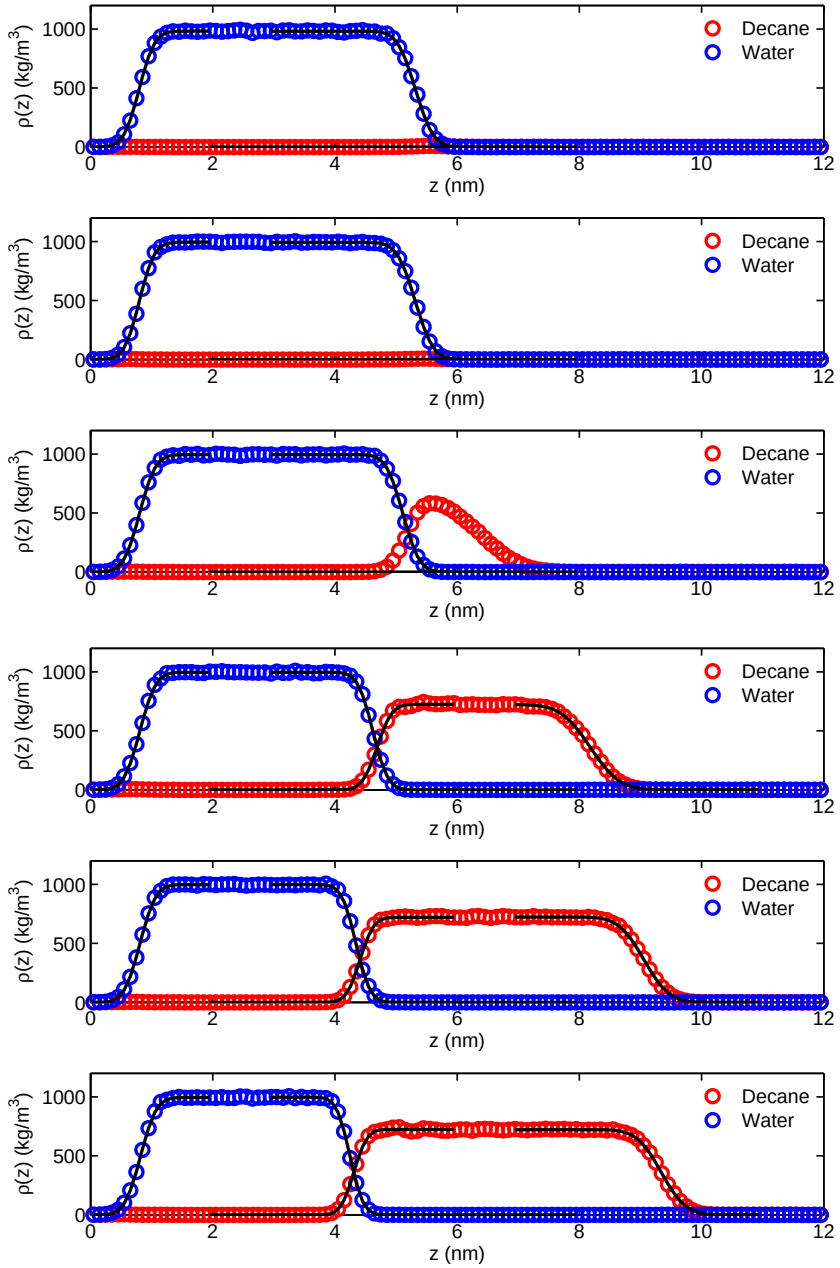

Figure 4.18: Density profiles for decane–water–vapor three phase system along z-axis at x=0, 2, 4, 6, 8 and 10nm (from top to bottom). Solid lines show fitted curves for the density profiles of water and decane.

where r is a radius of fitted circle, x_0 and z_0 are center positions of the circle and z_{GDS} is the positions of GDS. Since our density distributions (Fig.4.15, Fig.4.16 and Fig.4.17) were symmetrical around x =10nm, x_0 can be set to 10nm. The least square methods were used in the fitting procedures. The fitted circle of upper side of droplet (decane–vapor interface) was obtained from the GDSs at $x > 5$nm, and are also shown in Fig.4.16 with its fitted parameters. As shown, this circle is fitted very well with the GDSs. For the interface between the decane droplet and the water layer, there are two series of GDSs defined by each density profile. As shown in Fig.4.16 and Fig.4.17, these GDSs are almost parallel to each other and the average distance between these GDSs is quite small around 0.05nm. Therefore we defined that the GDSs of the decane–water interface locate at the middle point of two series of GDSs. The fitted circle of GDSs of the decane–water interface was shown in Fig.4.16 and Fig.4.17 with its fitted parameters. And finally, the location of the upper water surface was obtained from the z-positions of the GDSs of upper side of the water layer at $x < 2$nm as a horizontal line. The line is also shown in Fig.4.17 with its z position. It seems that all fitted lines can reproduce the shape of the decane–water–vapor three phase system well except for the region near the three phase contact line, and intersect at one point.

The geometry near the three phase contact line is shown in Fig.4.19. Fig.4.19 includes the locations of the GDSs with their interfacial thickness parameters w, the fitted lines, the location of the intersection of the fitted lines, the direction of each interface at that location and the contact angles. The intersection of the two circles was calculated to $x = 3.27$nm and $z = 5.34$nm. The z-position of the intersection is quit close to the position of water surface (z =5.32nm, Fig.4.17), the difference is only 0.02nm. Therefore we can define the location of this intersection as that of the three phase contact line for the decane–water–vapor three phase system. The slopes of the tangent of two circles at the three phase contact line were calculated to 61.49 ° and −17.87 ° (Fig.4.19). The directions of each interface at the three phase contact line are described in Fig.4.19 as the arrows. As mentioned above, these contact angles are independent from size of the system, since our system is 2D.

4.4.3 Local pressure distributions

The pressure tensor distribution, $\boldsymbol{p}(x, z)$, called as local pressure distributions, were calculated every 1 ps using the output trajectories and averaged over every 0.2 ns length of 10.0 ns MD simulation. Then these local pressure distributions were averaged over 2.0–10.0 ns by using same

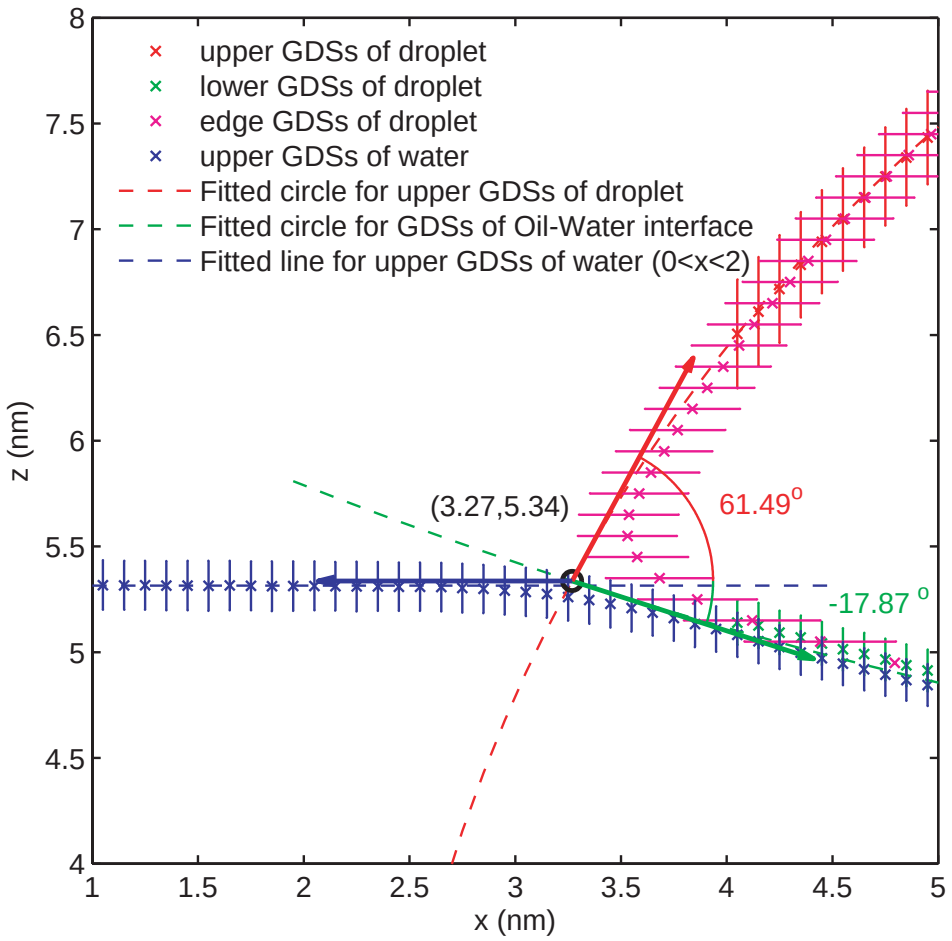

Figure 4.19: Geometry at vicinity of three phase contact line for decane–water–vapor three phase system. Length of the line at each GDS shows the interface thickness w in Eq.(4.52). The intersection of two fitted circles is shown. The difference of z values between the intersection and the horizontal fitted line for the water–vapor interface is only 0.02nm. The arrows show the directions of the tangent of fitted lines at the intersection. Contact angles were obtained from these directions and the horizontal fitted line for the water–vapor interface.

techniques in the calculation of density distributions. The distribution of each element in the local pressure tensor for our decane–water–vapor three phase system are shown in Fig.4.20.

p_{xx} and p_{yy} have big negative values along to three interfaces, whereas very small magnitude at bulk phases. And they show similar values at the lower and upper water–vapor interfaces. This is because both interfaces are parallel to xy-plane. It means that both p_{xx} and p_{yy} work toward to the direction tangent to these interfaces. Furthermore, same results were obtained at the decane–water and decane–vapor interfaces near the symmetrical axis of the decane droplet ($x = 10$nm). This is also because it can be seen that these interfaces are almost parallel to xy-plane at this location (Fig.4.20(a) and Fig.4.20(c)). On the other hand, p_{zz} shows small magnitude compared to p_{xx} and p_{yy} at these three interfaces far from the three phase contact line. p_{zz} has positive values at the water side of the decane–water and water–vapor interfaces , while negative value at the other side. And the shear stresses, p_{xy}, p_{yz} and p_{zx}, are almost zero far from the three phase contact line (Fig.4.20(b), Fig.4.20(d) and Fig.4.20(f), respectively). The reason for almost zero values of p_{xy} and p_{yz} is that the three phase system is 2D with the continuity in y direction. So with same reason, even near the three phase contact line, p_{xy} and p_{yz} show almost zero values. And the reason for almost zero values of p_{zx} far from the three phase contact line is that the interfaces are almost parallel to xy-plane at these regions.

However, at the vicinity of the three phase contact line, the local pressure distributions show different behaviors, because two of three interfaces are no longer parallel to xy-plane (Fig.4.19) and the molecular interactions among the three phases cannot be ignored. p_{yy} have still large magnitude similar to the interfaces far from the three phase contact line (Fig.4.20(c)). This is because even near three phase contact line, all interface are parallel to y direction. On the other hand, p_{xx} decrease its magnitude, especially on the decane–vapor interface (Fig.4.20(a)). In contrast, p_{zz} increase its magnitude at the decane–vapor interface (Fig.4.20(e)). For shear component, p_{xy} and p_{yz} are still almost zero (Fig.4.20(b) and Fig.4.20(d), respectively), because all interfaces are always parallel to y direction. On the other hand, p_{zx} shows minus values on the decane–vapor interface, and plus values on the decane–water interface.

In order to investigate the effect of the slopes of the interfaces, the local pressure distributions (Fig.4.20) were rotated based on the polar coordinate around the three phase contact line, using Eq.(4.27). Fig.4.21 show the local pressure distributions on the polar coordinate, p_{nn}, p_{tt} and p_{nt}. The subscripts n and t indicate the direction normal and tangential, respectively, to the interfaces as shown in Fig.4.21(a). Note that all interfaces near the three phase contact line were assumed to be along with the outward direction from that location. As shown in Fig.4.21, all

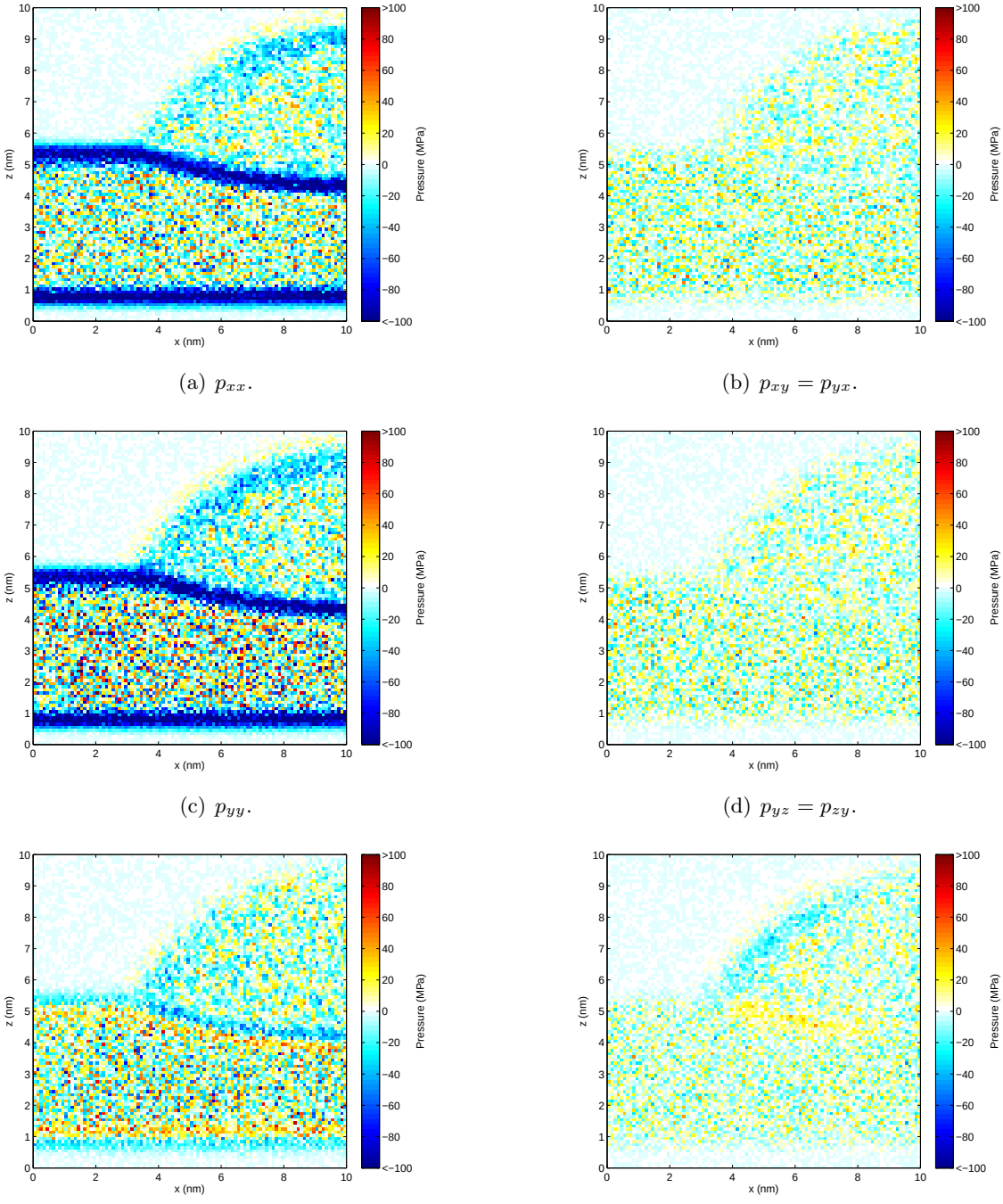

(a) p_{xx}.

(b) $p_{xy} = p_{yx}$.

(c) p_{yy}.

(d) $p_{yz} = p_{zy}$.

(e) p_{zz}.

(f) $p_{zx} = p_{xz}$.

Figure 4.20: Local pressure distributions for decane–water–vapor three phase system.

rotated local pressure distributions show inhomogeneity only at around $r < 1$nm. On the other hand, at outside of this region, they do not show such inhomogeneity. That shows a consistency of our assumption that all interfaces are along with outward direction. As shown in Fig.4.22, in microscopic view point, the interfaces and the three phase contact line are not just planes and line (lines and point, in case of 2D view). So they should have some thicknesses and region with molecular scale. Thus, this region, which shows these inhomogeneity in Fig.4.21(b), Fig.4.21(c) and Fig.4.21(d), indicates the three phase contact region. The line tension may be caused by the excess free energy in this region and calculated by integrating that over this region.

4.4.4 Interfacial tensions from local pressure distributions

In this section, the interfacial tensions for each interface are calculated from the local pressure distributions, $\boldsymbol{p}(x, z)$. Interfacial tension, γ_{ij}, between phase i and j can be calculated from local pressure distributions by following equation (Kirkwood and Buff (1949) and see also Eq.(3.1)):

$$\begin{aligned}\gamma_{ij} &= \int [p_B - p_{tt}]\, dn \\ &= \int [p_{nn} - p_{tt}]\, dn \end{aligned} \tag{4.55}$$

where p_B is the pressure at the bulk phase, p_{nn} and p_{tt} are the pressures normal and tangential to the interface, respectively. p_B can be express as:

$$p_B = \text{Trace}\,(\boldsymbol{p}) \qquad \text{at bulk phase.} \tag{4.56}$$

As mentioned above, we can assume that all interface are parallel to xy-plane far from the three phase contact line. Therefore, at these interfaces, Eq.(4.55) can be rewritten as follows:

$$\gamma_{ij} = \int \Delta p dz \tag{4.57}$$

where

$$\Delta p = p_{zz} - \frac{p_{xx} + p_{yy}}{2} \tag{4.58}$$

The integral in Eq.(4.57) are performed from the bulk of phase i to phase j.

Fig.4.23 shows the local pressure profiles and the pressure difference (Eq.(4.58)) averaged over $0 \leq x \leq 2$nm. As discussed above, p_{xx} and p_{yy} show similar and big negative values on each interface. p_{zz} shows negative and positive values on the vapor and water side, respectively, near the water–vapor interfaces. At the bulk regions, although p_{xx}, p_{yy} and p_{zz} fluctuate, they have

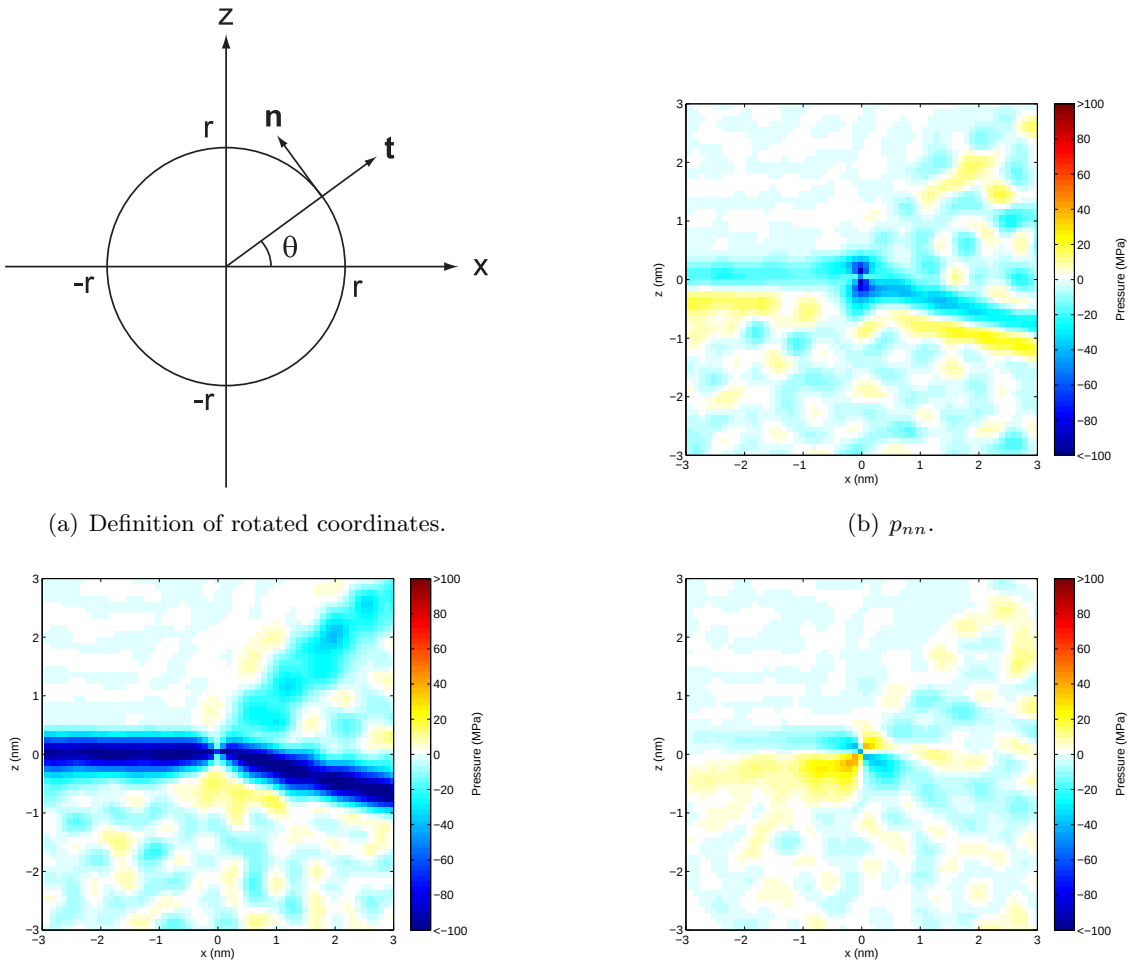

(a) Definition of rotated coordinates.

(b) p_{nn}.

(c) p_{tt}.

(d) $p_{nt} = p_{tn}$.

Figure 4.21: Rotated local pressure distributions for decane–water–vapor three phase system at vicinity of three phase contact line. The center position was shifted to the three phase contact line obtained from the density distribution (Fig.4.19).

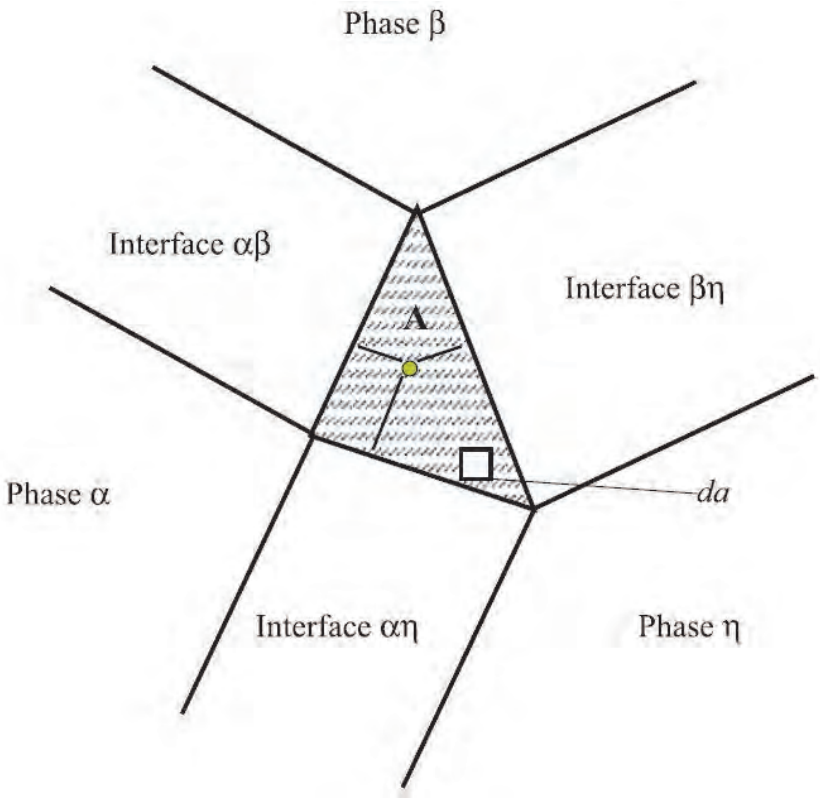

Figure 4.22: The shaded triangle represents the three phase confluence zone created as the result of truncation of the three interfaces (Amirfazli and Neumann, 2004). According to them, the size of three phase confluence zone is a few molecular diameters.

similar and almost constant values. And the shear components, p_{xy}, p_{yz} and p_{zx}, are almost zero over all range of z in Fig.4.23. The Δp shows local maximums at around the positions of GDSs in two interfaces. The interfacial tensions of upper water surface was calculated by using the pressure profiles in Fig.4.23 with Eq.(4.57) to 59.87 mN/m (Table.4.2). The standard error in Table.4.2 was calculated from 40 interfacial tension values, that each value was obtained from 0.2ns length of the local pressure distributions data (Fig.4.13).

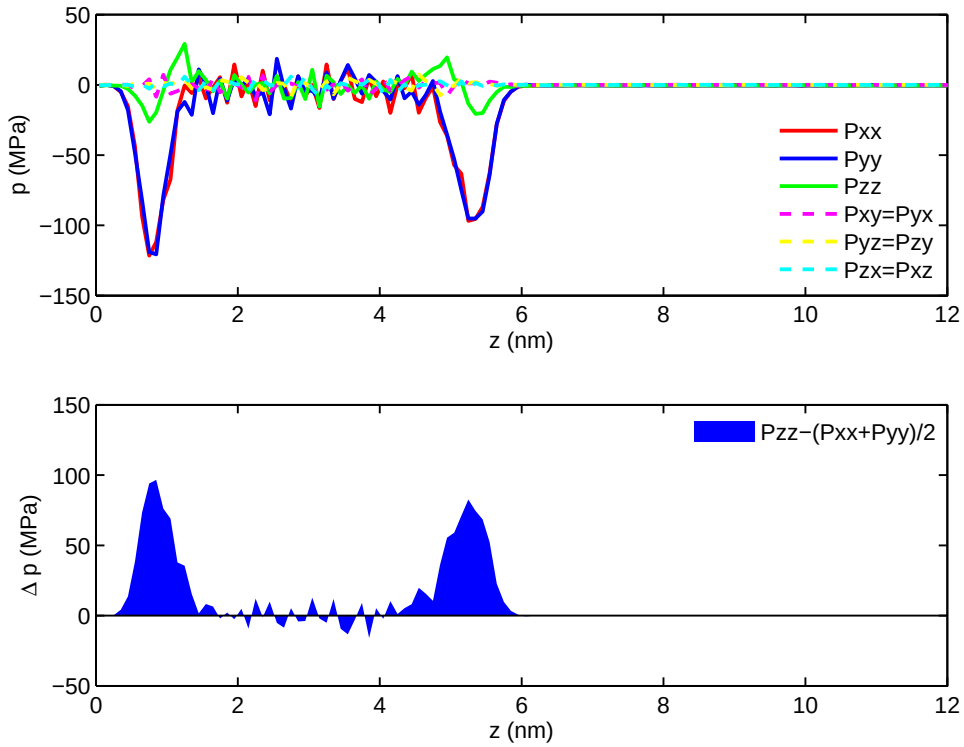

Figure 4.23: Local pressure profiles (top) and pressure difference profile (bottom) for decane–water–vapor three phase system along with z-axis averaged over $0 \leq x \leq 2$nm. Two regions in the pressure difference profile correspond to two water–vapor interfaces. The integrated value of each region gives the interfacial tension γ.

Fig.4.24 shows the local pressure profiles and the pressure difference (Eq.(4.58)) averaged over $8 \leq x \leq 10$nm. Similar to Fig.4.23, the p_{xx} and p_{yy} show similar values. And the shear components, p_{xy}, p_{yz} and p_{zx} are almost zero over all range of z. The Δp shows local maximums at around the position of two interfaces. The interfacial tension between decane and water was calculated over the range of $3 \leq z \leq 6$nm to 50.61 mN/m. And the interfacial tension of upper

Table 4.2: Interfacial tensions from local pressure distributions

Phase 1	Phase2	x (nm)	z (nm)	IFT† (mN/m)
Water	Vapor	0–10	0–2	58.75 ± 0.42
Water	Vapor	0–2	4–7	59.87 ± 1.13
Decane	Water	8–10	3–6	50.61 ± 2.82
Decane	Vapor	8–10	8–12	19.45 ± 2.32

† (Average)±(Standard error)

surface of decane was calculated over the range of $8 \leq z \leq 12$nm to 19.45 mN/m.

In addition to these interfaces, the interfacial tension of lower surface of water (the water–vapor interface) was also calculated over the range of $0 \leq x \leq 10$nm and $0 \leq z \leq 2$nm to 58.75 mN/m. This value is in good agreement with that of upper water surface (59.87 mN/m).

In order to confirm the accuracies of these interfacial tensions calculated from our decane–water–vapor three phase system, these values were compared with those which were calculated from MD simulations of their three two-phase interface systems. The results are shown in Table.4.3. From Table.4.2 and Table.4.3, it can be said that the interfacial tensions were calculated reasonably at far from three phase contact line in the decane–water–vapor three phase system.

Table 4.3: Interfacial tensions from MD simulations of interface systems.

Phase 1	Phase2	IFT (mN/m)
Water	Vapor	58.76
Decane	Water	50.06
Decane	Vapor	19.18

These calculated interfacial tensions of decane–water and decane–vapor interfaces are ∼ 5mN/m lower, and those of water–vapor interfaces are also ∼ 12mN/m lower than their experimental values (Goebel and Lunkenheimer, 1997). This is because the interfacial tensions by Eq.(4.55) are often underestimated in MD methods due to excluding of long-range interactions far from the cut-off distance. The correction value to their interfacial tensions by the long-range interaction may be a few mN/m (∼ 5mN/m in case of water–vapor interface according to Alejandre et al. (1995)).

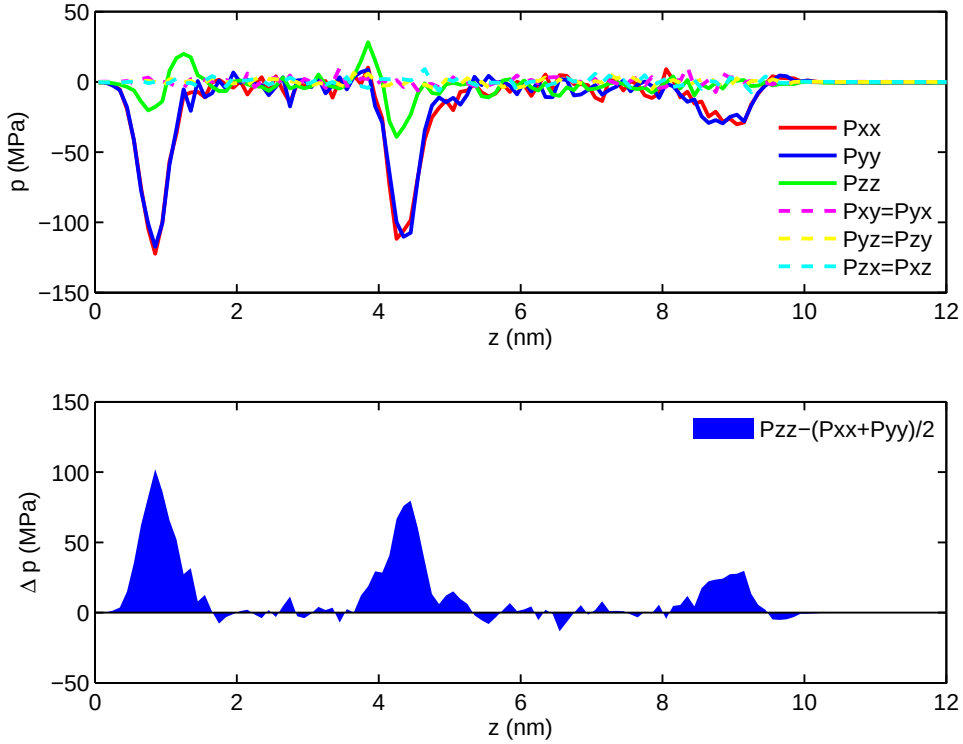

Figure 4.24: Local pressure profiles (top) and pressure difference profile (bottom) for decane–water–vapor three phase system along with z-axis averaged over $8 \leq x \leq 10$nm. Three regions in the pressure difference profile correspond to three interfaces, water–vapor, decane–water and decane–vapor, from left to right. The integrated value of each region gives the interfacial tension γ.

From the interfacial tensions of the three interfaces, the Neumann triangle relationship (Eq.(4.3)) can be determined. Eq.(4.3) can be rewritten by:

$$0 = \gamma_{ov} \sin\theta_1^0 - \gamma_{ow} \sin\theta_2^0 \tag{4.59}$$

and

$$\gamma_{wv} = \gamma_{ov} \cos\theta_1^0 + \gamma_{ow} \cos\theta_2^0 \tag{4.60}$$

where θ_1^0 and θ_2^0 are macroscopic contact angles, which can be determined by three interfacial tensions. Here θ_2^0 is taken in a clockwise fashion. From Eq.(4.59) and Eq.(4.60), one finds,

$$\cos\left(\theta_1^0 + \theta_2^0\right) = \frac{\gamma_{wv}^2 - \gamma_{ov}^2 - \gamma_{ow}^2}{2\gamma_{ov}\gamma_{ow}} \tag{4.61}$$

The calculated values of $\cos(\theta_1^0 + \theta_2^0)$ from the interfacial tensions (Table.4.2) by Eq.(4.61) is 0.33 ± 0.17. Here ± 0.17 indicate the standard error of $\cos(\theta_1^0 + \theta_2^0)$, calculated with law of propagation of errors. So the $\theta_1^0 + \theta_2^0$ is 70.87 °. The $\theta_1^0 + \theta_2^0$ from the interfacial tensions is similar to that from density distributions (79.36 ° = 61.49 ° + 17.87 °, Fig.4.19). This value is within the range of the error ($\theta_1^0 + \theta_2^0 = 81.05$ ° in case of $\cos(\theta_1^0 + \theta_2^0) = 0.33 - 0.17$).

4.4.5 Line tension from local pressure distributions

In this section, the line tension is calculated from the local pressure distributions (Fig.4.20). As mentioned above, we have three types of expression of the line tension as a function of local pressure distributions (Eq.(4.10), Eq.(4.11) and Eq.(4.13)). Among these equations, Eq.(4.13) is the most useful when we calculate the line tension from local pressure distributions. This is because the other two equations (Eq.(4.10), Eq.(4.11)) need the assumption that all three interfaces are planar even far from the three phase contact line. As shown in the density distributions (e.g. Fig.4.19), the decane surface and decane–water interface show circular shapes relatively near the three phase contact line. On the other hand, Eq.(4.13) can give the line tension τ only from the local pressure distributions and the bulk pressure value. To calculate the line tension, here we introduced the distance dependent line tension, $\tau(r)$, as:

$$\tau(r) = \iint_{B(r)} \left[p_{xx} + p_{zz} - p_{yy} - p_B\right] dxdz \tag{4.62}$$

where the $B(r)$ is circular region with a radium of r, which is centered at the three phase contact line (Fig.4.19). Fig.4.25 shows the distribution of the integrand in Eq.(4.62) at the vicinity of

the three phase contact line. Fig.4.26 shows $\tau\,(r)$ with increasing the distance r from the three phase contact line. The bulk pressure p_B was obtained from the average value of p_{xx}, p_{yy} and p_{zz} in each three bulk phase: decane droplet, water layer and vapor (Eq.(4.56)).

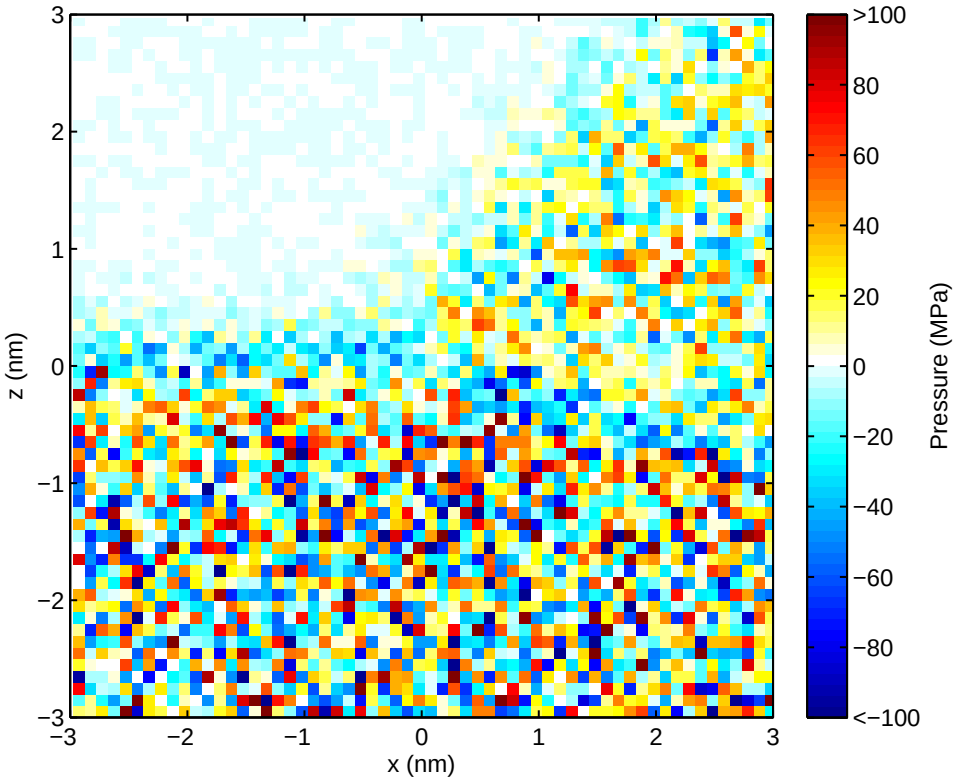

Figure 4.25: The distributions of the integrand of Eq.(4.62), $p_{xx} + p_{zz} - p_{yy} - p_B$. The center position was shifted to the three phase contact line obtained from the density distribution (Fig.4.19).

Eq.(4.62) gives the line tension τ at the infinity of r:

$$\begin{aligned}\tau &= \lim_{r\to\infty} \tau\,(r) \\ &= \lim_{r\to\infty} \iint_{B(r)} \left[p_{xx} + p_{zz} - p_{yy} - p_B\right] dxdz \end{aligned} \tag{4.63}$$

From Fig.4.26, we found that $\tau(r)$ converged at around $r > 1.4$nm. So the line tension τ of the decane–water–vapor three phase system was obtained to -8.2×10^{-12}N. This τ is intrinsic value for this system. There is no effect coming from any difficulty in experiments, such as contamination, impurities of materials, adsorptions of unwelcome molecules and so on (Amirfazli and Neumann, 2004; Checco et al., 2003, 2006; Kerins and Boiteux, 1983; Lee et al., 1985;

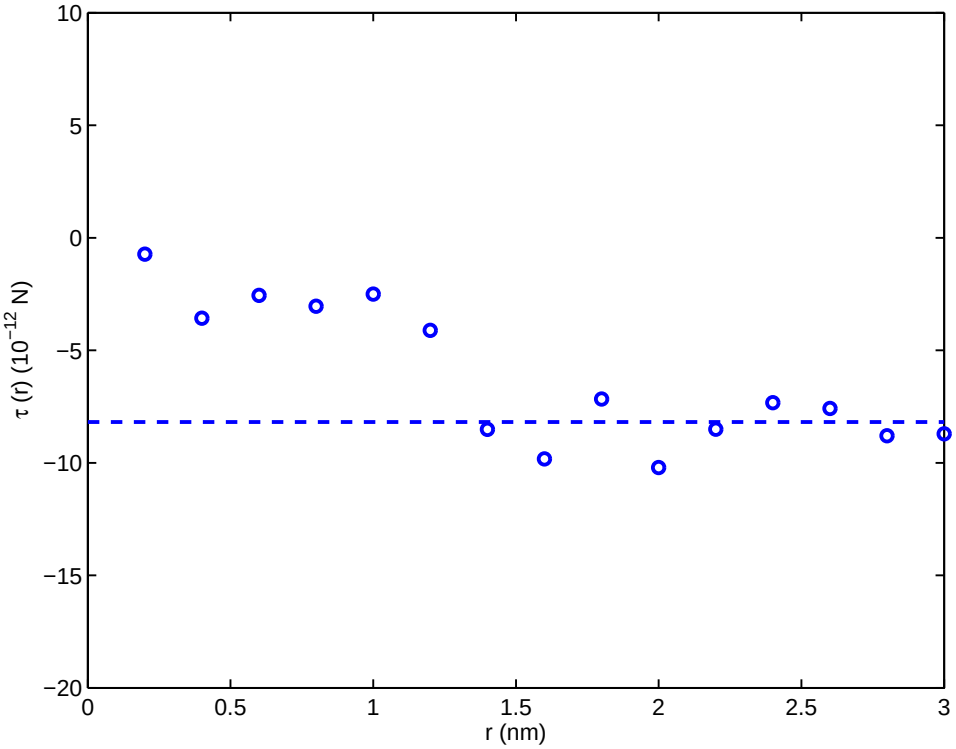

Figure 4.26: Distance dependent line tension $\tau(r)$ for decane–water–vapor three phase system against the distance r from the three phase contact line. The circle region $B(r)$ with the radius r was used for the integration. Dashed line shows the average value of $\tau(r)$ obtained from the last 5 values.

Tarazona and Navascues, 1981; Widom and Widom, 1991). Previous researches with theoretical approaches have reported that the line tension τ can be either positive or negative values and its magnitude is 10^{-12}–10^{-11}N (Drelich, 1996). Our value of -8.2×10^{-12}N is within this range. Therefore, it can be said that our techniques by MD have determined the line tension successfully.

4.4.6 Size dependence of contact angle

Once the line tension is obtained, the size dependence of the contact angle can be estimated by a general form of Neumann triangle (Eq.(4.2)). In our case, Eq.(4.2) can be rewritten as:

$$0 = \gamma_{ov} \sin\theta_1 - \gamma_{ow} \sin\theta_2 \tag{4.64}$$

and

$$\gamma_{wv} = \gamma_{ov} \cos\theta_1 + \gamma_{ow} \cos\theta_2 + \frac{\tau}{R} \tag{4.65}$$

where R is radius of the contact line of a lens-shape droplet. At the infinity of R, Eq.(4.64) and Eq.(4.65) produce classical expression of Neumann triangle (Eq.(4.59) and Eq.(4.60), respectively). From Eq.(4.65) and Eq.(4.60), one finds,

$$\gamma_{ov} \cos\theta_1 + \gamma_{ow} \cos\theta_2 = \gamma_{ov} \cos\theta_1^o + \gamma_{ow} \cos\theta_2^0 - \frac{\tau}{R} \tag{4.66}$$

Here Eq.(4.66) is defined as $G(R)$. Fig.4.27 show the $G(R)$ as a function of $1/R$. From Eq.(4.64) and Eq.(4.66) (=G), one finds,

$$\cos(\theta_1 + \theta_2) = \frac{G^2 - \gamma_{ov}^2 - \gamma_{ow}^2}{2\gamma_{ov}\gamma_{ow}} \tag{4.67}$$

Fig.4.28 show the value of $\theta_1+\theta_2$ as a function of the radius R. From Fig.4.28, the size dependence of the contact angle in our decane–water–vapor three phase system can be estimated. The effect caused by the line tension is big when the size of the droplet is small. However the difference of the contact angles between at $R = 10$nm and macroscopic scale is only less than 3 °, while a lot of experimental researches have reported significant big difference (That means big magnitude of the line tension). So although these experimental researches have been done carefully, they might not to be able to remove the effects by contamination, impurities of materials, adsorptions of unwelcome molecules and so on.

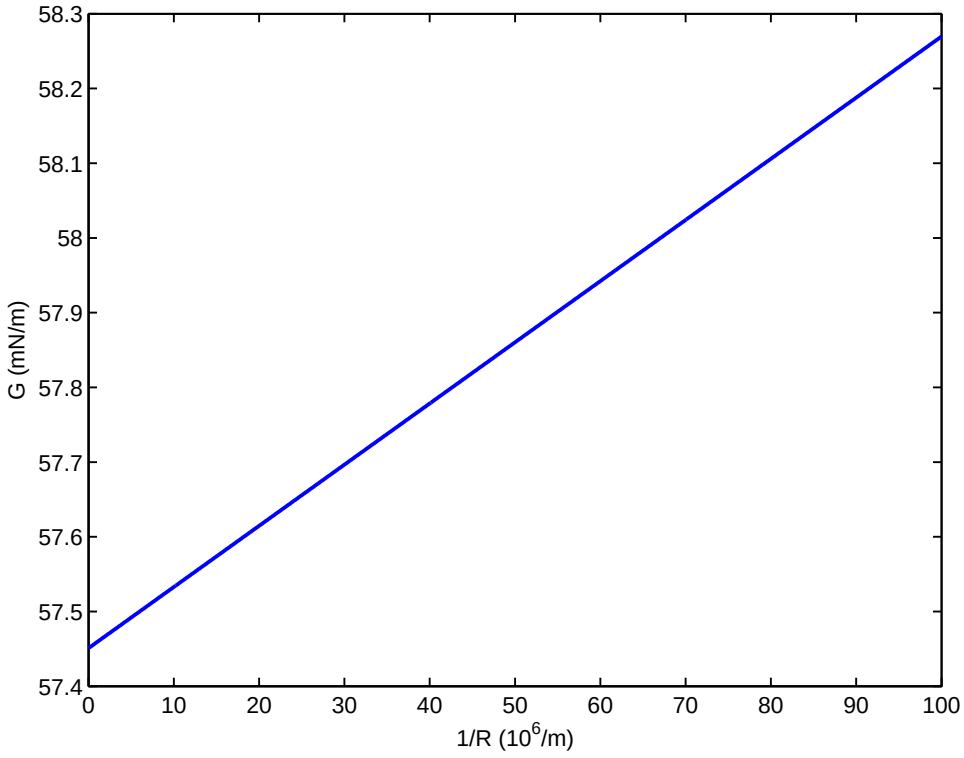

Figure 4.27: G against the inverse of the radius of the contact line $1/R$.

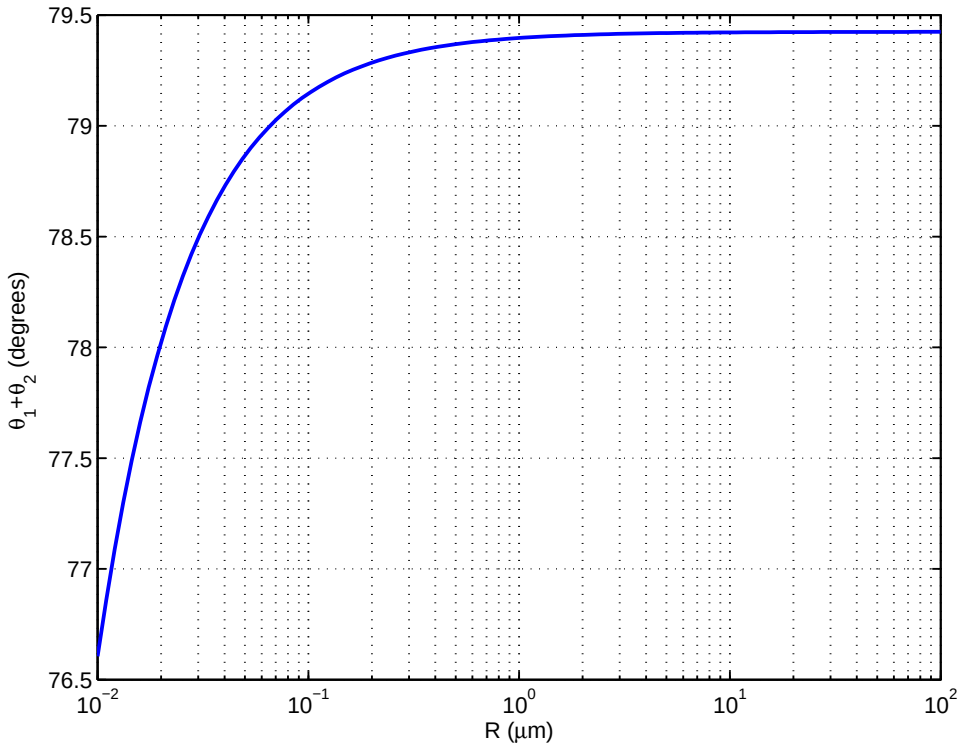

Figure 4.28: Contact angle inside of droplet $\theta_1 + \theta_2$, versus the radius of the contact line R.

4.5 Conclusions

The interfacial equilibrium of three liquid phases of decane, water and their vapor has been investigated by MD methods as an apparent 2D system. The decane droplet approached to water surface due to their van der Waals attractive interactions, and then floated on water surface during MD simulation, similar to an actual liquid droplet on the other liquid surface. That is one of reasons why experimental observation of a liquid droplet on the other liquid surface is difficult. The Gibbs dividing surfaces at each interface were determined by the density profiles. The three interfaces were defined as the fitted curve of the Gibbs dividing surfaces. The interface of decane droplet far from the three phase contact line could be fitted with circle very well as macroscopic aspect shows. The three interfaces intersected at almost one position, so the three phase contact line was defined as the intersection of these three interfaces. The interfacial tension of each interface was calculated from the local pressure distributions at far from three phase contact line successfully, and in good agreement with the one which was obtained by other MD calculation done independently. The convenient expression of the equation of the line tension was derived as a function of the local pressure distributions and applied. The distance dependent line tension converged at around 1.4 nm far from the three phase contact line as shown theoretically, and the line tension of our decane–water–vapor three phase system has been obtained to -8.2×10^{-12}N successfully. This is intrinsic value for this three phase system, so that the effects caused by any other phenomena, such as impurity of the droplet, to the line tension can be considered by taking it as a reference state.

Chapter 5

Molecular Dynamics of Multicomponent-Oil–Water–Vapor Three Phase System

5.1 Introduction

In Chapter 3, the interfacial equilibrium of light-oil model and water interface has been investigated by Molecular Dynamics (MD) methods. The results have shown that the aromatic components in a hydrocarbon mixture, such as crude oil, strongly accumulate at the oil–water interface due to their weak hydrogen bonding with water molecules, and determine the interfacial properties, such as interfacial tension. And also, in Chapter 4, the interfacial equilibrium of three liquid phases of decane, water and their vapor has been investigated by MD methods. We have investigated the local structure of decane droplet on water at the three phase contact line and calculated the interfacial tensions and the intrinsic line tension from the local density distributions, successfully.

In this chapter, the three liquid phase system are extended. The ternary mixture of heptane, decane and toluene has been used as the liquid droplet instead of only decane in Chapter 4.

5.2 Details of Molecular Dynamics

5.2.1 Materials

The droplet model used in this study was a ternary mixture (called as multicomponent-oil in followings) of toluene, heptane, and decane, with 250, 250, and 500 molecules, respectively. The water molecules were modeled by the SPC/E model (Alejandre et al., 1995; Berendsen et al., 1987). Table.5.1 shows the chemical formulas and structures in the multicomponent-oil–water–vapor three phase system. A revised version of the CHARMM 27 force field (Davis et al., 2008; Klauda et al., 2005; MacKerell Jr et al., 1998) was used to model the heptane, decane and toluene molecules. All parameters are listed in Appendix A

Table 5.1: Chemical formulas and structures in multicomponent-oil–water–vapor three phase system.

Component	Formula	Structure
n-heptane	C_7H_{16}	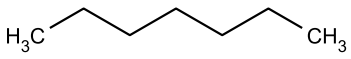
n-decane	$C_{10}H_{22}$	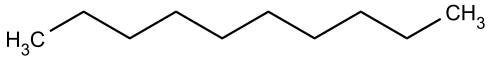
toluene	C_7H_8	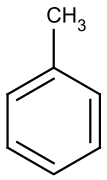
water	H_2O	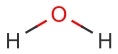

5.2.2 Preparation of multicomponent-oil–water–vapor three phase system

First, the droplet model was calculated from NVT simulation to form a cylindrical shape (Fig.4.9(a)). Then the thin water layer was calculated from NPnAT (Fig.4.9(b)). Then the cylindrical droplet was put next to the thin water layer to give continuity in the y-direction (Fig.4.9(c)), and hence, a 2-dimensional profile in the x and z plane. Finally, the multicomponent-oil–water–vapor three phase system was equilibrated by NVT simulation.

5.2.3 Details of Molecular Dynamics

The MD simulation was performed using the GROMACS package (Hess et al., 2008; Van Der Spoel et al., 2005). In all NVT and NPnAT calculations, the temperature was controlled by the Nose-Hoover thermostat (Nose, 1984) to 298 K. In NPnAT calculations, the pressure was controlled by the Parrinello-Rahman method (Parrinello and Rahman, 1982) to 0.1 MPa. The particle mesh Ewald summation (Essmann et al., 1995) was used for the electrostatic interactions, and a cutoff of 1.4 nm was used for calculation of the van der Waals interactions. A 1.0 fs time step was used and output coordinates were obtained every 1.0 ps. Calculations run for 10.0 ns showed sufficiently close approach to equilibrium states. Snapshots of molecular distributions were prepared by Visual Molecular Dynamics (VMD) software Humphrey et al. (1996). After that, the local pressure distributions were calculated using an adapted version of GROMACS that allows the computation of local pressures (Ollila et al., 2009), by re-calculating the output trajectories with 0.1 grid size.

5.3 Results and Discussion

5.3.1 Molecular distribution inside oil droplet

Fig.5.1 shows snapshots of unit cell for MD simulation of the multicomponent-oil–water–vapor three phase system at the beginning and after 5.0 ns of the simulation. The size of unit cell is same with that in Chapter 4, 20 nm $\times$ 6.88916 nm $\times$ 18 nm $\times$ in x, y and z direction, respectively. Similar to the case in Chapter 4, once the simulation started, the oil droplet approached the water surface with contact at around 10 ps due to their van der Waals attractive interactions. Then, the oil droplet started to spread on the water surface. Finally, the oil droplet formed a lens-shape at around 1.0 ns of simulation time. After that, the oil droplet kept its shape apart from the effect of thermal fluctuations. Snapshots of toluene, heptane, and decane molecules at the beginning and after 10.0 ns of simulation are shown in Fig.5.3, respectively. At the beginning of the simulation, all hydrocarbons distributed homogeneously in the cylindrical oil droplet. However after equilibrated, toluene molecules accumulated at the oil–water interface (Fig.5.4(c)) as expected from the results in Chapter 3. And it can be seen that small amount of their molecules evaporated from their bulk phase. Some of the evaporated hydrocarbon molecules went through the periodic boundary condition and adsorbed on the lower side of

the water surface. These phenomenon are more clearer in the multicomponent-oil–water–vapor three phase system than in the decaene–water–vapor three phase system (Fig.4.11).

The density distribution of each component was calculated from each trajectory, by using same procedures described in Chapter 4. Fig.5.5 shows the locations of the center of mass of the multicomponent-oil droplet from 2.0 ns to 10.0 ns. It can be seen the random floating of the oil droplet on water surface. The density distributions of system and each component after removing the effect by this floating are shown in Fig.5.6. As shown in Chapter 3, the strong accumulation of toluene molecules at the oil–water interface was clearly observed (Fig.5.6(e)). On the other hand, the decane concentrations were higher far from both the oil–water interface than near the interfaces (Fig.5.6(d)). In other words, this shows the desorption of decane molecules at the interface. To investigate the details of these phenomena, density profiles were calculated along the z axis, and a few examples are shown in Fig.5.7. The density profiles near the symmetrical line ($x = 10$nm), three regions can be identified along the z axis of the droplet: the water region, the bulk multicomponent-oil region and the vapor region. As shown in Fig.5.4(c) and Fig.5.6(e), toluene molecules accumulates strongly at the oil–water interface. The maximum density of toluene at the oil–water interface is about 3 times of its density in the bulk region. This is similar value which was observed in Chapter 3. From Fig.5.7, the accumulation of toluene at the oil–water interface was accompanied by weak accumulation of heptane molecules. At the oil–vapor interface, all density profiles change gradually (Fig.5.7) but the density profiles show the weak accumulation of heptane at the oil–vapor interface. As mentioned in Chapter 3, this phenomena can be explained using the surface tension difference between the hydrocarbon–water interfaces.

At the three phase contact line, toluene and heptane molecules showed preferential accumulation relative to decane molecules (Fig.5.6(c), Fig.5.6(d) and Fig.5.6(e)). And also, they showed the thin film on water surface, connecting the three phase contact region, especially in case of toluene. The film thickness of about 0.5 nm from the density distribution of toluene is comparable to its molecular size. During the MD simulation, toluene molecules in the oil spread as a thin film over the water surface followed by spreading of the bulk oil (Fig.5.2). In general, components of an oil mixture which move preferentially to the three phase contact line will spread on the water surface ahead of the bulk oil.

The Gibbs dividing surface (GDS) were obtained with same techniques described in Chapter 4. Then the GDSs were fitted with circular shapes (Eq.(4.54)). The calculated GDSs and fitted circles are shown in Fig.5.6 with their density distribution and fitted parameters. All fitted lines

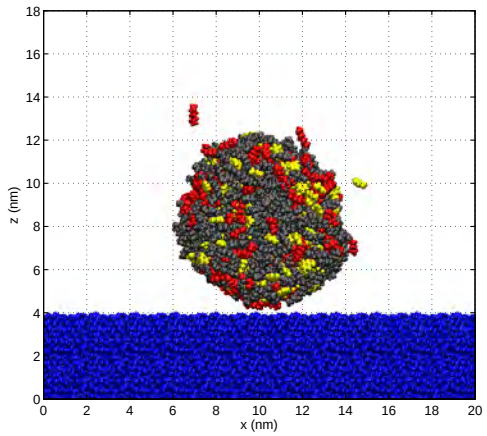

(a) side view at 0 ns

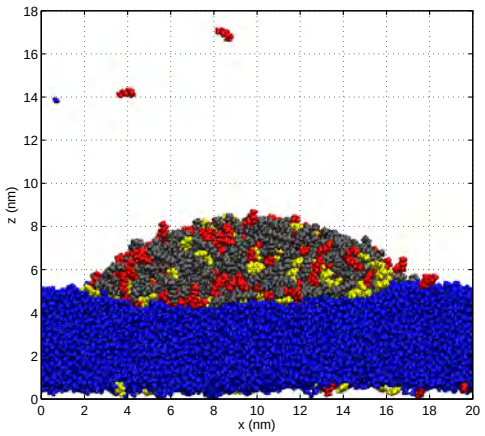

(b) side view at 5 ns

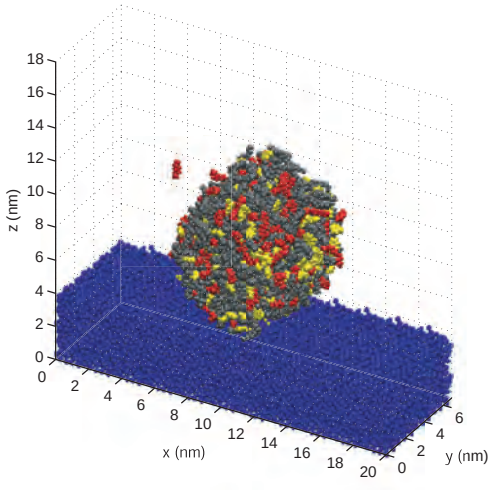

(c) 3D view at 0 ns

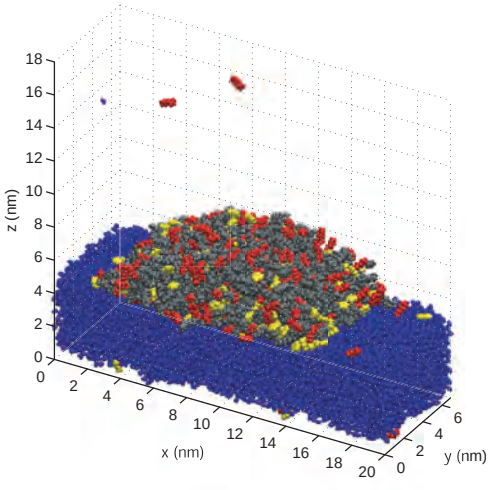

(d) 3D view at 5 ns

Figure 5.1: Snapshots of multicomponent-oil-on-water system (red, heptane; gray, decane; yellow, toluene; blue, water).

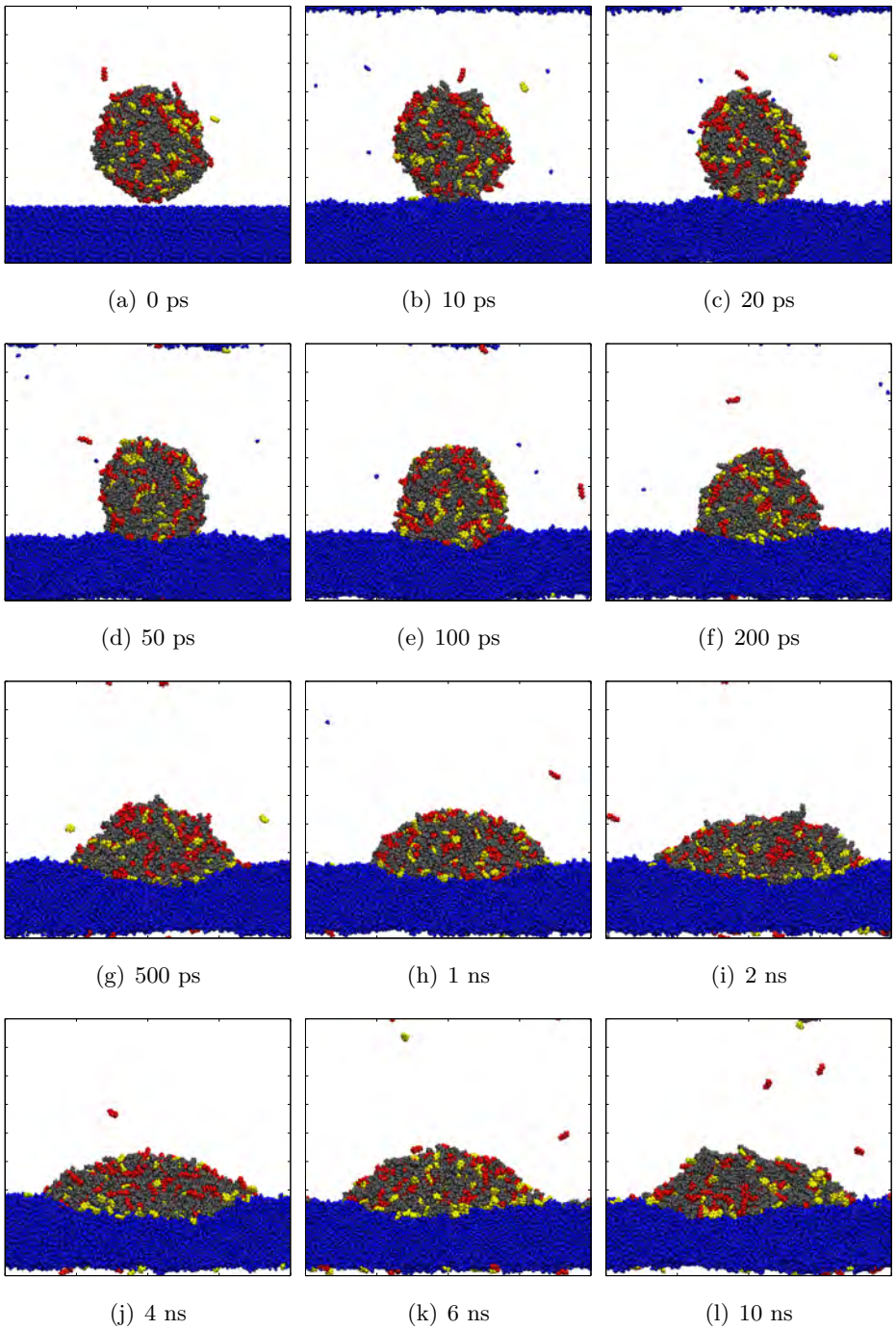

(a) 0 ps (b) 10 ps (c) 20 ps

(d) 50 ps (e) 100 ps (f) 200 ps

(g) 500 ps (h) 1 ns (i) 2 ns

(j) 4 ns (k) 6 ns (l) 10 ns

Figure 5.2: Series of snapshots of multicomponent-oil-on-water system (red, heptane; gray, decane; yellow, toluene; blue, water). The size of each panel corresponds to Fig.5.1(a).

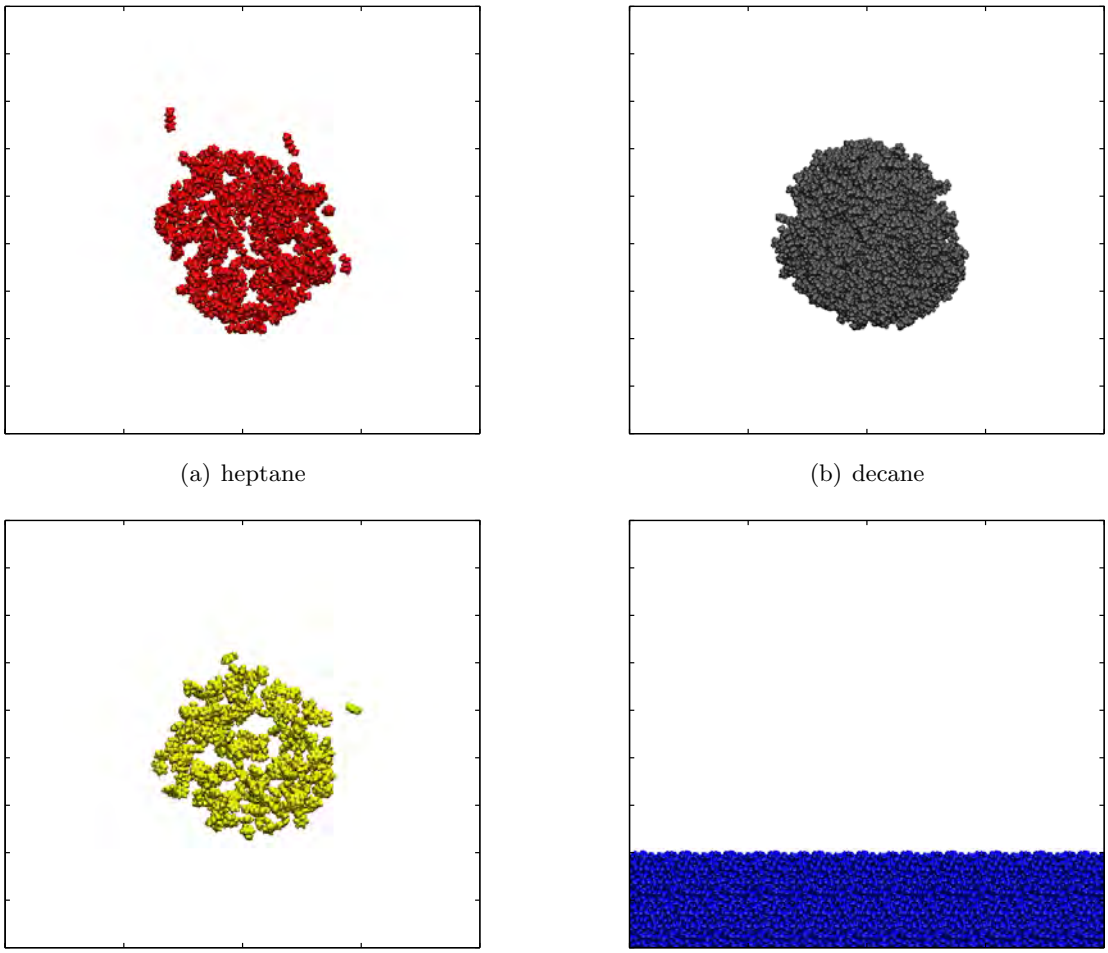

(a) heptane (b) decane

(c) toluene (d) water

Figure 5.3: Snapshots of each component for multicomponent-oil–water–vapor three phase system at the beginning of calculation. The size of each panel corresponds to Fig.5.1(a).

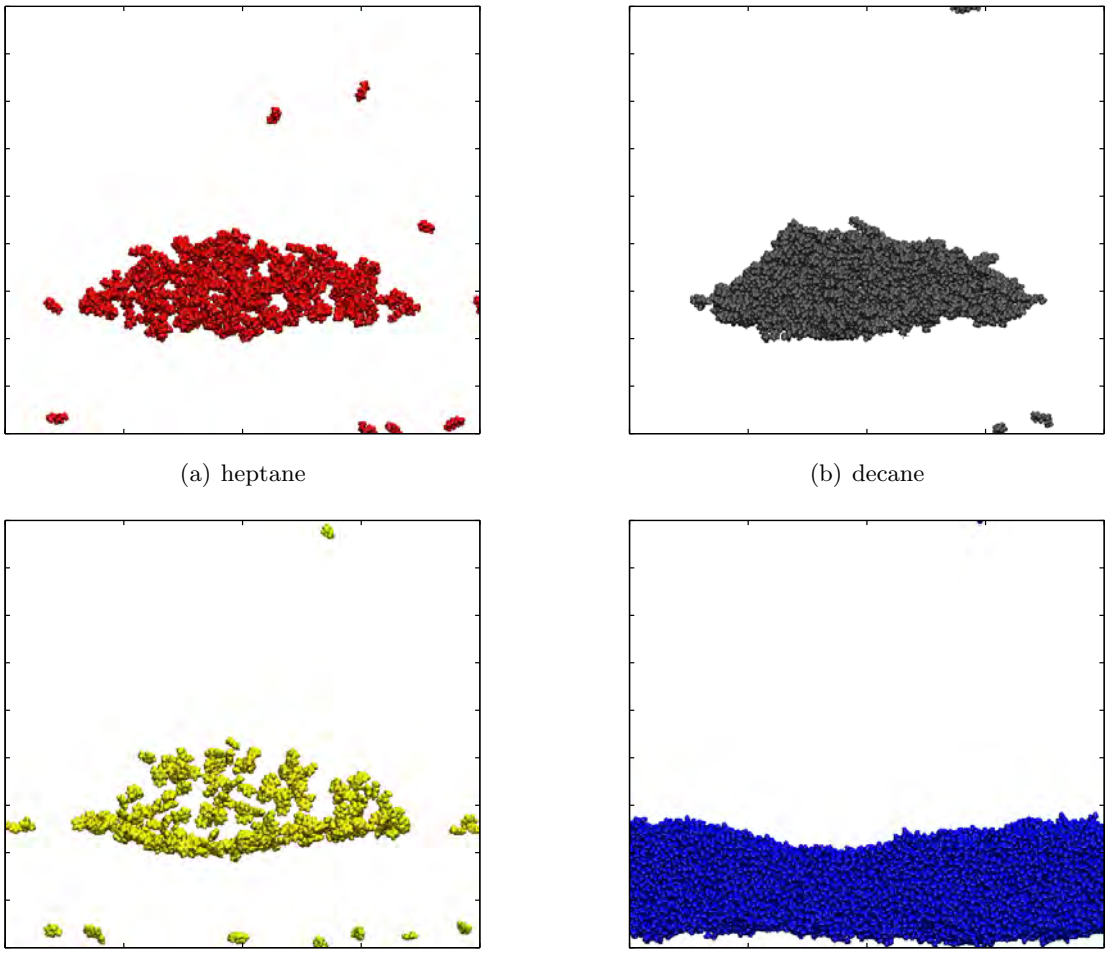

(a) heptane

(b) decane

(c) toluene

(d) water

Figure 5.4: Snapshots of each component for multicomponent-oil–water–vapor three phase system at $t = 10$ns. The size of each panel corresponds to Fig.5.1(a).

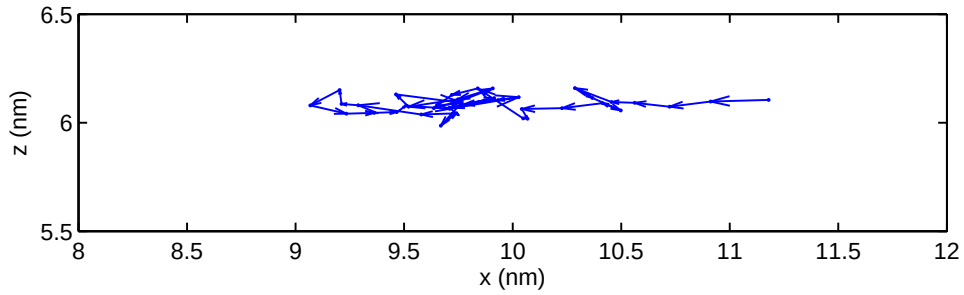

Figure 5.5: Positions of center of mass of multicomponent-oil droplet during 2.0–10.0ns of MD simulation. Each center of mass was calculated from the set of 0.2ns trajectories. Each arrow shows the migration of the center of mass from one time-segment to the next.

produce the shape of the three phase system very well. The geometry near the three phase contact line is shown in Fig.5.8. Fig.5.8 includes the locations of the GDSs with their interfacial thickness parameters w, the fitted lines, the location of the intersection of the fitted lines, the direction of each interface at that location and the contact angles. The intersection of the two circles was calculated to $x = 3.24$ nm and $z = 5.20$ nm. The slopes of the tangent of two circles at the three phase contact line was calculated to 49.82 ° and -16.87 ° (Fig.5.8). These value are lower than those in Chapter 4. That means the multicomponent-oil forms a thin-lens-shape on water surface, compared to in case of pure decane. Moreover, the GDSs at the vicinity of the three phase contact line show different behavior among the multicomponent and the pure decane cases. In case of the pure decane, the GDSs always located inside of the fitted circles. This is reasonable because the GDSs calculated from the density profiles correspond roughly to the positions of 50% of the bulk density, and the three phase contact region is the region of the coexistence of three phases (oil, water and vapors). On the other hand, in case of the multicomponent-oil, the GDSs located outside (vapor-side) of the fitted circle. And from Fig.4.19 and Fig.5.8, at the region of the three phase contact line, the interfacial thickness parameters for the multicomponent-oil–water–vapor three phase system is wider than that for the decane–water–vapor three phase system. These phenomenon are the effect caused by the impurity of the oil droplet. They might come from the change in the intensity of the accumulation of heptane and toluene molecules at the oil–water and oil–vapor interface between near and far from the three phase contact line.

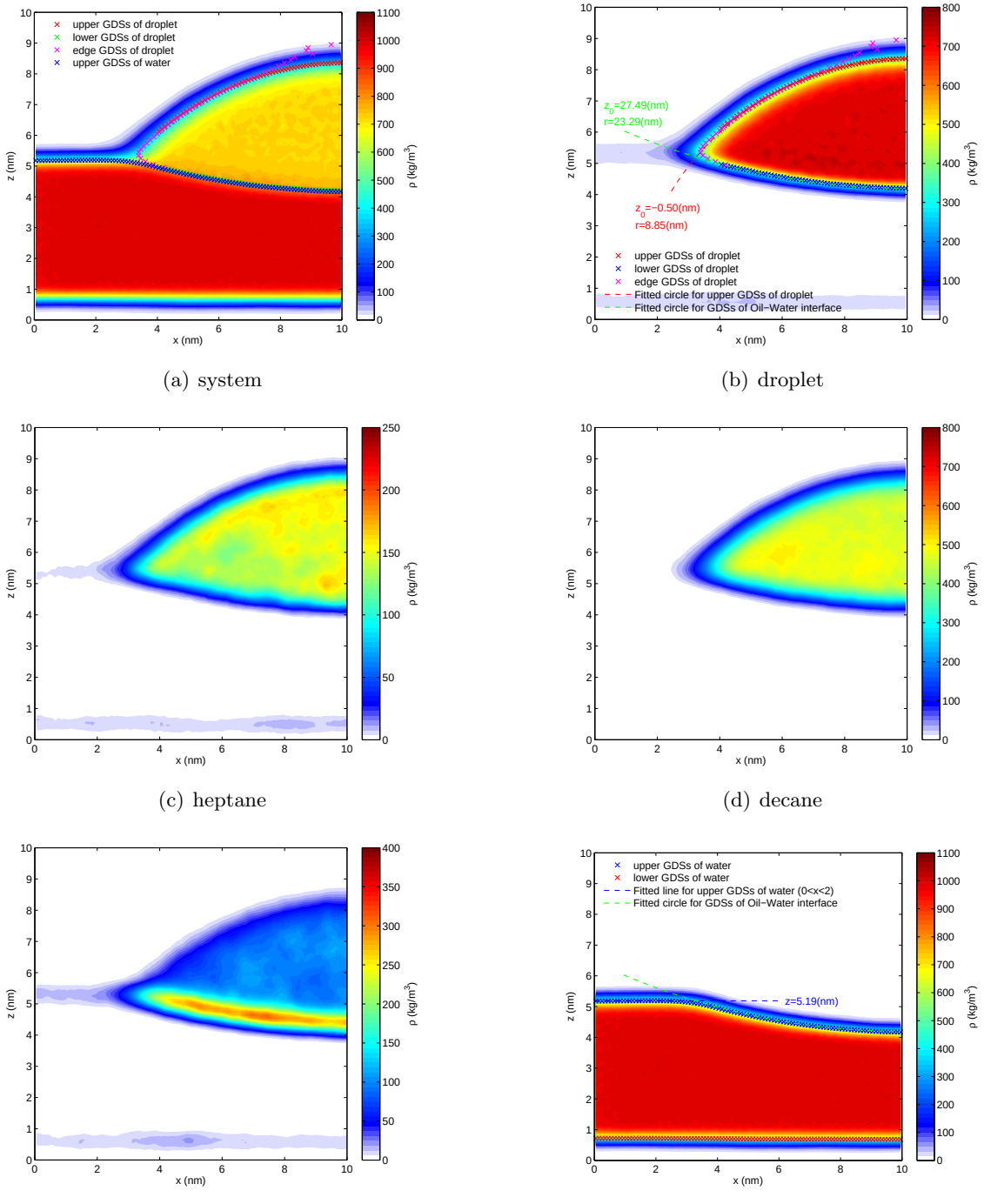

(a) system

(b) droplet

(c) heptane

(d) decane

(e) toluene

(f) water

Figure 5.6: Density distributions for multicomponent-oil–water–vapor three phase system. The density distribution of droplet was calculated as the summation of the densities of heptane, decane and toluene. The locations of Gibbs dividing surfaces and the fitted curves are also shown.

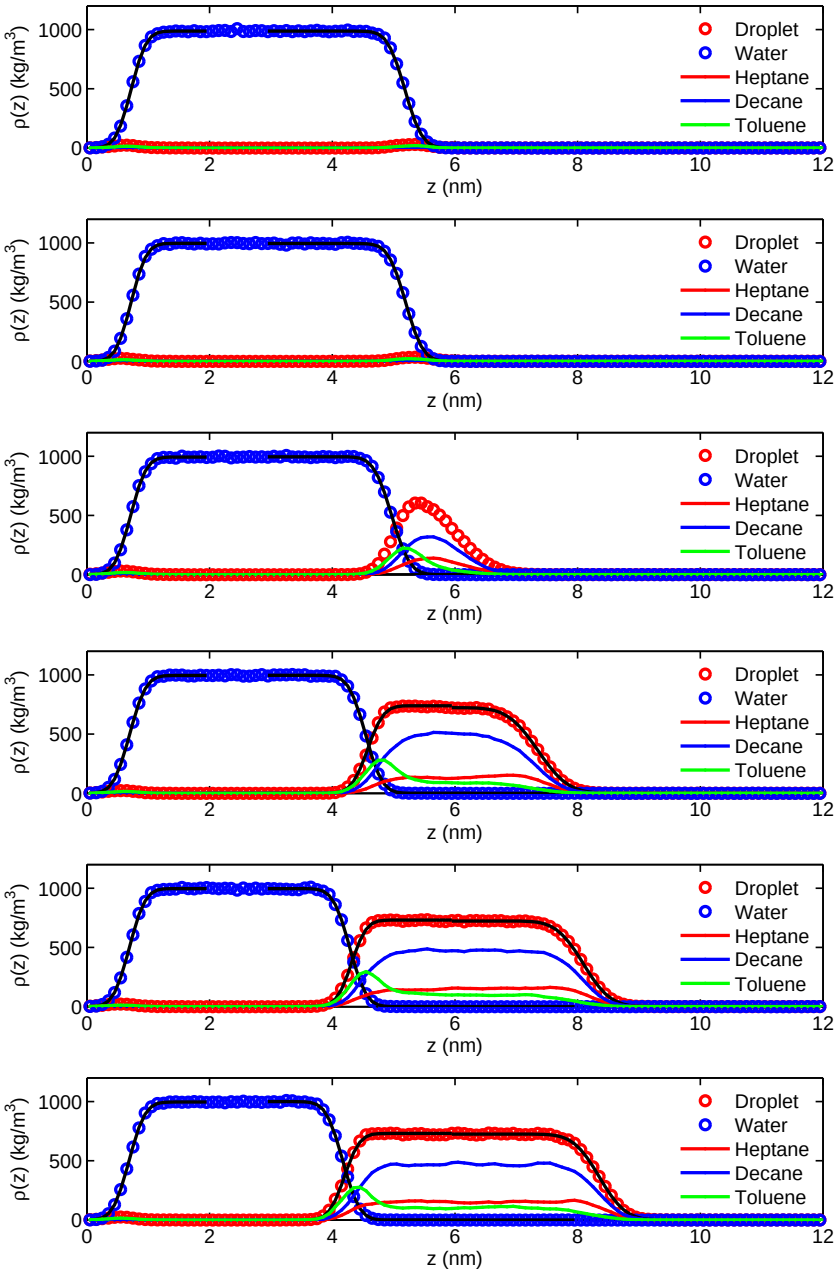

Figure 5.7: Density profiles for multicomponent-oil–water–vapor three phase system along z-axis at x=0, 2, 4, 6, 8 and 10nm (from top to bottom). The density profile of droplet was calculated as the summation of the densities of heptane, decane and toluene. Solid lines show fitted curves for the density profiles of water and droplet.

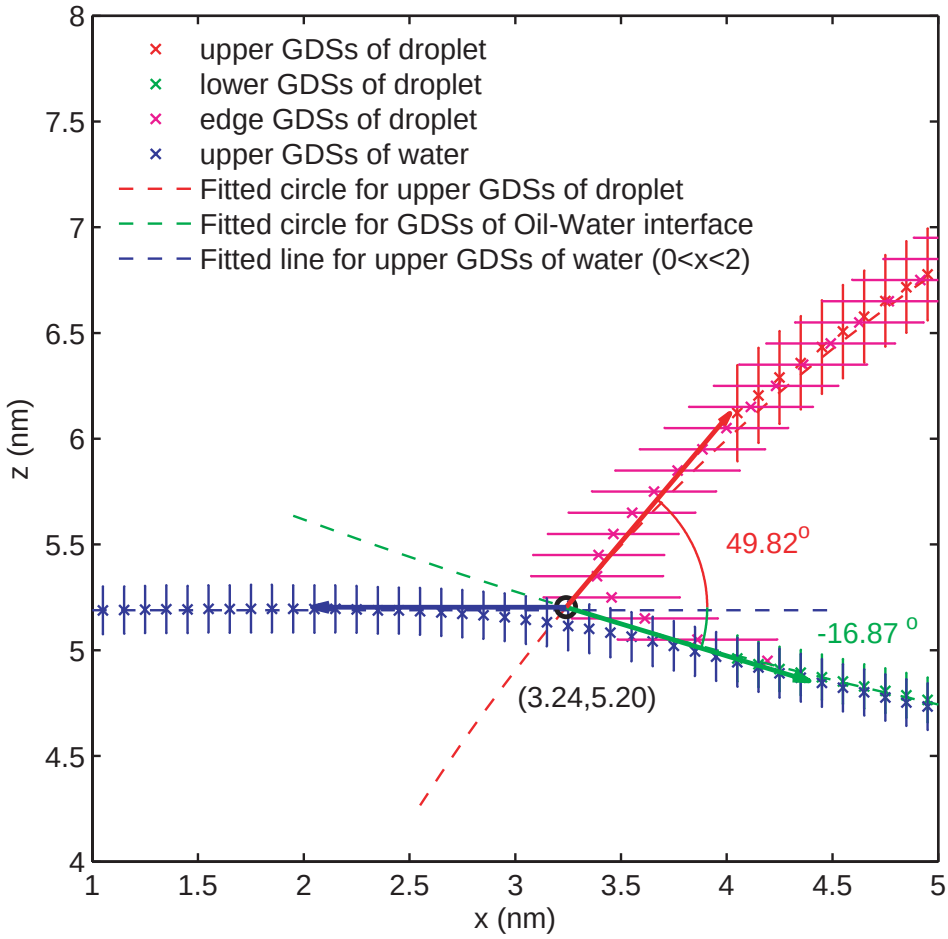

Figure 5.8: Geometry at vicinity of three phase contact line for multicomponent-oil–water–vapor three phase system. Length of the line at each GDS shows the interface thickness w in Eq.(4.52). The intersection of two fitted circles is shown. The difference between z value of the intersection and the horizontal fitted line for the water–vapor interface is only less than 0.04nm. The arrows show the directions of the tangent of fitted lines at the intersection. Contact angles were obtained from these directions and the horizontal fitted line for the water–vapor interface.

5.3.2 Interfacial tension and line tension

In this section, the interfacial tensions and the line tension are calculated from the local pressure distributions. The methods are same with those described in Chapter 4. The local pressure distribution of each component in the pressure tensor, $\boldsymbol{p}$ in the multicomponent-oil–water–vapor three phase system are shown in Fig.5.9. All local pressures showed similar distributions with Chapter 4. p_{xx} and p_{yy} showed similar values at the lower and upper water–vapor interfaces since both interfaces are parallel to xy-plane. Furthermore, same results were obtained at the oil–water and oil–vapor interfaces near the symmetrical axis of the oil droplet ($x = 10$nm). On the other hand, p_{zz} showed small magnitude compared to p_{xx} and p_{yy}. This is because it can be seen that these interfaces are almost parallel to xy-plain at this location (Fig.5.6). And hence, the shear stresses, p_{xy}, p_{yz} p_{zx}, are almost zero far from the three phase contact line (Fig.5.9(b), Fig.5.9(d) and Fig.5.9(f), respectively). And also, the local pressures at the vicinity of the three phase contact line show similar distributions with Chapter 4 p_{yy} have still large magnitude similar to the interfaces far from the three phase contact line since all interface are parallel to y direction even near three phase contact line. On the other hand, p_{xx} decrease its magnitude slightly, especially on the oil–vapor interface. In contrast, p_{zz} increase its magnitude at the oil–vapor interface. For shear component, p_{xy} and p_{yz} are almost zero because all interfaces are always parallel to y direction. On the other hand, p_{zx} shows minus values on the oil–vapor interface, and plus values on the oil–water interface. This phenomena can be analyzed with same techniques with Chapter 4, and it results the size of the three phase contact region.

Then the interfacial tensions were calculated at each three interfaces from the local pressure profiles. The results are shown in Table.5.2. Fig.5.10 shows the local pressure profiles and the pressure difference (Eq.(4.58)) across the water–vapor interface. The interfacial tension of upper water surface was calculated by using this pressure profiles to 59.99 mN/m. And Fig.5.11 shows the local pressure profiles and the pressure difference (Eq.(4.58)) across the oil–water and oil–vapor interfaces. The interfacial tensions of the oil–water and oil–vapor interface was calculated to 46.18 and 19.31 mN/m, respectively. As discussed in Chapter 3, the strong accumulation of aromatics make the interfacial tension decrease. So this effect can be seen the interfacial tension of the multicomponent-oil–water interface (46.18 mN/m) compared with one of the decane–water interface (50.61 mN/m, Chapter 4). Then the Neumann triangle relationship (Eq.(4.3)) for the multicomponent-oil–water–vapor three phase system was discussed. From Eq.(4.61), the $\cos(\theta_1^0 + \theta_2^0)$ was calculated to 0.61 ± 0.20. So the $\theta_1^0 + \theta_2^0$ was calculated to 52.18 °. Although

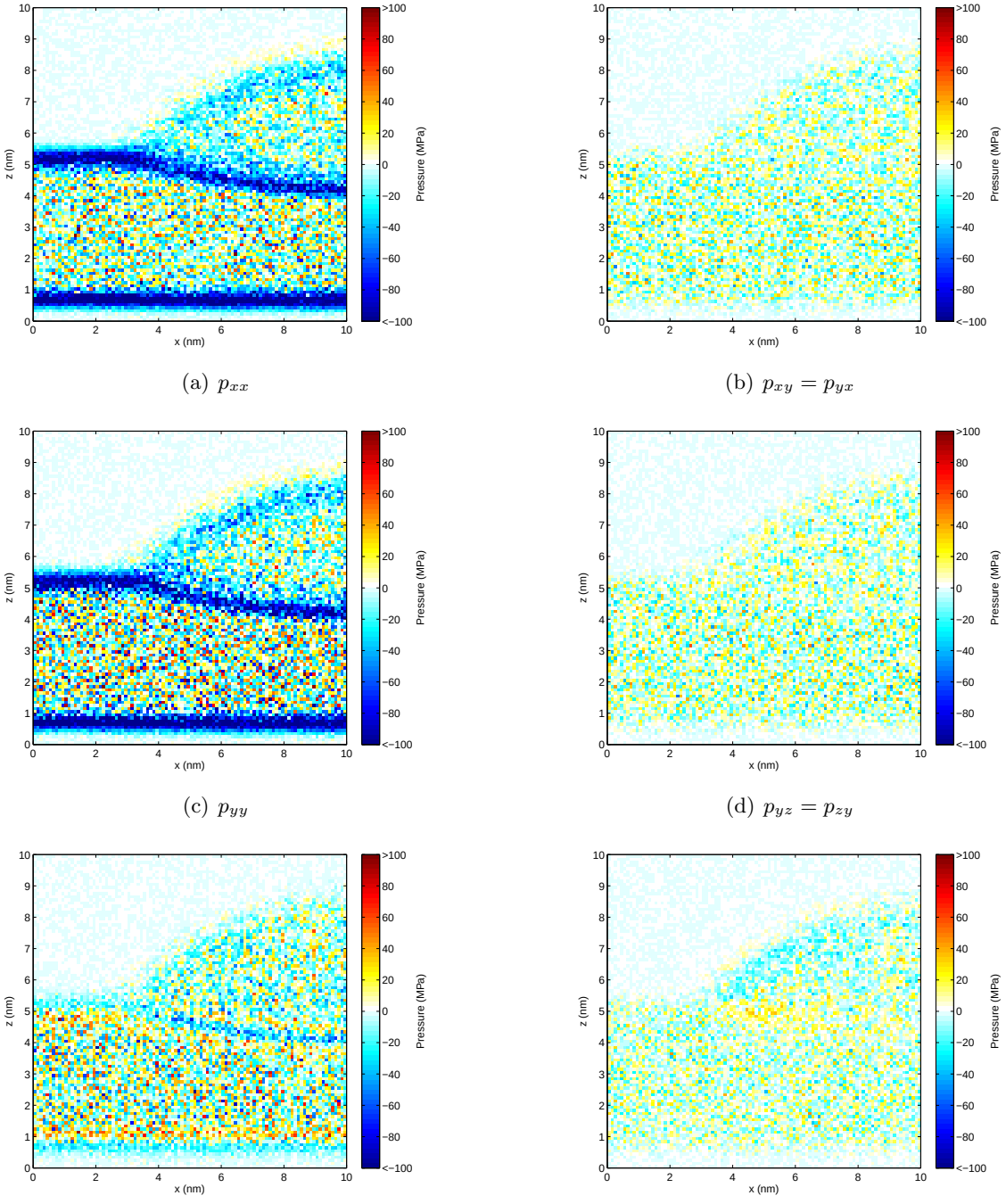

(a) p_{xx}

(b) $p_{xy} = p_{yx}$

(c) p_{yy}

(d) $p_{yz} = p_{zy}$

(e) p_{zz}

(f) $p_{zx} = p_{xz}$

Figure 5.9: Local pressure distributions of multicomponent-oil–water–vapor three phase system.

this value is slightly lower than that from density distributions (66.69 ° = 49.82 ° + 16.87 °, Fig.5.8),this is almost maximum of the range of the error due to the errors in the interfacial tensions ($\theta_1^0 + \theta_2^0 = 65.70$ ° in case of $\cos(\theta_1^0 + \theta_2^0) = 0.61 - 0.20$).

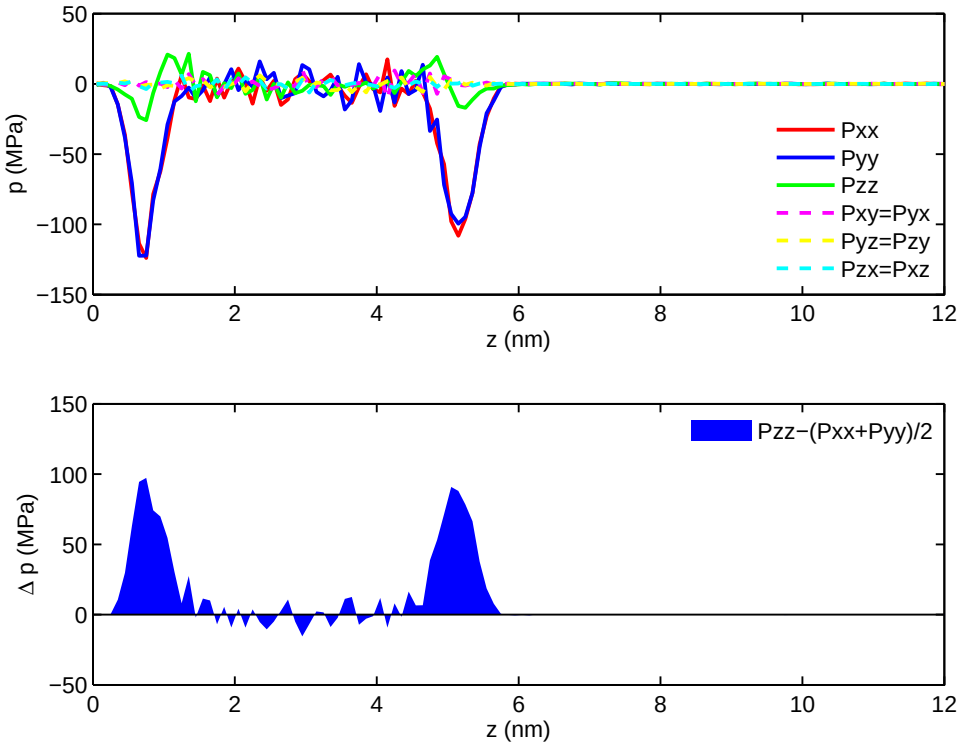

Figure 5.10: Local pressure profiles (top) and pressure difference profile (bottom) for multicomponent-oil–water–vapor three phase system along with z-axis averaged over $0 \leq x \leq 2$nm. Two regions in the pressure difference profile correspond to two water–vapor interfaces. The integrated value of each region gives the interfacial tension γ.

The line tension was calculated from the local pressure distributions, using same techniques with Chapter 4. Similar to Chapter 4, the distance-depended line tension $\tau(r)$ was used to evaluate the line tension τ (Eq.(4.62)). Fig.5.12 shows $\tau(r)$ with increasing the distance r from the three phase contact line (that is the intersection of GDSs). The $\tau(r)$ converges to 9.1×10^{-12}N at around $r > 1.5$nm. This value is also within the range of theoretical evaluations (10^{-12}–10^{-11}N Drelich (1996)). Surprisingly, the line tension of our multicomponent-oil–water–vapor three phase system is positive value, while that of our decane–water–vapor three phase system is negative. This causes an opposite behavior in a size dependence of contact angle

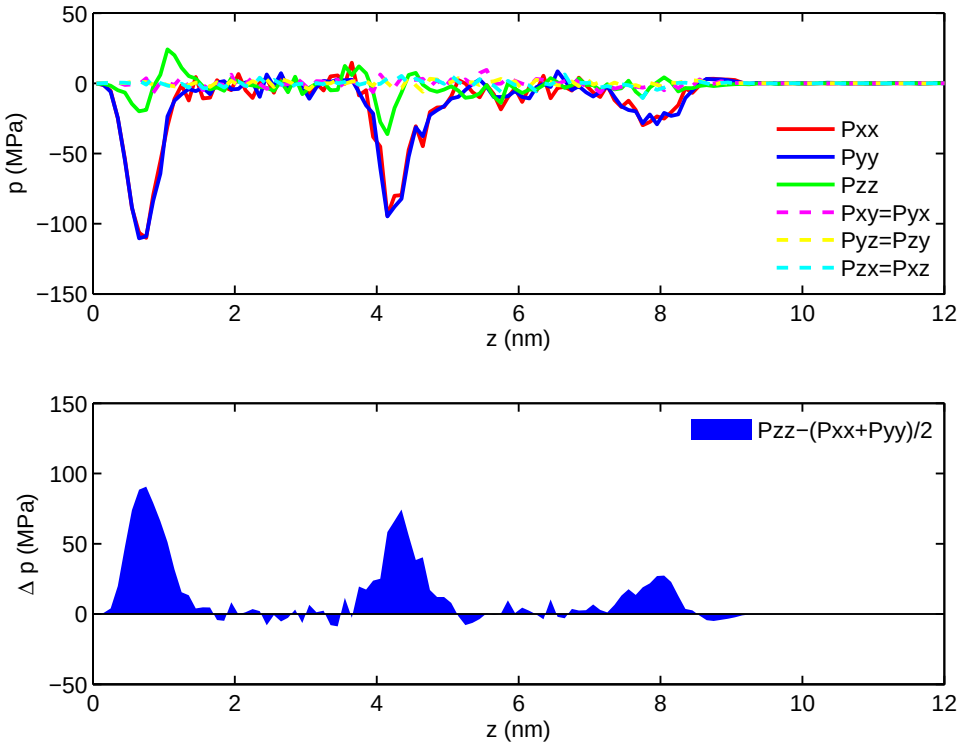

Figure 5.11: Local pressure profiles (top) and pressure difference profile (bottom) for multicomponent-oil–water–vapor three phase system along with z-axis averaged over $8 \leq x \leq 10$nm. Three regions in the pressure difference profile correspond to three interfaces, water–vapor, oil–water and oil–vapor, from left to right. The integrated value of each region gives the interfacial tension γ.

Table 5.2: Interfacial tension from local pressure distributions.

Phase 1	Phase 2	x (nm)	z (nm)	IFT† (mN/m)
Water	Vapor	0–10	0–2	58.06 ± 0.33
Water	Vapor	0–2	4–7	59.99 ± 0.94
Oil	Water	8–10	3–6	46.18 ± 2.94
Oil	Vapor	8–10	6–10	19.31 ± 2.83

† (Average)±(Standard error)

inside of the droplet. The size dependence of the contact angle was investigated by using same techniques with Chapter 4, Fig.5.13 shows the contact angle in the droplet phase as a function of droplet size. As mentioned above, Fig.5.13 shows opposite trend to Fig.4.28.

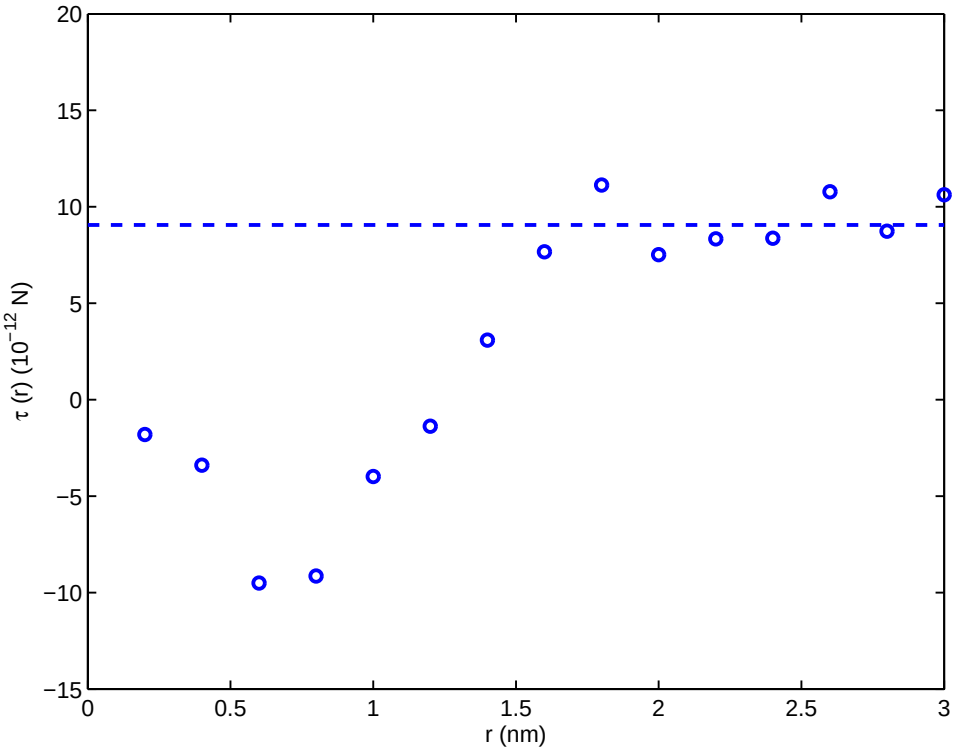

Figure 5.12: Distance-depended line tension $\tau\,(r)$ for multicomponent-oil–water–vapor three phase system against the distance r from the three phase contact line. The circle region $B(r)$ with the radius r was used for the integration. Dashed line shows the average value of $\tau\,(r)$ obtained from the last 5 values.

According to the theoretical approach done by Das and Binder (2011), the line tension value can be described as a function of the contact angle of the droplet (Fig.5.14). When the contact angle decreases, the line tension increases and changes from negative to positive values at one contact angle value. Although their research has been done for the droplet-on-solid system, it can be seen same trends even in our liquid–liquid–liquid three phase systems. In case of the decane–water–vapor three phase system, the contact angle of the droplet was 70.87 ° from their local pressure distributions (or 79.36 ° from their density distributions), and the line tension was -8.2×10^{-12}N. On the other hand, in case of the multicomponent-oil (ternary mixture of

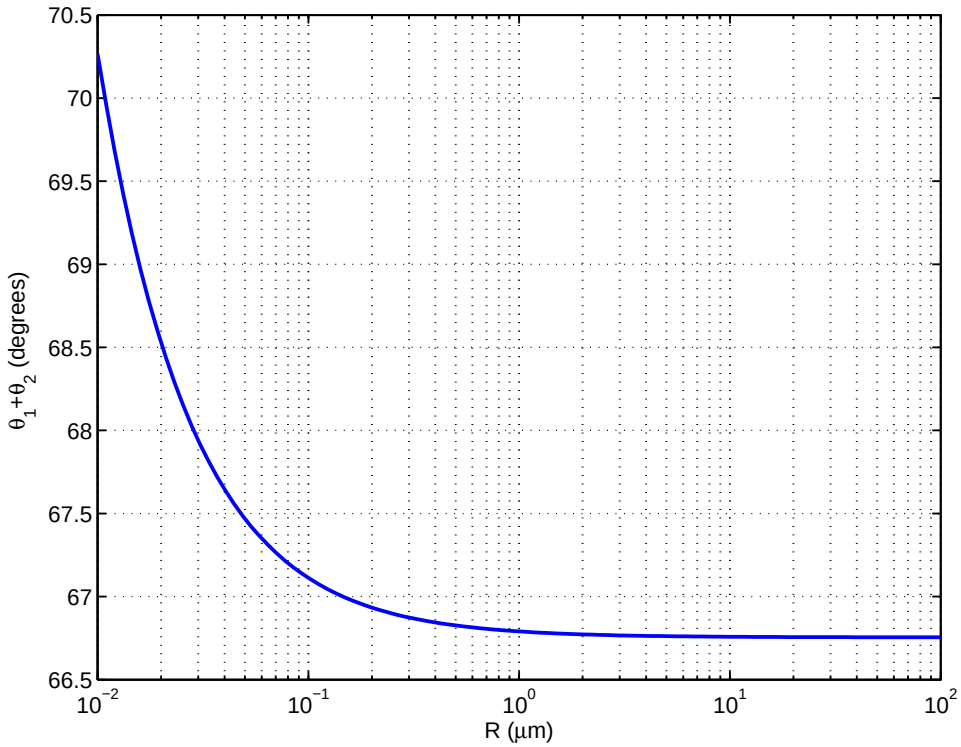

Figure 5.13: Contact angle inside of droplet $\theta_1 + \theta_2$, versus the radius of the contact line R.

heptane, decane and toluene)–water–vapor three phase system, that was 52.18 ° from their local pressure distributions (or 66.69 ° from their density distributions), and the line tension was 9.1×10^{-12}N. In other words, the line tension may be described as a function of the impurity of the droplet. In our case, the zero line tension is expected at the lower concentrations of heptane and toluene than those in our multicomponent-oil.

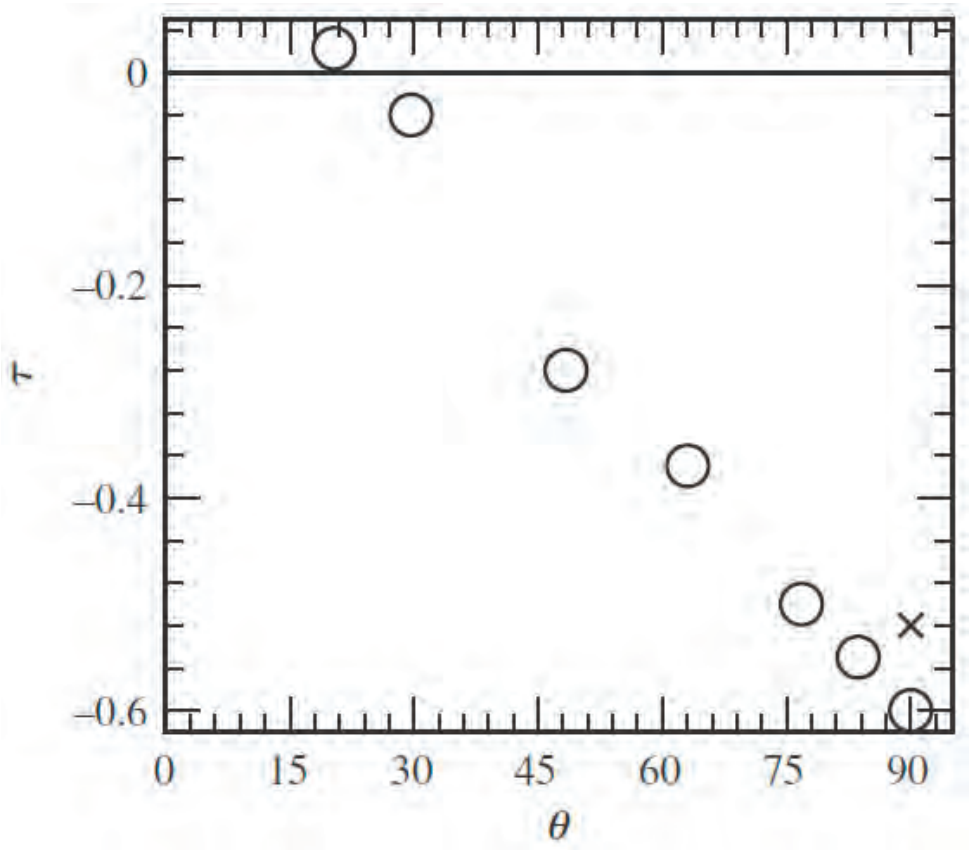

Figure 5.14: Line tension (circles), as extracted from the excess free energy of wall-attached droplets, plotted versus the contact angle θ (Das and Binder, 2011). The cross shows the result obtained from a finite size extrapolation of the free energy of flat interfaces confined by walls.

5.4 Conclusions

The interfacial equilibrium of multicomponent-oil–water–vapor three phase system has been investigated by using MD methods. The multicomponent-oil was modeled as the ternary mixture of heptane, decane and toluene molecules. The MD simulations showed weak accumulation of

lighter alkane at the oil–vapor interface and strong accumulation of aromatics at the oil–water interface, as expected from the results in Chapter 3. From the discussions at the three phase contact line, aromatic components in oil is predicted to spread preferentially over the water surface ahead of the bulk oil. The line tension value of the multicomponent-oil–water–vapor three phase system has been obtained successfully to 9.1×10^{-12}N by using same techniques with in Chapter 4. The line tension of the multicomponent-oil–water–vapor three phase system was positive, while that of the decane–water–vapor three phase system was negative (Chapter 4). This means the line tension of the decane–water–vapor system have increased and changed from negative to positive values by adding heptane and toluene molecules into decane droplet. The zero line tension is expected at some concentration of the multicomponent-oil. This is the effect caused by impurity of the liquid droplet on water surface. The three phase systems including highly complex materials can be also analyzed by using MD methods.

Chapter 6

Conclusion

The purpose of this dissertation was to investigate the interfacial equilibrium of various liquids, such as hydrocarbons, light-oil, water and their vapor in nano-scale by using Molecular Dynamics (MD) methods. This dissertation has shown following results:

In Chapter 3, the oil and water interface was investigated by using MD methods. The accuracies of hydrocarbon models were verified by comparing their calculated thermodynamic properties, such as the bulk density and interfacial tensions, to the experimental values at ambient conditions. Then, our light-oil model was modeled as the mixture of the eight kinds of hydrocarbons. After combining the light-oil model and water box, the interfacial equilibrium of the oil–water interface was investigated by using MD methods. The results showed the inhomogeneity of the molecular distributions, such as strong accumulation of aromatic molecules which were caused by the specific interaction between aromatic and water, called as weak hydrogen bonding.

In Chapter 4, the interfacial equilibrium of the decane–water–vapor three phase system was investigate by using MD methods. The MD simulation was carried out with an apparent 2 dimensional system, which has many advantages compared to 3 dimensional system. The inhomogeneity of the molecular distribution, especially at the vicinity of three phase contact line, and the interfacial tensions of each interface were obtained and discussed. In addition, in this chapter, the convenient way to calculate the line tension of a three phase system from the local pressure distributions was derived and applied to the decane–water-vapor three phase system. With this method, the line tension of the system was calculated successfully. This is intrinsic value for this three phase system, so that the effects caused by any other phenomena,

such as impurity of the droplet, to the line tension can be considered by taking it as a reference state.

In Chapter 5, the interfacial equilibrium of three phase system was investigated like in Chapter 4, but used the ternary mixture of heptane, decane and toluene molecules to model the multicomponent-oil droplet, instead of just decane. Same technical methodologies with Chapter 4 were used to obtain thermodynamic properties. The interfacial tensions and the molecular distributions of the multicomponent-oil–water–vapor three phase system were obtained and discussed for the investigations of the local structure. The line tension of the multicomponent-oil–water–vapor three phase system was also calculated successfully by using the equation derived in Chapter 4. Surprisingly, this value has opposite sign of that of pure decane–water–vapor three phase system (Chapter 4). We suggest that the effects were caused by impurity of droplet, such as lower interfacial tension and higher line tension, thin film of toluene molecules on water surface.

Remarks

The MD methods, which were shown in this dissertation in order to investigate the two phase and three phase interface systems, can extend to the system including the other fluid, such as nitrogen, carbon dioxide, methane, ethane and so on, related to oil industry. Moreover, the thermodynamic conditions can also be changed easily. Therefore, it is anticipated that these methods are applied for other various systems at high temperature and high pressure condition, like in an oil reservoir for EOR processes.

Appendix A

Force Field Parameters

Here all parameters used in this dissertation are listed. They are mainly based on the revised version of CHARMM27 force field (Davis et al., 2008; Klauda et al., 2005; MacKerell Jr et al., 1998). The SPC/E model is used for water molecules (Alejandre et al., 1995; Berendsen et al., 1987). Table.A.1 shows the definition of atom type, mass, charge, and Lennard-Jones parameters.

The equation of each potential is written again in followings. Table.A.2 shows the parameters in bonding interactions, which is given by:

$$U_b\left(r_{ij}\right) = \frac{1}{2}k_{ij}^{b}\left(r_{ij} - b_{ij}\right)^2 \tag{A.1}$$

Table.A.3 shows the parameters in angle interactions, which are given by:

$$U_a\left(\theta_{ijk}\right) = \frac{1}{2}k_{ijk}^{\theta}\left(\theta_{ijk} - \theta_{ijk}^{0}\right)^2 \tag{A.2}$$

or

$$U_a\left(\theta_{ijk}\right) = \frac{1}{2}k_{ijk}^{\theta}\left(\theta_{ijk} - \theta_{ijk}^{0}\right)^2 + \frac{1}{2}k_{ijk}^{UB}\left(r_{ik} - r_{ik}^{0}\right)^2 \tag{A.3}$$

Table.A.4 shows the parameters in dihedral interactions, which is given by:

$$U_d\left(\phi_{ijkl}\right) = k_{\phi}\left(1 + \cos\left(n\phi - \phi_s\right)\right) \tag{A.4}$$

Table A.1: Definition of atom name and non-bonding parameters.

Atom type	Mass (a.m.u.)	Charge (e)	σ_{ii} (nm)	ϵ_{ii} (kJ/mol)	Element specification
For n-Alkanes and Cycloalkanes					
CTL3	12.0110	-0.2700	0.3635	0.3264	Carbon atom in -CH_3
CTL2	12.0110	-0.1800	0.3581	0.2343	Carbon atom in -CH_2-
HAL3	1.0080	0.0900	0.2388	0.1004	Hydrogen atom in -CH_3
HAL2	1.0080	0.0900	0.2388	0.1172	Hydrogen atom in -CH_2-
For Benzene and Toluene					
CA	12.0110	-0.1150	0.3550	0.2929	Carbon atom in -CH-
HP	1.0080	0.1150	0.2420	0.1255	Hydrogen atom in -CH-
CT3	12.0110	-0.0650	0.3671	0.3347	Carbon atom in -CH_3
HA	1.0080	0.0600	0.2352	0.0921	Hydrogen atom in -CH_3
For Water					
OW	15.9994	-0.8476	0.3166	0.6502	Oxygen atom in SPC/E water
HW	1.0080	0.4238	0.0000	0.0000	Hydrogen atom in SPC/E water

Table A.2: Parameters for bonding interaction.

Atom i	Atom j	b_{ij} (nm)	k^b_{ij} (kJ/mol)
CTL2	HAL2	0.1111	258571.2
CTL3	HAL3	0.1111	269449.6
CTL2	CTL2	0.1530	186188.0
CTL2	CTL3	0.1528	186188.0
CA	CA	0.1375	255224.0
CT3	CA	0.1490	192464.0
HA	CT3	0.1111	269449.6
HP	CA	0.1080	284512.0

Table A.3: Parameters for angle interaction.

Atom i	Atom j	Atom k	θ^0_{ijk} (deg)	k^θ_{ijk} (kJ/mol)	r^0_{ik} (nm)	k^{UB}_{ijk} (kJ/mol)
HAL2	CTL2	HAL2	109.00	297.0640	0.1802	4518.720
HAL3	CTL3	HAL3	108.40	297.0640	0.1802	4518.720
HAL2	CTL2	CTL2	110.10	221.7520	0.2179	18853.104
HAL2	CTL2	CTL3	110.10	289.5328	0.2179	18853.104
HAL3	CTL3	CTL3	110.10	313.8000	0.2179	18853.104
CTL2	CTL2	CTL2	113.60	488.2728	0.2561	9338.688
CTL2	CTL2	CTL3	115.00	485.3440	0.2561	6694.400
CA	CA	CA	120.00	334.7200	0.2416	29288.000
CT3	CA	CA	122.30	383.2544	0.0000	0.000
HA	CT3	CA	107.50	412.5424	0.0000	0.000
HA	CT3	HA	108.40	297.0640	0.1802	4518.720
HP	CA	CA	120.00	251.0400	0.2153	18409.600

Table A.4: Parameters for dihedral interaction.

Atom i	Atom j	Atom k	Atom l	ϕ_s (deg)	k_ϕ (kJ/mol)	n
CTL3	CTL2	CTL2	CTL3	0.00	0.15989	2
CTL3	CTL2	CTL2	CTL3	180.00	0.13310	6
CTL2	CTL2	CTL2	CTL3	0.00	0.63016	2
CTL2	CTL2	CTL2	CTL3	180.00	0.34051	3
CTL2	CTL2	CTL2	CTL3	0.00	0.45318	4
CTL2	CTL2	CTL2	CTL3	0.00	0.85373	5
CTL2	CTL2	CTL2	CTL2	0.00	0.27005	2
CTL2	CTL2	CTL2	CTL2	180.00	0.62697	3
CTL2	CTL2	CTL2	CTL2	0.00	0.39599	4
CTL2	CTL2	CTL2	CTL2	0.00	0.47106	5
X†	CTL2	CTL2	X†	0.00	0.79496	3
X†	CTL2	CTL3	X†	0.00	0.66944	3
CA	CA	CA	CA	180.00	12.97040	2
CT3	CA	CA	CA	180.00	12.97040	2
HP	CA	CA	CA	180.00	17.57280	2
HP	CA	CA	CT3	180.00	17.57280	2
HP	CA	CA	HP	180.00	10.04160	2
X†	CT3	CA	X†	0.00	0.00000	6

† atom type which is not specified in other dihedral combinations.

References

J. Alejandre, D. Tildesley, and G. Chapela. Molecular-dynamics simulation of the orthobaric densities and surface-tension of water. *Journal of Chemical Physics*, 102(11):4574–4583, MAR 15 1995. ISSN 0021-9606. 20, 53, 75, 85, 106

M. Allen and D. Tildesley. *Computer simulation of liquids*, volume 18. Oxford university press, 1989. 5, 16

M. Allesch, F. C. Lightstone, E. Schwegler, and G. Galli. First principles and classical molecular dynamics simulations of solvated benzene. *Journal of Chemical Physics*, 128(1), JAN 7 2008. ISSN 0021-9606. 33

A. Amirfazli and A. Neumann. Status of the three-phase line tension. *Advances in Colloid and Interface Science*, 110(3):121–141, AUG 31 2004. ISSN 0001-8686. 45, 73, 78

E. Amott. Observations relating to the wettability of porous rock. *Transactions of the American Institute of Mining and Metallurgical Engineers*, 216:156–162, 1959. 41

M. Assael, J. Trusler, and T. Tsolakis. *Thermophysical properties of fluids*. Imperial College Press, 1996. 1

C. Baker and G. Grant. Modeling aromatic liquids: Toluene, phenol, and pyridine. *J. Chem. Theory Comput*, 3(2):530–548, 2007. 37

M. Batzle and Z. Wang. Seismic properties of pore fluids. *Geophysics*, 57:1396, 1992. 1

I. Benjamin. Molecular structure and dynamics at liquid-liquid interfaces. *Annual Review of Physical Chemistry*, 48:407–451, 1997. ISSN 0066-426X. 1, 65

H. Berendsen, J. Grigera, and T. Straatsma. The missing term in effective pair potentials. *Journal of Physical Chemistry*, 91(24): 6269–6271, NOV 19 1987. ISSN 0022-3654. 20, 53, 85, 106

H. Berendsen, J. Postma, W. Vangunsteren, A. Dinola, and J. Haak. Molecular-dynamics with coupling to an external bath. *Journal of Chemical Physics*, 81(8):3684–3690, 1984. ISSN 0021-9606. 12, 13

E. Bertrand, T. D. Blake, and J. De Coninck. Influence of solid-liquid interactions on dynamic wetting: a molecular dynamics study. *Journal of Physics-Condensed Matter*, 21(46), NOV 18 2009. ISSN 0953-8984. 41

E. Bertrand, D. Bonn, J. Meunier, and D. Segal. Wetting of alkanes on water. *Physical Review Letters*, 86(14):3208–3208, 2001. 42

E. Bertrand, H. Dobbs, D. Broseta, J. Indekeu, D. Bonn, and J. Meunier. First-order and critical wetting of alkanes on water. *Physical Review Letters*, 85(6):1282–1285, 2000. 42

F. Biscay, A. Ghoufi, V. Lachet, and P. Malfreyt. Calculation of the surface tension of cyclic and aromatic hydrocarbons from Monte Carlo simulations using an anisotropic united atom model (AUA). *Physical Chemistry Chemical Physics*, 11(29):6132–6147, 2009. ISSN 1463-9076. 19

T. D. Blake. The physics of moving wetting lines. *Journal of Colloid and Interface Science*, 299(1):1–13, JUL 1 2006. ISSN 0021-9797. 41

D. Bonn, J. Eggers, J. Indekeu, J. Meunier, and E. Rolley. Wetting and spreading. *Reviews of Modern Physics*, 81(2):739–805, APR-JUN 2009. ISSN 0034-6861. 1, 41, 42

D. Bonn and D. Ross. Wetting transitions. *Reports on Progress in Physics*, 64(9):1085–1163, SEP 2001. ISSN 0034-4885. 41, 42

P. Bonnaud, C. Nieto-Draghi, and P. Ungerer. Anisotropic united atom model including the electrostatic interactions of benzene. *Journal of Physical Chemistry B*, 111(14):3730–3741, APR 12 2007. ISSN 1520-6106. 37

F. Bresme, E. Chacon, P. Tarazona, and K. Tay. Intrinsic structure of hydrophobic surfaces: The oil-water interface. *Physical Review Letters*, 101(5), AUG 1 2008. ISSN 0031-9007. 3, 19

D. Chandler. Physical chemistry - Oil on troubled waters. *Nature*, 445(7130):831–832, FEB 22 2007. ISSN 0028-0836. 1

G. Chapela, G. Saville, S. Thompson, and J. Rowlinson. Computer-simulation of a gas-liquid surface .1. *Journal of the Chemical Society-faraday Transactions II*, 73:1133–1144, 1977. ISSN 0300-9238. 24

P. Chau and A. Hardwick. A new order parameter for tetrahedral configurations. *Molecular Physics*, 93(3):511–518, FEB 20 1998. ISSN 0026-8976. 3

A. Checco, P. Guenoun, and J. Daillant. Nonlinear dependence of the contact angle of nanodroplets on contact line curvature. *Physical Review Letters*, 91(18), OCT 31 2003. ISSN 0031-9007. 78

A. Checco, H. Schollmeyer, J. Daillant, P. Guenoun, and R. Boukherroub. Nanoscale wettability of self-assembled monolayers investigated by noncontact atomic force microscopy. *langmuir*, 22(1):116–126, JAN 3 2006. ISSN 0743-7463. 78

R. Chelli, G. Cardini, P. Procacci, R. Righini, S. Califano, and A. Albrecht. Simulated structure, dynamics, and vibrational spectra of liquid benzene. *The Journal of Chemical Physics*, 113:6851, 2000. 37

P. Cheng, D. Li, L. Boruvka, Y. Rotenberg, and A. Neumann. Automation of axisymmetric drop shape-analysis for measurement of interfacial-tensions and contact angles. *Colloids and Surfaces*, 43(2-4):151–167, FEB 1990. ISSN 0166-6622. 41

P. Chiquet, J. Daridon, D. Broseta, and S. Thibeau. CO2/water interfacial tensions under pressure and temperature conditions of CO2 geological storage. *Energy Conversion and Management*, 48 (3):736–744, 2007. 1

E. R. Cruz-Chu, A. Aksimentiev, and K. Schulten. Water-silica force field for simulating nanodevices. *Journal of Physical Chemistry B*, 110(43):21497–21508, NOV 2 2006. ISSN 1520-6106. 41

R. Cygan, J. Liang, and A. Kalinichev. Molecular models of hydroxide, oxyhydroxide, and clay phases and the development of a general force field. *Journal of Physical Chemistry B*, 108(4): 1255–1266, JAN 29 2004. ISSN 1520-6106. 7

S. K. Das and K. Binder. Simulation of binary fluids exposed to selectively adsorbing walls: a method to estimate contact angles and line tensions. *MOLECULAR PHYSICS*, 109(7-10, SI):1043–1056, 2011. ISSN 0026-8976. 100, 102

J. E. Davis, G. L. Warren, and S. Patel. Revised charge equilibration potential for liquid alkanes. *Journal of Physical Chemistry B*, 112 (28):8298–8310, JUL 17 2008. ISSN 1520-6106. 7, 20, 53, 85, 106

J. De Coninck and T. D. Blake. Wetting and molecular dynamics simulations of simple liquids. *Annual Review of Materials Research*, 38:1–22, 2008. ISSN 1531-7331. 41

M. De Ruijter, T. Blake, and J. De Coninck. Dynamic wetting studied by molecular modeling simulations of droplet spreading. *Langmuir*, 15(22):7836–7847, OCT 26 1999. ISSN 0743-7463. 41

M. De Serio, H. Mohapatra, R. Zenobi, and V. Deckert. Investigation of the liquid-liquid interface with high spatial resolution using near-field Raman spectroscopy. *Chemical Physics Letters*, 417(4-6):452–456, JAN 10 2006. ISSN 0009-2614. 3, 19, 40

P. Degennes. Wetting - statics and dynamics. *Reviews of Modern Physics*, 57(3):827–863, 1985. ISSN 0034-6861. 41

J. Di Leo and J. Maranon. Confined water/oil interface. Molecular dynamics study. *Journal of Molecular Structure-Theochem*, 672 (1-3):221–229, MAR 1 2004. ISSN 0166-1280. 1

M. E. Diaz, J. Fuentes, R. L. Cerro, and M. D. Savage. An analytical solution for a partially wetting puddle and the location of the static contact angle. *Journal of Colloid and Interface Science*, 348(1):232–239, AUG 1 2010. ISSN 0021-9797. 41

J. Dickson, G. Gupta, T. Horozov, B. Binks, and K. Johnston. Wetting phenomena at the CO2/water/glass interface. *Langmuir*, 22 (5):2161–2170, FEB 28 2006. ISSN 0743-7463. 41

A. Dixit, J. Buckley, S. McDougall, and K. Sorbie. Empirical measures of wettability in porous media and the relationship between them derived from pore-scale modelling. *Transport in Porous Media*, 40(1):27–54, JUL 2000. ISSN 0169-3913. 41

D. Donahue and F. Bartell. The boundary tension at water organic liquid interfaces. *Journal of Physical Chemistry*, 56(4):480–489, 1952. ISSN 0022-3654. 24, 26

E. Donaldson and W. Alam. *Wettability: Wettability. 2, Surface forces. 3, Wettability and production. 4, Pore size effects and wettability alteration. 5, Practical applications of wettability. 6, Fortran computer programs. 7, Front tracking program.* Gulf Publishing Company, 2008. 41

J. Drelich. The significance and magnitude of the line tension in three-phase (solid-liquid-fluid) systems. *Colloids and Surfaces A-physicochemical and Engineering Aspects*, 116(1-2):43–54, SEP 16 1996. ISSN 0927-7757. Wetting and Interfacial Phenomena Symposium, at the 69th Annual Colloid and Surface Science Symposium, SALT LAKE CITY, UT, JUN, 1995. 45, 80, 98

Q. Du, E. Freysz, and Y. Shen. Surface vibrational spectroscopic studies of hydrogen-bonding and hydrophobicity. *Science*, 264 (5160):826–828, MAY 6 1994. ISSN 0036-8075. 3, 19, 40

E. Dussan. Spreading of liquids on solid-surfaces - static and dynamic contact lines. *Annual Review of Fluid Mechanics*, 11:371–400, 1979. ISSN 0066-4189. 41

A. Dussaud and M. VignesAdler. Wetting transition of n-alkanes on concentrated aqueous salt solutions. Line tension effect. *Langmuir*, 13(3):581–589, FEB 5 1997. ISSN 0743-7463. 42

U. Essmann, L. Perera, M. Berkowitz, T. Darden, H. Lee, and L. Pedersen. A smooth particle mesh Ewald method. *Journal of Chemical Physics*, 103(19):8577–8593, 1995. 11, 22, 56, 86

S. Feller, Y. Zhang, and R. Pastor. Computer-simulation of liquid/liquid interfaces .2. surface-tension area dependence of a bilayer and monolayer. *Journal of Chemical Physics*, 103(23):10267–10276, DEC 15 1995. ISSN 0021-9606. 15, 16

M. Fioroni and D. Vogt. Toluene Model for Molecular Dynamics Simulations in the Ranges 298 T (K) 350 and 0.1 P (MPa) 10. *Journal of Physical Chemistry B-Condensed Phase*, 108(31):11774–11781, 2004. 37

D. Frenkel and B. Smit. *Understanding molecular simulation: from algorithms to applications*, volume 1. Academic Pr, 2002. 5

A. Goebel and K. Lunkenheimer. Interfacial tension of the water/n-alkane interface. *Langmuir*, 13(2):369–372, JAN 22 1997. ISSN 0743-7463. 24, 26, 32, 75

G. Graziano and B. Lee. Hydration of aromatic hydrocarbons. *Journal of Physical Chemistry B*, 105(42):10367–10372, OCT 25 2001. ISSN 1089-5647. 33, 39

E. Guggenheim. Statistical thermodynamics of the surface of a regular solution. *Transactions of the Faraday Society*, 41(3):150–156, 1945. 32

W. Harkins and A. Feldman. Films the spreading of liquids and the spreading coefficient. *Journal of the American Chemical Society*, 44:2665–2685, JUL-DEC 1922. ISSN 0002-7863. 41, 42

J. Harris. Liquid vapor interfaces of alkane oligomers - structure and thermodynamics from molecular-dynamics simulations of chemically realistic models. *Journal of Physical Chemistry*, 96(12): 5077–5086, JUN 11 1992. ISSN 0022-3654. 24

B. Hess, C. Kutzner, D. van der Spoel, and E. Lindahl. Gromacs 4: Algorithms for highly efficient, load-balanced, and scalable molecular simulation. *J. Chem. Theory Comput*, 4(3):435–447, 2008. 5, 20, 56, 86

G. Hirasaki. Structural interactions in the prediction of wetting of vanderwaals fluids. *Abstracts of Papers of the American Chemical Society*, 203(Part 1):41–COLL, APR 5 1992. ISSN 0065-7727. 41

S. D. Hong, M. Y. Ha, and S. Balachandar. Static and dynamic contact angles of water droplet on a solid surface using molecular dynamics simulation. *Journal of Colloid and Interface Science*, 339(1):187–195, NOV 1 2009. ISSN 0021-9797. 41

W. Hoover. Canonical dynamics - equilibrium phase-space distributions. *Physical Review A*, 31(3):1695–1697, 1985. ISSN 1050-2947. 15

D. K. Hore, D. S. Walker, and G. L. Richmond. Water at hydrophobic surfaces: When weaker is better. *Journal of the American Chemical Society*, 130(6):1800+, FEB 13 2008. ISSN 0002-7863. 1

C. Huh and L. Scriven. Hydrodynamic model of steady movement of a solid/liquid/fluid contact line. *Journal of Colloid and Interface Science*, 35(1):85–&, 1971. ISSN 0021-9797. 41

W. Humphrey, A. Dalke, and K. Schulten. VMD: visual molecular dynamics. *Journal of Molecular Graphics*, 14(1):33–38, 1996. 56, 86

N. Ikeda, M. Aratono, and K. Motomura. Thermodynamic study on the adsorption of sodium-chloride at the water hexane interface. *Journal of Colloid and Interface Science*, 149(1):208–215, MAR 1 1992. ISSN 0021-9797. 3

J. Indekeu. Line tension at wetting. *International Journal of Modern Physics B*, 8(3):309–345, JAN 30 1994. ISSN 0217-9792. 45

J. Israelachvili. *Intermolecular and Surface Forces: Revised Third Edition*. Academic press, 2011. 16

P. Jadhunandan and N. Morrow. Effect of wettability on waterflood recovery for crude-oil brine rock systems. *SPE Reservoir Engineering*, 10(1):40–46, FEB 1995. ISSN 0885-9248. 41

S. Jang, S. Lin, P. Maiti, M. Blanco, W. Goddard, P. Shuler, and Y. Tang. Molecular dynamics study of a surfactant-mediated decane-water interface: Effect of molecular architecture of alkyl benzene sulfonate. *Journal of Physical Chemistry B*, 108(32): 12130–12140, AUG 12 2004. ISSN 1520-6106. 3, 19, 40

P. Jungwirth, B. Finlayson-Pitts, and D. Tobias. Introduction: Structure and chemistry at aqueous interfaces. *Chemical Reviews*, 106(4):1137–1139, APR 2006. ISSN 0009-2665. 2

K. Kadau, T. Germann, and P. Lomdahl. Large-scale molecular-dynamics simulation of 19 billion particles. *International Journal of Modern Physics C*, 15(1):193–201, JAN 2004. ISSN 0129-1831. 5

F. Kalaydjian, J. Moulu, O. Vizika, and P. Munkerud. Three-phase flow in water-wet porous media: determination of gas/oil relative permeabilities under various spreading conditions. In *SPE Annual Technical Conference and Exhibition*, 1993. 41

A. Kantzas, I. Chatzis, and F. Dullien. Enhanced oil recovery by inert gas injection. In *SPE Enhanced Oil Recovery Symposium*, 1988. 41

Y. Kataoka. Studies of liquid water by computer-simulations .5. equation of state of fluid water with carravetta-clementi potential. *Journal of Chemical Physics*, 87(1):589–598, JUL 1 1987. ISSN 0021-9606. 15

I. Kereszturi and P. Jedlovszky. Computer simulation investigation of the water-benzene interface in a broad range of thermodynamic states from ambient to supercritical conditions. *Journal of Physical Chemistry B*, 109(35):16782–16793, SEP 8 2005. ISSN 1520-6106. 3, 19, 20

J. Kerins and M. Boiteux. Applications of noether's theorem to inhomogeneous fluids. *Physica A: Statistical and Theoretical Physics*, 117(2-3):575–592, 1983. 45, 46, 47, 78

J. Kirkwood and F. Buff. The statistical mechanical theory of surface tension. *Journal of Chemical Physics*, 17(3):338–343, 1949. ISSN 0021-9606. 24, 71

J. Klauda, B. Brooks, A. MacKerell Jr, R. Venable, and R. Pastor. An ab initio study on the torsional surface of alkanes and its effect on molecular simulations of alkanes and a DPPC bilayer. *J. Phys. Chem. B*, 109(11):5300–5311, 2005. 7, 20, 53, 85, 106

L. Lake. Enhanced oil recovery. 1989. 1, 2, 19, 41

J. Lambert, R. Hergenroeder, D. Suter, and V. Deckert. Probing Liquid-Liquid Interfaces with Spatially Resolved NMR Spectroscopy. *Angewandte Chemie-International Edition*, 48(34):6343–6345, 2009. ISSN 1433-7851. 3, 19, 40

D. Lee, M. Dagama, and K. Gubbins. Adsorption and surface-tension reduction at the vapor liquid interface. *Journal of Physical Chemistry*, 89(8):1514–1519, 1985. ISSN 0022-3654. 78

E. Lemmon, M. McLinden, and D. Friend. Thermophysical properties of fluid systems in nist chemistry webbook, nist standard reference database number 69, eds. *PJ Linstrom and WG Mallard, June*, 2005. 22, 24

P. Linse. Monte-carlo simulation of liquid liquid benzene water interface. *Journal of Chemical Physics*, 86(7):4177–4187, APR 1 1987. ISSN 0021-9606. 3, 19, 20

J. Lopez-Lemus, G. A. Chapela, and J. Alejandre. Effect of flexibility on surface tension and coexisting densities of water. *Journal of Chemical Physics*, 128(17), MAY 7 2008. ISSN 0021-9606. 24

A. MacKerell Jr, D. Bashford, M. Bellott, R. Dunbrack Jr, J. Evanseck, M. Field, S. Fischer, J. Gao, H. Guo, S. Ha, et al. All-atom empirical potential for molecular modeling and dynamics studies of proteins. *Journal of Physical Chemistry B-Condensed Phase*, 102(18):3586–3616, 1998. 7, 20, 53, 85, 106

H. Maeda and K. Okatsu. Eor using thin oil film drainage mechanism in water wet oil reservoir. *SPE*, page 116532, 2008. 41, 43

D. Mitrinovic, A. Tikhonov, M. Li, Z. Huang, and M. Schlossman. Noncapillary-wave structure at the water-alkane interface. *Physical Review Letters*, 85(3):582–585, JUL 17 2000. ISSN 0031-9007. 3, 19, 20

K. Moran, A. Yeung, and J. Masliyah. Measuring interfacial tensions of micrometer-sized droplets: A novel micromechanical technique. *Langmuir*, 15(24):8497–8504, NOV 23 1999. ISSN 0743-7463. 24, 26

N. Morrow. Wettability and its effect on oil-recovery. *Journal of Petroleum Technology*, 42(12):1476–1484, DEC 1990. ISSN 0149-2136. 41

J. Nicolas and N. de Souza. Molecular dynamics study of the n-hexane-water interface: Towards a better understanding of the liquid-liquid interfacial broadening. *Journal of Chemical Physics*, 120(5):2464–2469, FEB 1 2004. ISSN 0021-9606. 3, 19

T. Nomoto and H. Onishi. Fourth-order coherent Raman spectroscopy in a time domain: applications to buried interfaces. *Physical Chemistry Chemical Physics*, 9(41):5515–5521, 2007. ISSN 1463-9076. 3, 19, 40

S. Nose. A molecular-dynamics method for simulations in the canonical ensemble. *Molecular Physics*, 52(2):255–268, 1984. ISSN 0026-8976. 12, 15, 22, 56, 86

S. Nose and M. Klein. Constant pressure molecular-dynamics for molecular-systems. *Molecular Physics*, 50(5):1055–1076, 1983. ISSN 0026-8976. 15

O. Ollila, H. Risselada, M. Louhivuori, E. Lindahl, I. Vattulainen, and S. Marrink. 3d pressure field in lipid membranes and membrane-protein complexes. *Physical Review Letters*, 102(7): 78101, 2009. 56, 86

M. Parrinello and A. Rahman. Strain fluctuations and elastic constants. *The Journal of Chemical Physics*, 76:2662, 1982. 13, 15, 22, 56, 86

S. A. Patel and C. L. Brooks, III. Revisiting the hexane-water interface via molecular dynamics simulations using nonadditive alkane-water potentials. *Journal of Chemical Physics*, 124(20), MAY 28 2006. ISSN 0021-9606. 3, 19

K. Pedersen and P. Christensen. *Phase behavior of petroleum reservoir fluids*. CRC, 2006. 1, 3, 19, 20

T. Pfohl and H. Riegler. Critical wetting of a liquid/vapor interface by octane. *Physical Review Letters*, 82(4):783–786, 1999. 42

B. Poling, J. Prausnitz, and O. John Paul. *The properties of gases and liquids*, volume 5. McGraw-Hill New York, 2001. 15

J. Prausnitz, R. Lichtenthaler, and E. de Azevedo. *Molecular thermodynamics of fluid-phase equilibria*. Prentice Hall, 1998. 15

T. Qian, X. Wang, and P. Sheng. Power-law slip profile of the moving contact line in two-phase immiscible flows. *Physical Review Letters*, 93(9), AUG 27 2004. ISSN 0031-9007. 41

T. Qian, X.-P. Wang, and P. Sheng. A variational approach to moving contact line hydrodynamics. *Journal of Fluid Mechanics*, 564: 333–360, OCT 10 2006. ISSN 0022-1120. 41

W. Qu and D. Li. Line tension of simple liquid-liquid-fluid systems. *Colloids and Surfaces A-physicochemical and Engineering Aspects*, 156(1-3):123–135, OCT 15 1999. ISSN 0927-7757. 45

S. Rafaï, D. Bonn, E. Bertrand, J. Meunier, V. Weiss, and J. Indekeu. Long-range critical wetting: Observation of a critical end point. *Physical Review Letters*, 92(24):245701, 2004. 42

K. Ragil, J. Meunier, D. Broseta, J. Indekeu, and D. Bonn. Experimental observation of critical wetting. *Physical Review Letters*, 77(8):1532–1535, 1996. 42

P. Raiteri, R. Martonak, and M. Parrinello. Exploring polymorphism: The case of benzene. *Angewandte Chemie-International Edition*, 44(24):3769–3773, 2005. ISSN 1433-7851. 37

T. Raschke and M. Levitt. Nonpolar solutes enhance water structure within hydration shells while reducing interactions between them. *Proceedings of the National Academy of Sciences of the United States of America*, 102(19):6777–6782, MAY 10 2005. ISSN 0027-8424. 33

S. Rehfeld. Adsorption of sodium dodecyl sulfate at various hydrocarbon-water interfaces. *Journal of Physical Chemistry*, 71 (3):738–&, 1967. ISSN 0022-3654. 24, 26

M. Riazi and T. AlSahhaf. Physical properties of heavy petroleum fractions and crude oils. *Fluid Phase Equilibria*, 117(1-2):217–224, MAR 31 1996. ISSN 0378-3812. 7th International Conference on Fluid Properties and Phase Equilibria for Chemical Process Design, SNOWMASS VILLAGE, CO, JUN 18-23, 1995. 3

D. Ross, D. Bonn, A. Posazhennikova, J. Indekeu, and J. Meunier. Crossover from first-order to critical wetting: Short-range tricritical wetting. *Physical Review Letters*, 87(17):176103, 2001. 42

A. Rusanov. Surface thermodynamics revisited. *Surface Science Reports*, 58(5-8):111–239, SEP 2005. ISSN 0167-5729. 41, 45

L. Scatena, M. Brown, and G. Richmond. Water at hydrophobic surfaces: Weak hydrogen bonding and strong orientation effects. *Science*, 292(5518):908–912, MAY 4 2001. ISSN 0036-8075. 3, 19, 40

P. Schravendijk and N. van der Vegt. From hydrophobic to hydrophilic solvation: An application to hydration of benzene. *Journal of Chemical Theory and Computation*, 1(4):643–652, JUL-AUG 2005. ISSN 1549-9618. 33

S. Senapati and M. Berkowitz. Computer simulation study of the interface width of the liquid/liquid interface. *Physical Review Letters*, 87(17), OCT 22 2001. ISSN 0031-9007. 24, 65

D. Seveno, A. Vaillant, R. Rioboo, H. Adao, J. Conti, and J. De Coninck. Dynamics of Wetting Revisited. *Langmuir*, 25(22):13034–13044, NOV 17 2009. ISSN 0743-7463. 41

N. Shahidzadeh, D. Bonn, K. Ragil, D. Broseta, and J. Meunier. Sequence of two wetting transitions induced by tuning the hamaker constant. *Physical Review Letters*, 80(18):3992–3995, 1998. 42

D. Shaw and D. Shaw. *Introduction to colloid and surface chemistry*, volume 3. Butterworths London, 1980. 41, 42

Y. Solomentsev and L. White. Microscopic drop profiles and the origins of line tension. *Journal of Colloid and Interface Science*, 218(1):122–136, OCT 1 1999. ISSN 0021-9797. 45

S. Suzuki, P. Green, R. Bumgarner, S. Dasgupta, W. Goddard, and G. Blake. Benzene forms hydrogen-bonds with water. *Science*, 257(5072):942–944, AUG 14 1992. ISSN 0036-8075. 33

T. Takiue, A. Uemura, N. Ikeda, K. Motomura, and M. Aratono. Thermodynamic study on phase transition in adsorbed film of fluoroalkanol at the hexane/water interface. 3. Temperature effect on the adsorption of 1,1,2,2-tetrahydroheptadecafluorodecanol. *Journal of Physical Chemistry B*, 102(19):3724–3729, MAY 7 1998. ISSN 1089-5647. 32, 40

P. Tarazona and G. Navascues. A statistical mechanical theory for line tension. *Journal of Chemical Physics*, 75(6):3114–3120, 1981. ISSN 0021-9606. 45, 46, 47, 80

S. Thomas. Enhanced oil recovery - An overview. *Oil & Gas Science and Technology-revue De L Institut Francais Du Petrole*, 63 (1):9–19, JAN-FEB 2008. ISSN 1294-4475. 1, 2

B. Toshev, D. Platikanov, and A. Scheludko. Line tension in 3-phase equilibrium systems. *Langmuir*, 4(3):489–499, MAY-JUN 1988. ISSN 0743-7463. 45

A. van Buuren, S. Marrink, and H. Berendsen. A molecular-dynamics study of the decane water interface. *Journal of Physical Chemistry*, 97(36):9206–9212, SEP 9 1993. ISSN 0022-3654. 3, 19, 20, 37

D. Van Der Spoel, E. Lindahl, B. Hess, G. Groenhof, A. Mark, and H. Berendsen. Gromacs: fast, flexible, and free. *Journal of Computational Chemistry*, 26(16):1701–1718, 2005. 5, 56, 86

O. Vizika, E. Rosenberg, and F. Kalaydjian. Study of wettability and spreading impact in three-phase gas injection by cryo-scanning electron microscopy. *Journal of Petroleum Science and Engineering*, 20(3-4):189–202, JUN 1998. ISSN 0920-4105. 4th International Symposium on Evaluation of Reservoir Wettability and Its Effect on Oil Recovery, MONTPELLIER, FRANCE, SEP 11-13, 1996. 41

J. H. Weijs, A. Marchand, B. Andreotti, D. Lohse, and J. H. Snoeijer. Origin of line tension for a Lennard-Jones nanodroplet. *Physics of Fluids*, 23(2), FEB 2011. ISSN 1070-6631. 54, 55

B. Widom and H. Widom. Model for line tension in 3-phase equilibrium. *Physica A*, 173(1-2):72–110, APR 15 1991. ISSN 0378-4371. 45, 46, 80

T. Xia and U. Landman. Molecular-dynamics of adsorption and segregation from an alkane mixture. *Science*, 261(5126):1310–1312, SEP 3 1993. ISSN 0036-8075. 3, 20

A. Yeung, T. Dabros, and J. Masliyah. Does equilibrium interfacial tension depend on method of measurement? *Journal of Colloid and Interface Science*, 208(1):241–247, DEC 1 1998. ISSN 0021-9797. 24, 26, 32, 33

H. Zhang, M. Dong, and S. Zhao. Which one is more important in chemical flooding for enhanced court heavy oil recovery, lowering interfacial tension or reducing water mobility? *Energy & Fuels*, 24:1829–1836, MAR 2010. ISSN 0887-0624. 2

Y. Zhang, S. Feller, B. Brooks, and R. Pastor. Computer-simulation of liquid/liquid interfaces .1. theory and application to octane/water. *Journal of Chemical Physics*, 103(23):10252–10266, DEC 15 1995. ISSN 0021-9606. 15, 16, 17

Acknowledgment

I would like to appreciate my reviewers, Prof. Toshifumi Matsuoka, Prof. Takashi Kakiuchi and Prof. Hiroyasu Ohtsu at Kyoto University, who provided insightful comments and suggestions.

Also, I would like to appreciate my supervisors, Prof. Toshifumi Matsuoka and Assistant Prof. Yunfeng Liang at Kyoto University, whose encouragement, guidance and support from the initial to the final level enabled me to develop an understanding of the subject.

Also, I am heartily thankful to Prof. Norman R. Morrow, Prof. Koichi Takamura, Dr. Nina Loahardjo and Dr. Winoto Winoto at University of Wyoming, Prof. Yasuhiro Fukunaka at WASEDA University, Prof. Akira Ueda at Toyama University, and Associate Prof. Yasuhiro Yamada, Assistant Prof. Takeshi Tsuji at Kyoto University, for giving me constructive comments and warm encouragement. And I am indebted to my many of colleagues to support me.

Lastly, I offer my regards and blessings to my parents, my wife Marie and our daughter Mayuko. Without the generous help of these individuals, this thesis would not have been possible.

Makoto Kunieda

Ph.D. Thesis

Molecular Dynamics Study of Oil–Water Interfacial Equilibrium in Petroleum Engineering

---

Makoto Kunieda

Laboratory of Engineering Geology,
Department of Civil and Earth Resources Engineering,
Kyoto University

Kyoto University, Room C1-1-118
Kyotodaigaku-Katsura, Nishikyo-ku, Kyoto, 615-8540, Japan

m_kunieda@earth.kumst.kyoto-u.ac.jp
